MID-INFRARED ANTIMONIDE BASED

TYPE II QUANTUM DOT LASERS FOR USE

IN GAS SENSING

By

Qi Lu

A thesis submitted in fulfilment for the degree of Doctor of Philosophy at the University of

Lancaster

No part of this thesis has been submitted to any other university or other academic institution

February 2015

Mid-Infrared Antimonide Based Type II Quantum Dot Lasers for Use in Gas Sensing

By

Qi Lu

Abstract

Type II InSb/InAs quantum dots (QDs) emitting in the 3-4 µm range are promising candidate as the gain medium for semiconductor laser diodes. The molecular beam epitaxy (MBE) growth of the QDs on GaAs and InP substrates can largely cut down the costs for future devices and massively broaden its application possibilities using the more mature material platforms. Different metamorphic growth techniques including inter-facial misfit (IMF) arrays were experimented for the integration of the InSb QDs on GaAs substrates. The density of threading dislocations and the quality of the QDs were investigated using cross-sectional transmission electron microscopy (TEM) images, high resolution X-ray diffraction (XRD) and photo-luminescence (PL). The 4 K PL intensity and linewidth of InSb QDs grown onto a 3 µm thick InAs buffer layer directly deposited onto GaAs proved to be superior to that from QDs grown on 0.5 µm thick InAs buffer layers using either AlSb or GaSb interlayers with IMF technique. Even though the dislocation densities are still high in all the 3 samples ($\sim 10^9$ cm^{-2}), they all achieved comparable PL intensity as the QDs grown on InAs substrates. Electro-luminescence (EL) from the QDs on GaAs substrates were obtained up to 180 K,

which was the first step towards making mid-infrared InSb QD light sources on GaAs. From the study of PL temperature quenching, thermal excitation of holes out of the QDs was identified as one of the major reasons for weaker PL/EL signals at higher temperature range. To compensate the thermal leakage problem, the QDs integrated on InP substrates were grown between InGaAs barriers, which can provide a larger valence band offset compared with InAs. The QD PL peak moved to shorter wavelength (~2.7 μm) partly due to the stronger confinement, and the PL quenching was significantly slower for T > 100 K. From microscopy images, PL characteristics and calculations, the size and composition of the QDs were estimated.

The InSb QD laser structures on InAs substrates emitting at around 3.1 μm were improved by using liquid phase epitaxy (LPE) grown InAsSbP p-cladding layers and two step InAs n-cladding layers. The maximum working temperature was increased from 60 K to 120 K. The gain was determined to be 2.9 cm^{-1} per QD layer and the waveguide loss was around 15 cm^{-1} at 4 K. The emission wavelength of these lasers showed first a blue shift followed by a red shift with increasing temperature, identical with the PL characteristics. Multimodal spectra were measured using Fourier transform infrared spectroscopy (FTIR). Spontaneous emission measurements below threshold revealed a blue shift of the peak wavelength with increasing current, which was caused by the charging effect in the QDs. The characteristic temperature, $T_0 = 101K$ below 50 K, but decreased to 48K at higher temperatures. Current leakage from the active region into the cladding layers was possibly the main reason for the increase of threshold current and decay of T_0 with rising temperature.

Acknowledgements

First of all, I would like to thank my supervisor Professor Anthony Krier for all the support, guidance and discussions throughout my PhD study.

Secondly, special thanks need to be given to my vice supervisor Dr. Qiandong Zhuang for growing most of the samples for the project and the training I received on molecular beam epitaxy.

I need to thank Dr Andrew Marshall for his help and advice on clean room techniques, thank Dr. Manoj Keraria for the useful discussions on the material characterizations, thank Hiromi Fujita and Dr. Michael Thompson for the discussions on fabrication and measurement techniques, and thank Dr. Min Yin for the help and training on LPE growth and laser fabrication.

I would like to thank all the colleagues in my office for providing a pleasant working environment, including Ezekiel Anyebe, Kylie O'shea, Juanita James, Jonathan Hayton, Aiyeshah Alhodaib, Samual Harrison, Clair Tinker and Hayfaa Alradhi.

For all the excellent technical support in the physics department, I would like to thank Dr. Atif Aziz, Stephen Holden, Shonah Ion, Tim Clough, Stephen Holt, Peter Livesley, Robin Lewsey, Martin Ward and John Windsor.

I also need to give my acknowledgements to our external collaborators: Professor Abderrahim Ramdane, Dr Anthony Martinez and Konstantinos Papatryfonos in Laboratory in Photonics and Nanostructures, CNRS, France, for the trainings I received on laser fabrications and useful discussions with them, Dr Richard Beanland in Warwick University for TEM images, Dr. Krzysztof Klos in Procal for gas sensing training.

I'd like to thank all the members in the Marie Curie initial training network PROPHET. We had very useful discussions and had a great time during conferences and summer schools.

At last, special acknowledgements need to be given to the EU Marie Curie program PROPHET for providing the funding for my work and training.

Publications

1. Q. Lu, Q. Zhuang, J. Hayton, M. Yin and A. Krier, Gain and tuning characteristics of mid-infrared InSb quantum dot diode lasers, Appl. Phys. Lett. 105, 031115 (2014).

2. Q. Lu, Q. Zhuang, A. Marshall, M. Kesaria, R. Beanland and A. Krier, InSb quantum dots for the mid-infrared spectral range grown on GaAs substrates using metamorphic InAs buffer layers, Semicond. Sci. Technol. 29, 075011 (2014).

Conference presentations

1. Q. Lu, Q. Zhuang, J. Hayton and A. Krier, Gain and tuning characteristics of mid-infrared InSb quantum dot diode lasers, Mid-infrared optoelectronics materials and devices conference (MIOMD) 16, Montpellier, France, 5th -9th, October, 2014 (talk)

2. Q. Lu, Q. Zhuang, J. Hayton, M. Yin and A. Krier, Type II InSb/InAs quantum dot lasers emitting at 3.1 μm, Quantum dot day conference, Sheffield, UK, 10th, January, 2014 (poster)

3. Q. Lu, Q. Zhuang, A. Marshall and A. Krier, Luminescence study of type II InSb/InAs quantum dots on GaAs substrates. iNOW summer school, Cargese, France, 19th – 30th, August, 2013 (poster)

4. Q. Lu, Q. Zhuang, A. Krier, K. Papatryfonos, A. Martinez and A. Ramdane, Mid-infrared photo-luminescence and electro-luminescence from type II InSb/InAs quantum dots grown on GaAs substrates, 16th International conference on narrow gap semiconductors (NGS-16), Hangzhou, China, 2nd - 6th, August, 2013 (talk)

5. Q. Zhuang, M. Yin, Q. Lu, A. Marshall and A. Krier, Thermophotovoltaic cells based on pseudomorphic InAs on GaAs, 16th International conference on narrow gap semiconductors (NGS-16), Hangzhou, China, 2nd - 6th, August, 2013(talk)

6. Q. Lu, Q. Zhuang and A. Krier, Type II InSb/InAs quantum dots grown on GaAs substrates and design of laser structures, COST MP1024 summer school, Cortona, Italy, 20th – 23rd, May, 2013 (poster)

7. Q. Lu, P. Carrington, Q. Zhuang and A. Krier, Growth and Characterization of Type II InSb Quantum Dots for Mid-infrared Diode Lasers on GaAs Substrates, SIOE, Cardiff, 9th -11th, April, 2013 (talk)

8. Q. Lu, P. Carrington, Q. Zhuang and A. Krier, Antimonide based quantum dot lasers for use in gas sensing, UK semiconductors annual conference, Sheffield, UK, 3rd – 4th, July 2012 (poster)

Contents

1. Introduction

Semiconductor lasers, in which the optical gain is achieved by the stimulated emission from semiconductor materials, can emit light with high intensity, narrow linewidth and high coherence. The idea was first proposed in 1957 [1]. After the experimental demonstration of the ruby laser and He-Ne laser in 1960, pulsed oscillation of a GaAs semiconductor laser was observed at low temperature in 1962. In 1970, continuous wave oscillation at room temperature was accomplished. Since then, semiconductor lasers have seen tremendous developments and progresses in their structures and performances. Nowadays, they have become one of the most widely used optoelectronic devices, enabling a huge variety of applications such as optical communications, digital data storage and micro manufacturing. [1].

Quantum nanostructures such as quantum wells (QW) and quantum dots (QD) used as the gain medium in the laser have a number of crucial advantages compared with bulk semiconductor materials [2][3]. The modern material growth techniques of metal organic chemical vapour deposition (MOCVD) and molecular beam epitaxy (MBE) can enable the precise control of such nanostructures and their integration into lasers. Experimental demonstration of QW lasers using the GaAs/AlGaAs material system was first reported in 1977 [4]. In 1994, the first Fabry-Perot injection laser based on self-organized AGalAs/GaAs quantum dots (QDs) was reported [3]. The last two decades has seen significant developments of QW and QD lasers in the visible and near-infrared spectral range, different types of semiconductor lasers including distributed feedback (DFB) lasers, vertical cavity surface emitting lasers (VCSELs) and mode locked lasers have been invented for various applications.

In comparison, today's QW and QD laser technologies in the mid-infrared spectral region are still less well developed. The mid-infrared spectral region is in fact of enormous interest. With the help of suitable laser sources emitting in the 3-5 µm spectral range, different potential

applications can be realized, such as optical gas sensing, environmental pollution monitoring, chemical process control, non-invasive medical diagnosis, tunable IR spectroscopy, laser surgery and infrared countermeasures [5]. The mid-infrared region provides unique fingerprints with strong absorption bands for drug intermediates, pharmaceuticals, narcotics and bio-chemicals, allowing highly selective and sensitive detection or imaging. Consequently, the mid-infrared is very attractive for the development of sensitive optical sensor instrumentation. In addition, there is an atmospheric transmission window between 3 μm and 5 μm which enables free space optical communications and thermal imaging applications in both civil and military situations as well as the development of infrared countermeasures for homeland security. As shown in Fig. 1.1 the mid-infrared range contains the fundamental absorption bands of a number of important gases. There are many situations (e.g. oil-rigs, coal mines, landfill sites, car exhausts) where methane (3.3 μm), CO_2 (4.6 μm), CO (4.2 μm), NO_x (6.5 μm) and SO_x (7.3 μm) require accurate, in situ monitoring.
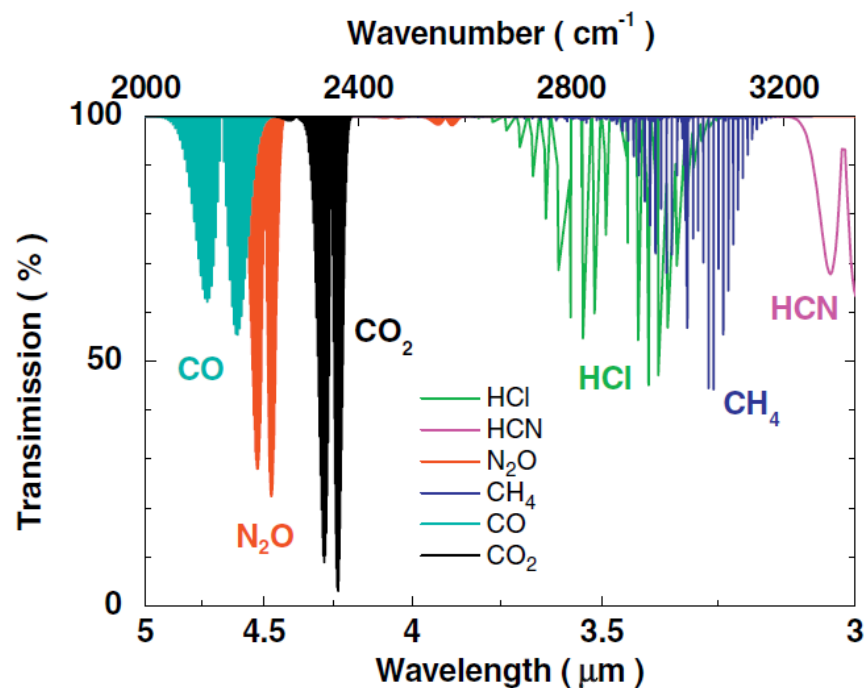
Fig. 1.1 Examples of some gas transmission spectra in the mid-infrared spectral range [5].

2

Mid-infrared laser emission at cryogenic temperatures was first demonstrated at 3.1 μm from InAs [6] and at 5.3 μm from InSb [7]. During the 1980's, many mid-IR devices were fabricated from narrow gap lead and lead-tin based IV-VI semiconductors. These are however limited by poor material quality and thermal conductivity which prevents continuous wave (CW) operation at room temperature (RT). Impressive results have been obtained recently with III-V semiconductor materials. The band gaps of ternary and quaternary semiconductors are dependent on their composition, which makes it possible to select appropriate compositions to achieve a given emission wavelength. Substantial progress has been made in the growth of antimonides, in particular GaInAsSb and InAsSb by using MOCVD and MBE. However, the performance of bulk semiconductor laser sources is possibly limited by stronger Auger recombination in the mid infrared range. Inter-valence band absorption (IVBA) and Shockley-Read-Hall (SRH) recombination all work to reduce the efficiency and maximum operating temperature of mid-infrared devices.
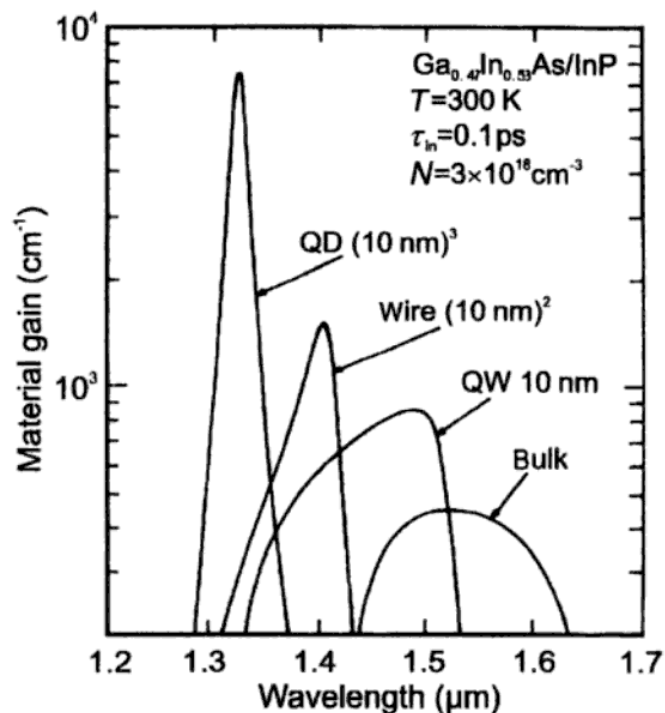
Fig. 1.2 Calculated gain spectra for the GaInAs/InP QD, wire, QW and bulk material at T = 300 K [3]**.**

In recent years, QW lasers in the mid-infrared range have made significant progresses in reducing the threshold current density, increasing maximum working temperature and output power [8][9]. Moreover, the quantum cascade lasers (QCLs) and interband cascade lasers (ICLs), which make use of the inter sub-band transition, have achieved superior performance. However, these types of devices suffer from lower wall plug efficiency and higher turn-on voltages than QW lasers. In addition, typical QCLs and ICLs are composed of hundreds of thin layers, making the growth and fabrication more challenging. From theoretical studies, due to their discreet density of states, QDs have higher material gain, narrower gain spectrum (Fig. 1.2), and are less temperature sensitive than QWs [3], making them the ideal candidate as the gain medium in semiconductor lasers. Compared with QCLs and ICLs, QD lasers also have the advantage of less complicated growth and processing steps. Despite of all these potential merits, to date there are still very few reports on QD lasers in the mid-infrared range due to the very limited choices of material systems, and their performance is still far behind the aforementioned types of lasers.

This thesis focuses on the InSb QDs emitting in the mid-infrared range and investigates their potential as an improved gain medium in bipolar laser diodes. The first section introduces the theoretical concepts and fundamentals on semiconductors, quantum nanostructures and lasers, followed by the description of experimental tools and techniques used to carry out the studies in this work. Then a detailed review and comparison of different types of mid-infrared laser sources will be given. The results of this work are divided into 3 chapters. The first part demonstrates the integration of In(As)Sb/InAs QDs onto the GaAs substrates using different metamorphic buffer layers. This type of QDs, which relies on the As-to-Sb exchange reaction, has only been grown on InAs substrates previously. Growing the QDs on GaAs substrates can make use of the more mature and inexpensive material platform, giving more possibility in device applications. Various characterization techniques were used to examine the QDs quality and the influence of dislocations. The problem of thermal leakage of confined carriers out of the QDs was identified. Light emitting diode (LED) structures containing these

In(As)Sb QDs in the active region were subsequently fabricated and electroluminescence from the QDs was obtained and studied. In the following chapter, the optical and structural characteristics of the QDs are discussed in detail. The QD size and composition were estimated with the help of simulations. The possible confined energy states were also calculated. The QD wavelength shift with temperature was observed. Finally, In(As)Sb QD laser diodes emitting at around 3.1 µm in pulsed operation were demonstrated. By using an improved structure design, the highest working temperature was significantly enhanced compared with previous works. The gain of the QDs and the loss in the waveguide were analysed. Possible contributions to the waveguide loss were examined. The reasons for shorter wavelength lasing compared with PL were explained. The leakage current in the laser was discussed. The details of the laser wavelength tuning with temperature and injection current were also investigated.

2. Theory and fundamental concepts

2.1 Energy bands in semiconductors

Solid state semiconductor materials can be single crystalline, where the atoms are arranged in a perfectly periodic structure in all three dimensions; polycrystalline, where there are many small regions of single crystalline materials called grains; or amorphous, where there is no periodic structure. The semiconductors studied in this work, unless specified, are all single crystalline materials.

In isolated free atoms, electrons can only exist in discreet energy levels. In bulk semiconductor materials, atoms are placed very close to each other in a periodic manner. The discreet energy levels evolve into continuous energy bands. The majority of the electrons stay in the band with lower energy (valence band). While some of the electrons can be excited to the band with higher energy (conduction band). Between the conduction band and valence band, there is a band gap in which there are no electron states. The differences in the energy bands between insulators, conductors and semiconductors are illustrated in the Fig. 2.1 below.
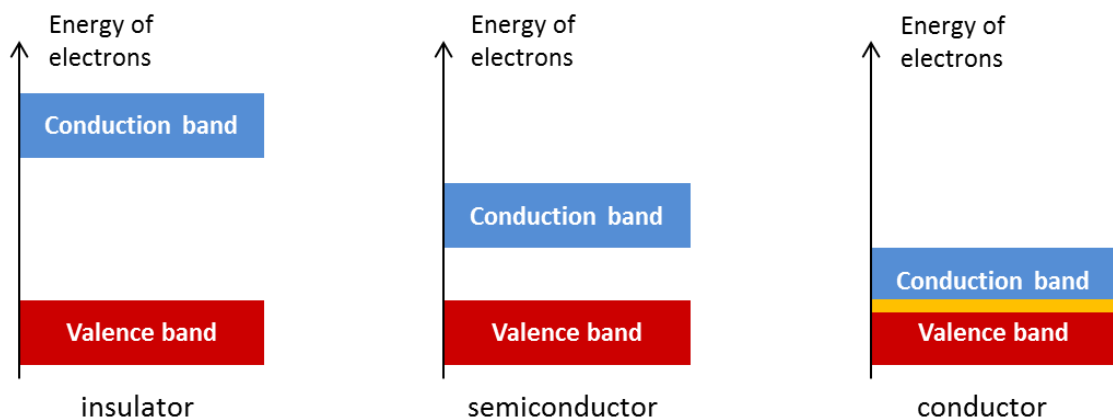
Fig. 2.1 Illustration of energy bands in bulk solid materials. The yellow part for conductor indicates the overlap between conduction and valence bands [10]**.**

In insulators there is a wide energy gap between the conduction and valence bands. The electrons can only stay in the valence band at any ordinary temperature. In semiconductors,

the band gap is significantly narrower than in insulators. A small portion of the electrons can be thermally excited to the conduction band. Under external excitations, the density of electrons on the conduction band can drastically increase, resulting in a big change of its various physical properties. In the conductors, the conduction band and valence band overlap with each other. Large number of free electrons naturally exists in the material. As will be discussed later, the band gap in semiconductors is a crucial factor for the optical and electrical properties of the structures and devices [10].

2.1.1 Direct and indirect band semiconductors

The band diagrams shown in Fig. 2.1 are very simplified representations of the rather complex band structures. More realistic semiconductor band structures are shown in Fig. 2.2 for two different cases. In case (a), the conduction band minima and the valence band maxima are located at the same momentum value, so the transition between conduction and valence band can happen without the change of momentum. This kind of semiconductors are called direct semiconductors, examples include GaAs, InAs and InP. In direct semiconductors, the transition of electrons from the conduction band to the valence band can result in the emission of photons with energy equal to the band gap E_g. On the other hand, in case (b), the conduction band minima and the valence band maxima do not have the same momentum value, and the material is called indirect semiconductors. The recombination in indirect semiconductors is difficult to result in the emission of photons [11].
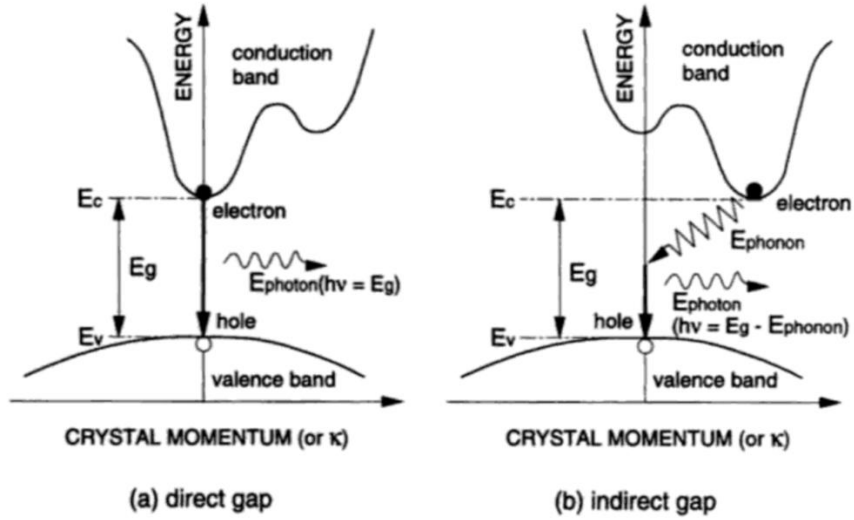
Fig. 2.2 the electron energy versus momentum plot at the bottom of conduction band and the top of valence band for case (a): direct semiconductors and case (b): indirect semiconductors [11]**.**

2.1.2 Electronic states

The outer electrons of the atoms in a bulk semiconductor material are delocalized over the whole crystal. The wave functions of the electrons can be described by Bloch wave functions:

$$\psi(\boldsymbol{r}) = \mu_k(\boldsymbol{r})\exp[j(\boldsymbol{k} \cdot \boldsymbol{r})] \tag{2.1}$$

where $\mu_k(\boldsymbol{r})$ has the periodicity of the crystal lattice, $\boldsymbol{r}$ is position and $\boldsymbol{k}$ is the wave vector. Comparing it with the Schordinger equation, it can be found that the solution of equation (2.1) indicates that the eigenvalues of the electron energy $\boldsymbol{E}$ are a function of $\boldsymbol{k}$, the values of which fall within certain allowed bands. Within the parabolic approximation, the $\boldsymbol{E}$ versus $\boldsymbol{k}$ relation can be written as:

$$E_c = \frac{\hbar^2 k^2}{2m_c} \tag{2.2}$$

for the conduction band $\boldsymbol{E_c}$, where $m_c = \hbar^2/(d^2E_c/dk^2)_{k=0}$ is the effective mass of electrons at the bottom of the conduction band. In the same manner, the valence band $\boldsymbol{E_v}$ verses $\boldsymbol{k}$ relation is:

$$E_v = \frac{\hbar^2 k^2}{2m_v} \tag{2.3}$$

where $m_v = \hbar^2/(d^2 E_v/dk^2)_{k=0}$ is the effective mass of electrons at the top of the valence band. The E verses k relations for conduction band and valence band are illustrated in Fig. 2.3, where E_g equals the energy difference between the bottom of the conduction band and the top of the valence band [12].
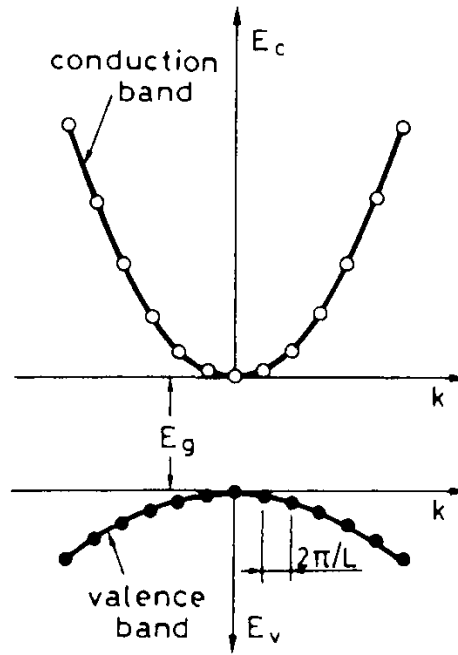
**Fig. 2.3 Energy verses k relation for a bulk semiconductor** [12].

2.1.3 Density of states

The number of energy states *p(k)* whose *k* value fall in the range between 0 and *k* can be derived by dividing the volume of the sphere *4πk³/3* with the volume of the unit cell *(2π)³/LₓLᵧL_z*, and multiplying by a factor of two for the two electron spin states:

$$p(k) = \left(\frac{k^3 V}{3\pi^2} \right) \tag{2.4}$$

9

where $V=L_xL_yL_z$ is the volume of a unit cell. The density of states (DOS) per unit volume can be calculated as:

$$\rho_{c,v} = \frac{dp}{V\,dk} = \frac{k^2}{\pi^2} \tag{2.5}$$

which is valid for both conduction and valence band. The density of states in terms of electron/hole energy can also be calculated as:

$$\rho_c(E_c) = \frac{1}{2\pi^2}\left(\frac{2m_c}{\hbar^2}\right)^{3/2} E_c^{1/2} \tag{2.6a}$$

$$\rho_v(E_v) = \frac{1}{2\pi^2}\left(\frac{2m_v}{\hbar^2}\right)^{3/2} E_v^{1/2} \tag{2.6b}$$

where E_c and E_v are measured from the bottom of the conduction band and the top of the valence band, upward and downward respectively. And the values of DOS for electrons and holes both increase with their respective energies [12].

2.1.4 Level occupation

Under equilibrium conditions, the probability of an electron occupying a given energy state E' can be described by Fermi-Dirac equation:

$$f(E) = \frac{1}{1 + exp[(E - E_F)/kT]} \tag{2.7}$$

where E_F is the energy of the Fermi level, k is the Boltzmann constant and T is the absolute temperature. For un-doped semiconductors E_F is located approximately in the middle of the energy gap. Thus for T > 0, only a small fraction of electrons can occupy the states in the conduction band.

This situation can be largely changed if the material is doped or externally excited. When the semiconductor is n-doped, large number of electrons would exist at the bottom of the conduction band, moving the quasi Fermi level E_F up into the conduction band (Fig. 2.4a). In

the case of p-doping, the absence of electrons on top of the valence band results in the E_F moving down into the valence band, leaving large number of holes in the bottom of the valence band (Fig. 2.4b). When both electrons and holes are externally injected into the material (e.g. in the middle of a *p-i-n* diode), at the same time electrons and holes can occupy the bottom of the conduction band and the top of the valence band respectively, resulting in a large separation of quasi Fermi levels of electrons E_{Fc} and of holes E_{Fv} (Fig. 2.4c) [13].


(a)   **(b)**   **(c)**
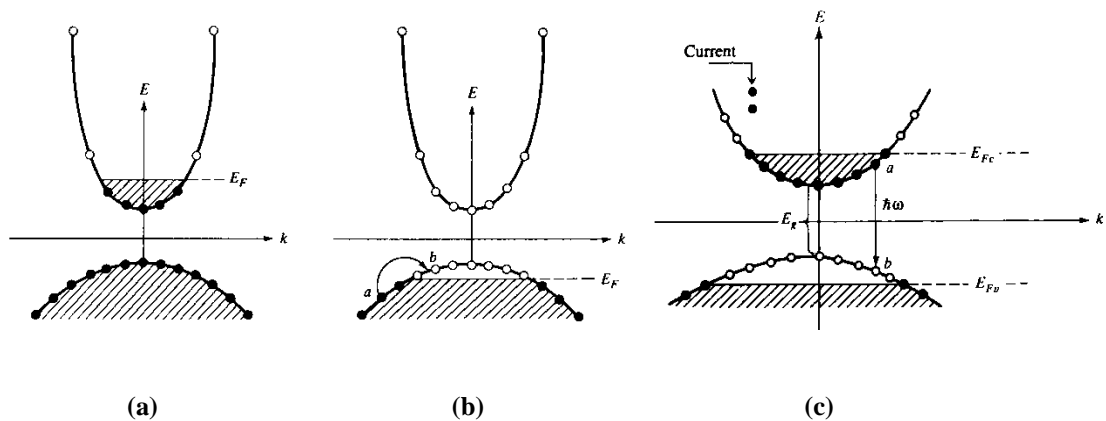
Fig. 2.4 Energy bands and quasi Fermi levels in (a) n-doped semiconductors, (b) p-doped semiconductors and (c) in a *p-i-n* diode with external current injection [13]**.**

2.1.5 Band alignments

When two different semiconductors come into contact in a hetero-interface, forming a sandwich structure, different types of band alignments will happen depending on the differences on the electron affinities and band gaps of the two semiconductors.

2.1.5.1 Type I band alignment

In the type I band alignment, the conduction band (E_c) of the material in the middle is lower than that of the material outside, and the valence band (E_v) of the material in middle is higher than that of the material outside, as is illustrated in the diagram below. In this band alignment, both excited electrons in the conduction band and excited holes in the valence band tend to concentrate within the material in middle, in which most of the two types of carriers would recombine.

11
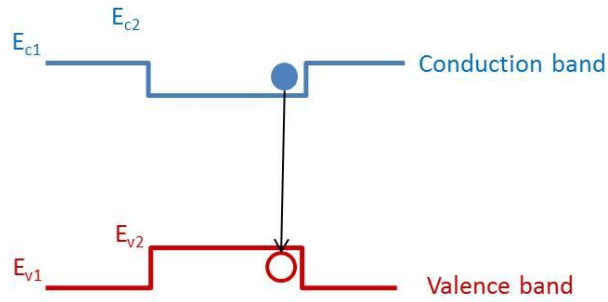
Fig. 2.5 Illustration of type I band alignment.

2.1.5.2 Type II band alignment

In type II band alignment, either both the conduction band and valence band of the material in the middle is higher than those of the material outside, as shown in Fig. 2.6 (a), or both of them are lower than those of the material outside, as shown in Fig. 2.6 (b). In any of these two situations, only one type of carriers tend to concentrate in the middle, and recombination happens between electrons and holes in separated locations.

(a)   (b)
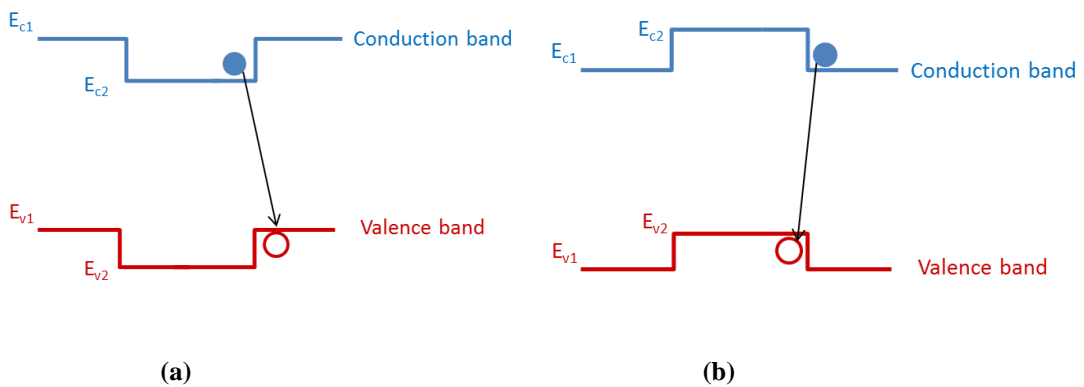
Fig. 2.6 Two situations of type II band alignments. (a): only the holes are concentrated in the centre, (b): only the electrons are concentrated in the centre.

In some material combinations, it is also possible that the valence band of one material is higher than the conduction band of the other material (e.g. InSb/InAs), creating a broken type II band alignment, shown in Fig. 2.7.

12
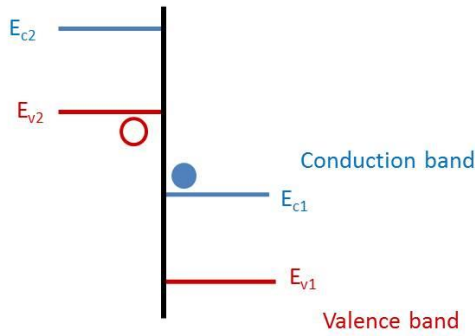
Fig 2.7 Illustration of broken type II band alignment.

2.1.6 Band bending in p-n junctions

In reality, the interface of two materials would not have the abrupt change of bands, as shown in Figs. 2.5-2.7. Instead, the bending of the energy bands will take place at the hetero-interface.

Fig. 2.8 shows the energy band profile of a p–n junction before the layers are brought into contact. The subscripts 1 and 2 refer to the p-type and n-type layers respectively. E_c and E_v denote conduction and valence bands. F is the Fermi level and δ is the difference between the band edge and the Fermi level. The electron affinity χ is the energy required to move an electron from the edge of conduction band to vacuum level and the work function Φ is the energy required to take an electron from the Fermi level to the vacuum level.
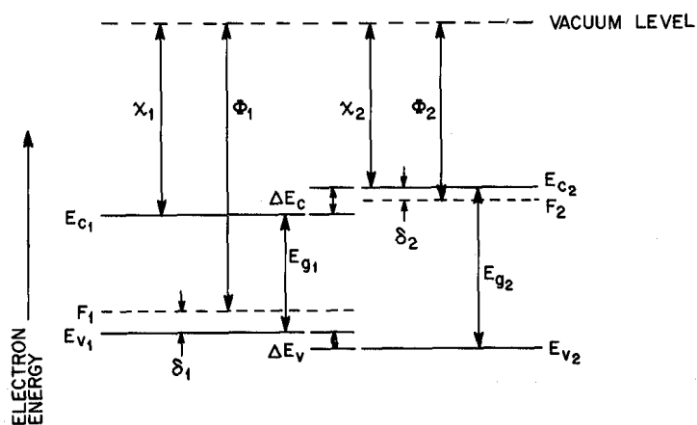

Fig. 2.8 The energy band profile of a p – n junction before the materials are brought into contact [14].

From Fig. 2.8, it is clear that the conduction band discontinuity is given by the difference in electron affinities

$$\Delta E_c = \chi_1 - \chi_2 \tag{2.8}$$

$$E_{g2} = \Delta E_c + E_{g1} + \Delta E_v \tag{2.9}$$

From equation 2.2, the discontinuity in valence band can be deducted as:

$$\Delta E_v = (E_{g2} - E_{g1}) - \Delta E_c \tag{2.10}$$

From equation 2.3, it can be noticed that:

$$\Delta E_v + \Delta E_c = E_{g2} - E_{g1} \tag{2.11}$$

When the two semiconductors are brought into contact, the Fermi level must be constant throughout the structure at thermal equilibrium, as shown in Fig 2.9.
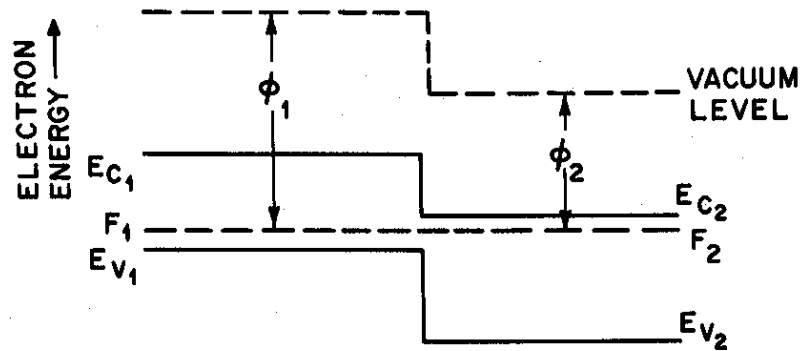
Fig. 2.9 The energy band profile of a p–n junction after the materials are brought into contact showing the constant Fermi level [14]**.**

For the p-n junction, since the density of the majority carrier on one side is much greater than the density of the minority carriers on the other side, the electrons will diffuse from the n-side to the p-side, and the holes will diffuse from the p-side to the n-side. These two types of carriers will recombine, leaving a depleted space-charge region near the hetero-interface where there exist charged immobile acceptors and donors, as illustrated in Fig. 2.10.
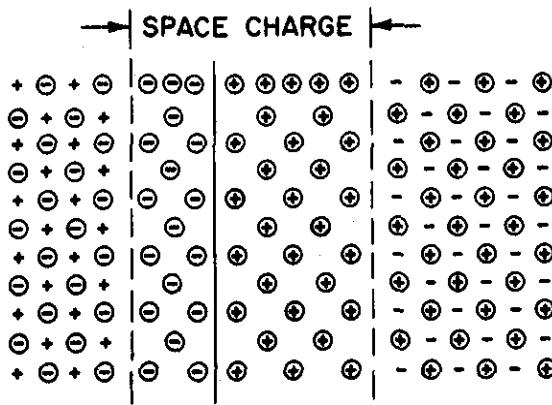
Fig. 2.10 The depleted space-charge region near the heterointerface of a p – n junction [14]**.**

The relative width of this region on the p-side and the n-side may be different, depending on the dielectric permittivities, the built-in potentials and the density of ionised donors and acceptors. This region creates a built-in field, which stops the carrier from diffusing into the opposite side. The energy diagram in Fig. 2.9 must be modified because of this built-in field, shown in Fig. 2.10. The method of calculating the band diagram is often called the Anderson model [15]. In Fig. 2.11, V_{Dp} and V_{Dn} are the built-in potentials on the p-side and n-side respectively. The interfacial energy spikes are a natural result of the abrupt interface where the Fermi level must be constant when in equilibrium [16].
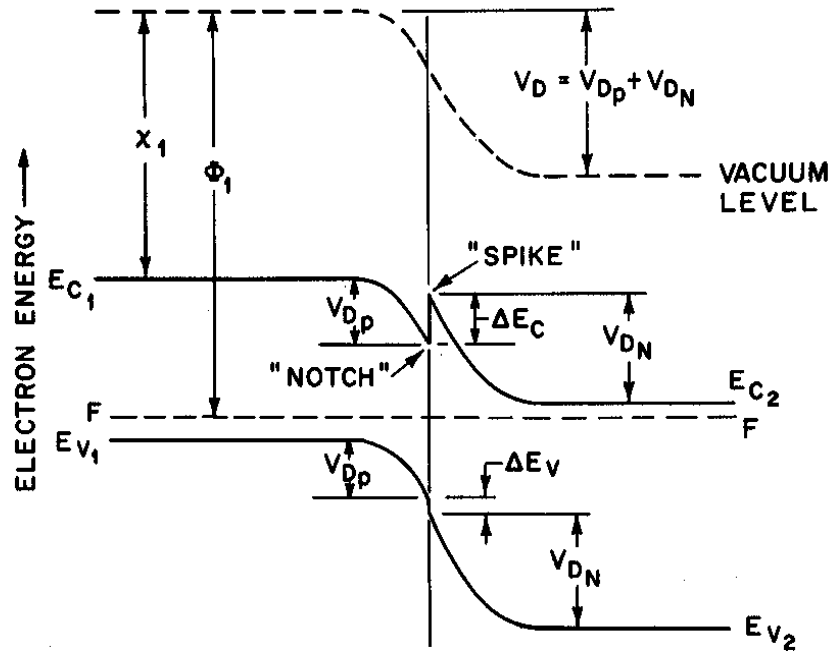
Fig. 2.11 The energy band diagram for a p–n junction showing the band bending at the interface. Terms are defined the same as in Fig. 2.8 [14]**.**

2.2 III-V semiconductors and alloys

At present, III–V compound semiconductors provide the materials basis for a number of well-established commercial technologies, as well as novel classes of electronic and photonic devices. Just a few examples include diode lasers, LEDs, photo-detectors, electro-optic modulators, and frequency-mixing components. The operating characteristics of these devices depend critically on the physical properties of the materials. Because ternary and quaternary alloys may be included in addition to the binary compounds, and the materials may be layered in all varieties of configurations, an almost limitless flexibility is now available in designing hetero-structure devices [17].

2.2.1 Band gaps

The zinc blende crystal consists of two interpenetrating face-centred-cubic lattices, one having a group-III element atom (e.g., Ga) and the other a group-V element atom (e.g., As). A zinc

blende crystal is characterized by a single lattice constant *a*. Most of the III-V semiconductors have zinc blende crystal structure, except for some of the III-nitride materials. The Γ-valley band gaps versus their lattice constants of the 12 zinc blende binary III-V materials are plotted in Fig. 2.12.
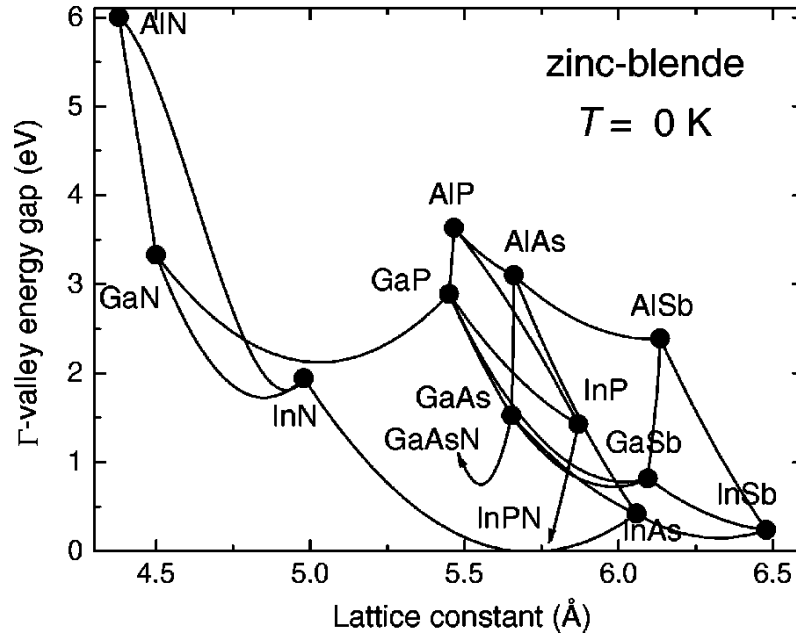
Fig. 2.12 Direct Γ -valley energy gap as a function of lattice constant for the zinc blende form of 12 III–V binary compound semiconductors (points), and some of their random ternary alloys (curves) at zero temperature [17].

Among all the binary III-V semiconductors, only InAs and InSb have the band gaps corresponding to mid-infrared range. InSb has the narrowest band gap of 0.24 meV, corresponding to a wavelength of 5.17 μm. The lattice constant of InSb is 6.479 Å, the largest of the binary materials shown on the graph. InAs has the second narrowest band gap (0.415 meV) among these materials.

The band gaps of ternary and quaternary alloys can be estimated by interpolating the binary semiconductors [18]:

$$T_{ABC}(x) = xB_{AB} + (1 - x)B_{AC} + x(x - 1)C_{ABC} \qquad (2.12)$$

17

for the ternary materials in the form of AB_xC_{1-x}, where $\boldsymbol{B_{AB}}$ and $\boldsymbol{B_{AC}}$ are the band gaps of the binary materials AB and AC, and $\boldsymbol{C_{ABC}}$ is the bowing parameter. In the case of quaternary material $AB_xC_yD_{1-x-y}$, the band gap becomes:

$$Q_{ABCD}(x,y) = xB_{AB} + yB_{AC} + (1 - x - y)B_{AD} - xyC_{ABC} \tag{2.13}$$
$$- x(1 - x - y)C_{ABD} - y(1 - x - y)C_{ACD}$$

Equally, in the case of $A_xB_{1-x}C_yD_{1-y}$,

$$Q_{ABCD}(x,y) = \frac{x(1 - x)[yT_{ABC}(x) + (1 - y)T_{ABD}(x)}{x(1 - x) + y(1 - y)} \tag{2.14}$$
$$+ \frac{y(1 - y)[xT_{ACD}(y) + (1 - x)T_{BCD}(y)}{x(1 - x) + y(1 - y)}$$

Instead of the discreet band gap values for binary materials, ternary and quaternary alloys can provide continuous tuning of band gap values, giving much more freedom in the design of semiconductor devices. Some examples of the ternary alloys' band gaps are shown by the curves in Fig. 2.12.

2.2.2 Refractive indices

The refractive indices of ternary and quaternary materials are also dependent on the compositions. For quaternary alloys, the refractive index $\boldsymbol{n}$ for photon energy $\boldsymbol{\hbar\omega}$ below the direct band gap $\boldsymbol{E_0}$ can be estimated by [19]:

$$n = \sqrt{A\left[f(x_0) + 0.5\left(\frac{E_0}{E_0 + \Delta_0}\right)^{1.5} f(x_{0s})\right] + B} \tag{2.15}$$

with

$$f(x_0) = x_0^{-2}\left(2 - \sqrt{1 + x_0} - \sqrt{1 - x_0}\right)$$

$$f(x_{0s}) = x_{0s}^{-2}\left(2 - \sqrt{1 + x_{0s}} - \sqrt{1 - x_{0s}}\right)$$

18

$$x_0 = \hbar\omega/E_0, \qquad x_0 = \hbar\omega/(E_0 + \Delta_0)$$

where E_0 is the direct band gap and Δ_0 is the spin-orbit splitting energy, $\hbar\omega$ represents the transition energy, A and B are the linear interpolations of binary data, the values can be found in [19]. The calculated photon energy dependent refractive indices of $InP_xAs_ySb_{1-x-y}$ lattice matched with InAs are shown in Fig. 2.13 below [20].
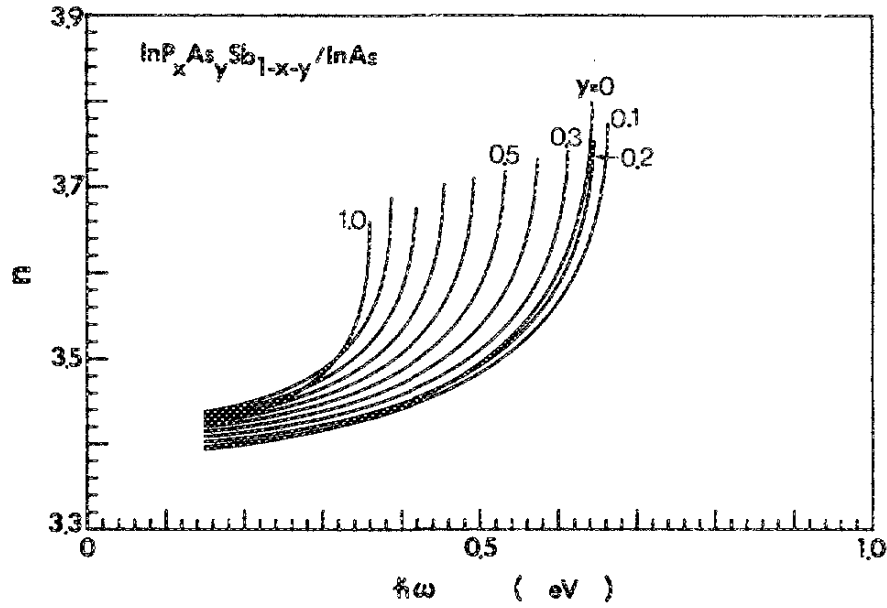

Fig. 2.13 calculated refractive indices of $InP_xAs_ySb_{1-x-y}$/InAs as a function of the photon energy with y-composition increment of 0.1 [20].

2.3 Recombination mechanisms in semiconductors

Under non-equilibrium conditions, excess carriers exist in the semiconductors. To restore the equilibrium condition, excessive electrons in the conduction band will recombine with holes in the valence band, either radiatively or non-radiatively.

2.3.1 Radiative recombination

During the radiative recombination process, the energy of the recombined electron-hole pairs is used to generate photons. In order to generate photons, the creation of excess electrons and holes can be achieved by various methods, i.e. bombardment with energetic electrons, ions or

19

other particles. In experiments, the most common methods are: photo-luminescence – the radiative recombination of excess carriers which are generated by the absorption of light, and electro-luminescence – the radiative recombination of excess carriers which are generated by electrical injection [21]. Different radiative recombination mechanisms are illustrated in figure 2.14 below.
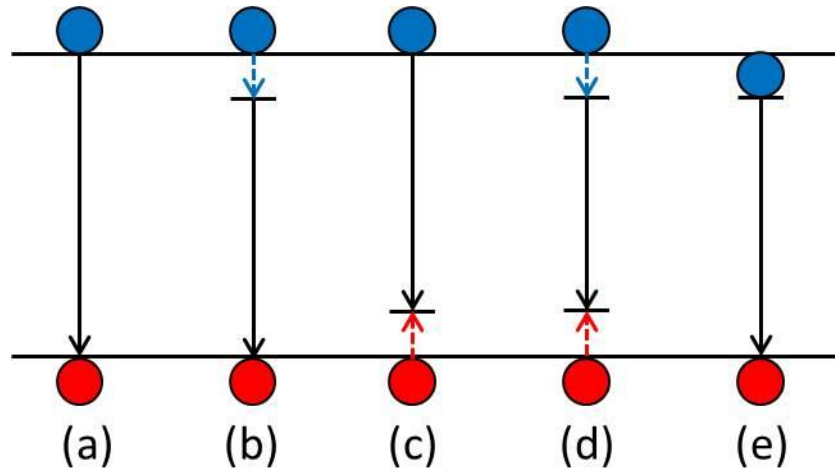
Fig. 2.14 Radiative recombination mechanisms in semiconductors. (a) band-to-band recombination, (b) donor-to-valence band recombination, (c) conduction band-to-acceptor recombination, (d) donor-to-acceptor recombination and (e) exciton recombination. The blue and red circles represent electrons and holes respectively. Straight line arrows and dotted vertical lines represent photon and phone emissions respectively.

2.3.1.1 Band-to-band recombination

Band to band recombination is the process in which an electron on the conduction band recombines with a hole on the valence band and emits a photon whose energy equals:

$$h\nu = E_g + kT/2 \qquad (2.16)$$

where *kT/2* accounts for the thermal effects. The rate of the band to band recombination can be written as:

$$R = -\frac{dn}{dt} = -\frac{dp}{dt} = Bnp \qquad (2.17)$$

where *n* and *p* are the densities of free electrons and holes in the semiconductor respectively and the constant *B* is the bimolecular recombination coefficient. The typical value of *B* for direct band gap III-V semiconductors is in the range of $10^{-11} - 10^{-9}$ cm^3/s [22]. For indirect semiconductors, radiative band to band transition requires the participation of phonons, which is much less likely to happen and the value of B is much smaller ($10^{-15} - 10^{-14}$ cm^3/s) [21].

2.3.1.2 Free-to-bound recombination

Donors and acceptors in the semiconductors can introduce energy states within the band gap, either close to the conduction band for donors or close to the valence band for acceptors. Other than the band-to-band recombination, radiative processes can also happen between electrons on the donors' state and holes on the valence band (Fig. 2.14b), or between electrons on the conduction band and holes on the acceptor' state (Fig. 2.14c). The energy of the emitted photons is:

$$h\nu = E_g - E_i \tag{2.18}$$

Compared with equation 2.16, the additional term E_i represents the ionization energy of the donors or acceptors. For most direct band gap semiconductors, the donor/acceptor related recombination can be more clearly observed at low temperatures [16]. With increasing temperature, donor-to-band and band-to-acceptor recombination shows a quicker decay compared with band-to-band transition, due to the thermal excitation of carriers out of the donor/acceptor states [23].

2.3.1.3 Donor-to-acceptor recombination

Radiative recombination can also happen if the density of both donors and acceptors are substantial ($\sim 10^{16}$ cm^{-3}). The electrons in the donors can recombine with holes in the accpectors, both within the energy gap, as illustrated in Fig. 2.11d. The emitted photon energy equals:

$$hv = E_g - (E_D + E_A) + {e^2}/{\varepsilon r} \tag{2.19}$$

where E_D and E_A are the ionization energy of donors and acceptors respectively. The last term in this equation represents the Coulomb force between carriers on the donor and acceptor states, in which ε is the static dielectric constant and r is the donor-acceptor separation. Similar to donor–to-band and band-to-acceptor recombination, the donor-acceptor recombination can only be clearly seen at low temperatures [16].

2.3.1.4 Exciton recombination

Excitons are electron-hole pairs held together through Coulomb interactions. For free excitons, the energy of the emitted photon from an exciton recombination is:

$$hv = E_g - E_{exc} \pm KE_p \tag{2.20}$$

where KE_p denotes the emission or absorption of K lattice phonons with the energy E_p. The value of E_{exc} is usually in the range of a few milli-electronvolts (meV). If the exciton is bounded next to a donor, acceptor or neutral atom (bound exciton), the energy of the emitted photon becomes smaller than the free exciton due to the lack of kinetic energy. The value becomes:

$$hv = E_g - E_{bx} - E_{exc} \tag{2.21}$$

where E_{bx} is the binding energy of the exciton to the impurity. E_{bx} is also in the range of a few meV. The spectrum of bound exciton emission is usually narrower than free exciton and band-to-band emission spectra. Both free and bound exciton emissions can only be significant at low temperatures, since at high temperature the thermal energy can far exceed the exciton binding energy [16].

2.3.2 Non-radiative recombination

Besides the emission of photons, the energy released from the recombination of electrons and holes can also be transferred in non-radiative forms. The most common non-radiative recombination mechanisms will be discussed in this section.

2.3.2.1 Auger recombination

During the Auger recombination, the released energy from an electron-hole pair recombination is used to excite another free electron to higher into the conduction band, or excite another hole deeper into the valence band. The excited electron or hole will quickly relax to the low energy end of their respective energy band through multiple phonon emissions. In this process, no photons are emitted. The three most common Auger recombination processes (CHCC, CHSH and CHLH) are schematically shown in the figure below.
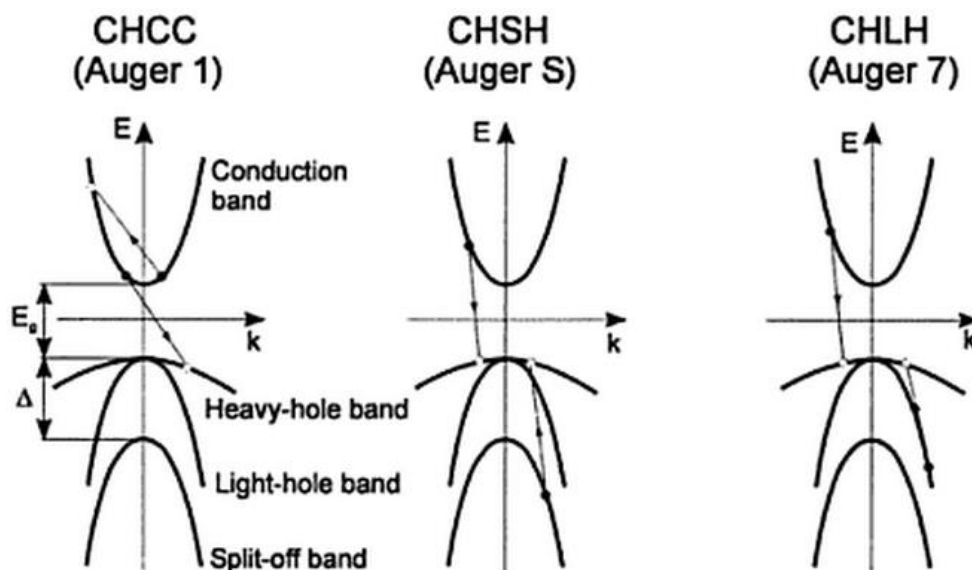

Fig. 2.15 CHCC, CHSH and CHLH Auger recombination mechanisms. In the CHCC process, one electron on the conduction band recombines with a hole on the valence band, transferring the energy to another free electron so that it moves higher on the conduction band. In the CHSH process, the energy from an electron-hole pair recombination is transferred to an electron on the split-off (SO) band and excites it to the heavy hole (HH) band. In the CHLH process, the energy from recombination lifts an electron from the light hole (LH) band to the heavy hole band [24]**.**

Because the CHCC process involves two free electrons, it is most prominent in n-type semiconductors. In materials where the spin split-off energy Δ is much larger than the band gap energy E_g (i.e. InSb and HgCdTe), the CHSH transition can be negligibly small compared with CHLH transition. However, in materials where Δ is close to E_g, the CHSH process is much more significant than CHLH (as in the case of InAs and InAsSb) [24].

At low external injection, the combined Auger generation rate of these three major processes can be simplified to:

$$(G - R)_A = \frac{n_i^2 - np}{2n_i^2} \left(\frac{n_o}{\tau_{A1}^i} + \frac{p_o}{\tau_{A7}^i} + \frac{p_o}{\tau_{AS}^i} \right)$$

(2.22)

where n_i is the intrinsic electron concentration, n and p represent the non-equilibrium carrier concentrations of electrons and holes respectively, n_o and p_o denote the carrier concentrations at equilibrium conditions. The three factors in the brace of the equation 2.22 represent the contributions from CHCC (A1), CHLH (A7) and CHSH (AS). τ_{A1}^i, τ_{A7}^i and τ_{AS}^i are the intrinsic Auger lifetime of the CHCC, CHLH and CHSH processes respectively. The values of the Auger lifetimes are all dependent on the carrier effective mass, the density of states, the band gap energy, and decrease drastically with carrier concentration.

In the high excitation range, the Auger recombination rate can be simplified as:

$$R_A = Cn^3$$

(2.23)

where n is the carrier concentration and the value of the Auger coefficient C is in the range of $10^{-28} - 10^{-29}$ cm^6/s for typical III-V semiconductors [22].

The Auger processes also features strong temperature dependence, since τ_{A1}^i, τ_{A7}^i and τ_{AS}^i are all functions of temperature T. With increasing T, the Auger rate tends to increase significantly [24]. In general, the Auger effect becomes more important with decreasing band gap energy. At 300 K, the Auger lifetime τ_A in InAs (E_g = 0.36 eV) can be as short as 10^{-9} s

with a low carrier concentration of 10^{17} cm^{-3}. However, in GaAs (E$_g$ = 1.42 eV), the Auger effect can only be significant with very high carrier concentration (10^{19} cm^{-3}) [16].

At last, it needs to be noted that the processes discussed above are all band-to-band Auger recombination. Similar Auger processes can also happen at donor/acceptor centres, in a similar manner to donor/acceptor related radiative recombination [21].

2.3.2.2 Shockley-Read-Hall recombination

In Shockley-Read-Hall (SRH) recombination, electrons and holes recombine via energy levels induced by impurities or lattice defects within the energy gap. As recombination centres, they trap electrons or holes; as generation centres, they emit carriers [24]. When the holes are in majority, conditions are close to equilibrium, the SRH lifetime can be estimated by assuming electrons and holes have the same capture cross sections ($\sigma_n = \sigma_p$) and thermal velocities ($v_n = v_p$):

$$\tau_{SR} = \tau_{n0}\left(1 + \frac{p_o + p_1}{p_o + n_o}\right) \tag{2.24}$$

where τ_{n0} equals $1/N_T v_n \sigma_n$. Similar estimations can also be made when the electrons become the majority carrier. In the particular case of intrinsic material (i.e. $n_0 = p_0 = n_i$), the SRH rate becomes:

$$\tau_i = \tau_{n0}\left(1 + cosh\left(\frac{E_T - E_{Fi}}{kT}\right)\right) \tag{2.25}$$

where E_{Fi} is the intrinsic Fermi level, which is typically near the middle of the band gap. If it equals the energy level of the traps ($E_{Fi} = E_T$), τ_i reaches the minimum value $2\tau_{n0}$, which means the traps with energy levels close to the middle of the band gap can act as more efficient SRH recombination centres. Equation 2.25 also indicates with increasing temperature, the SRH lifetime decreases, resulting in lower radiative recombination efficiency [22].

2.3.2.3 Inter-valence band absorption

The inter-valence band absorption (IVBA) process happens when the photon generated from electron-hole recombination is re-absorbed by lifting an electron in the spin split-off band to an injected hole state in the heavy hole band (Fig. 2.16). The IVBA can be significant in materials where the energy gap between spin split-off band and heavy hole band is close to the band gap E_g. The dashed arrows in Fig. 2.16 shows with increasing band gap E_g, the re-absorption needs to happen at larger wavevector k, making the process less likely [25].
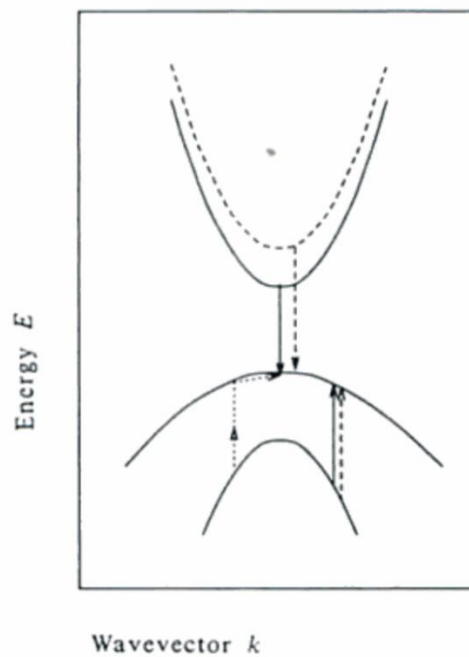
Fig. 2.16 Inter-valence band absorption mechanisms. The solid arrows indicate direct IVBA process, while the dotted arrows indicate phonon-assisted IVBA. The dashed arrows indicate how IVBA moves to larger wavevector k and is thereby reduced with increasing band gap E_g [25].

2.3.2.4 Free carrier absorption.

Free carrier absorption (or intra-band absorption) happens when a photon gives up its energy to an electron already in the conduction band or a hole in the valence band, thus raising it to a higher energy (as illustrated in Fig. 2.17). Usually free carrier absorption also includes the absorption in which electrons/holes are excited from the shallow donor/acceptor states near

the band edges into the conduction/valence band. For energies sufficiently lower than the band gap energy, free carrier absorption can become the dominant recombination mechanism. The rate of free carrier absorption is proportional to the carrier concentration, since one free carrier is required for an absorption event. According to Drude free electron model, free carrier absorption increases as the square of the wavelength:

$$\alpha_{fc} = N\lambda^2 \tag{2.26}$$

where N is the concentration of electrons or holes and λ is the wavelength [22]. From this quadratic relation, it is obvious that the free carrier absorption is stronger at longer wavelength range. So in mid-infrared devices, the effect of free carrier absorption can possibly be more significant than in near-infrared and visible devices.
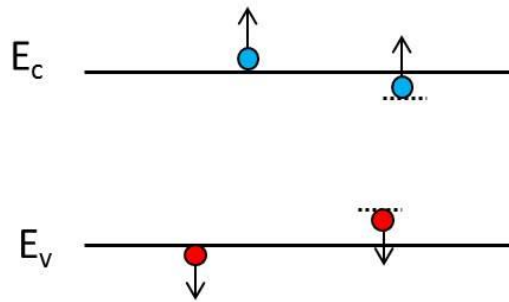
Fig. 2.17 Illustration of carrier transitions during free carrier absorption. Red dots: electrons, blue dots: holes, arrows: direction of carrier movement, short dotted lines: donor/acceptor states.

2.3.2.5 Surface recombination

Non-radiative recombination can occur at semiconductor surfaces, which are strong perturbations of the periodicity of a crystal lattice. From a chemical view point, due to the lack of neighbouring atoms, dangling bonds can be formed on the semiconductor surfaces. The dangling bonds create electronic states located in the forbidden gap, which can act as non-radiative recombination centres [22].

Recombination via these surface states can often dominate the device efficiency. The effect can be reduced by locating the p – n junction a distance greater than three times the diffusion length away from the surface [27].

2.3.3 Competition between radiative and non-radiative recombination

The mechanisms of the major non-radiative processes have been discussed, including Auger recombination, SRH recombination and surface recombination. Even though these non-radiative recombination rates can be reduced, they can never be totally eliminated. Besides, any semiconductor material contains some native defects which can induce non-radiative recombination. It is difficult to fabricate materials with impurity levels lower than parts per billion. Thus even the purest material contains impurity in the level of 10^{12} cm^{-3}.

If the total radiative recombination lifetime is denoted as τ_r and the total non-radiative recombination lifetime is denoted as τ_{nr}, the overall recombination rate can be given by:

$$\tau^{-1} = \tau_r^{-1} + \tau_{nr}^{-1} \tag{2.27}$$

The probability of radiative recombination or internal quantum efficiency is:

$$\eta_{int} = \frac{\tau_r^{-1}}{\tau_r^{-1} + \tau_{nr}^{-1}} \tag{2.28}$$

Note that not all photons emitted internally can escape from the semiconductor due to the light-escape problem and reabsorptions [22].

2.4 Semiconductor quantum dots

We have previously discussed the energy bands and carrier recombination mechanisms in bulk semiconductors, and the calculations are based on the assumption that the material is infinitely large in all dimensions. Once the sizes of the semiconductor materials are reduced to

considerably low levels, this assumption can no longer be legitimate, and the properties of the small sized materials (nanostructures) can be significantly different from the bulk materials.

2.4.1 Density of states in nanostructures

Within parabolic approximation, the relation between electron energy E and wave vector k in equations 2.2 and 2.3 can be rewritten as:

$$E = \frac{\hbar^2 k^2}{2m^*} \tag{2.29}$$

where m^* is the effective mass of electrons or holes. In this equation, k can be in any direction in the three dimensional (3D) space. If the semiconductor is reduced in size in one direction, becoming a quantum well, the wave vector can have freedom in the other two dimensions (2D). Boundary conditions need to be added to the Schrodinger equation 2.1, and the solved DOS becomes:

$$\rho^{2D} = \frac{k}{\pi}\left(\frac{2m^*}{\hbar^2}\right)^{1/2}\frac{E^{1/2}}{2} \tag{2.30}$$

By substituting k with E from equation 2.29, equation 2.30 becomes:

$$\rho^{2D} = \frac{m^*}{\pi\hbar^2} \tag{2.31}$$

which is a constant value independent of energy E. If there are many (n) confined states within the QW, then the DOS at any particular energy is the sum over all subbands below that energy. The density of states can be written as:

$$\rho^{2D} = \sum_{i=1}^{n}\frac{m^*}{\pi\hbar^2}\Theta(E - E_i) \tag{2.32}$$

where Θ is the unit step function.

For the case of quantum wires (i.e. the semiconductor is reduced in size in two directions), and quantum dots (i.e. the semiconductor is reduced in size in all three directions), different boundary conditions need to be applied to solve the Schrodinger equation. The derived DOS for a quantum wire is:

$$\rho^{1D} = \left(\frac{m^*}{\pi\hbar^2}\right)^{1/2}\frac{1}{\pi E^{1/2}} \tag{2.33}$$

for the case of multiple states confined in the quantum wire, the DOS at any particular energy can be written as:

$$\rho^{1D} = \sum_{i=1}^{n}\left(\frac{m^*}{\pi\hbar^2}\right)^{1/2}\frac{1}{\pi(E-E_i)^{1/2}}\Theta(E-E_i) \tag{2.34}$$

where E_i is the subband minima below the energy E.
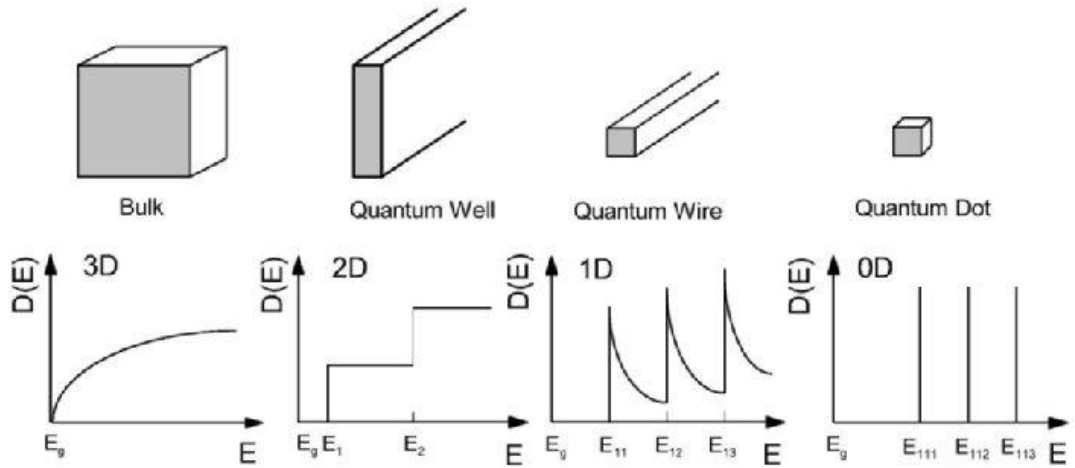
Fig. 2.18 Schematic evolution of the density of states from 3D bulk semiconductors to 2D quantum wells, to 1D quantum wires and to 0D QDs [28].

In the case of quantum dots (QDs), since there is confinement in all the three directions, the E verses k relation of equation 2.29 becomes:

$$E = \frac{\hbar^2}{2m^*}\left(\frac{n_x^2}{L_x^2} + \frac{n_y^2}{L_y^2} + \frac{n_z^2}{L_z^2}\right) \tag{2.35}$$

where L_x, L_y, L_z are the width of the QDs in the three directions, and n_x, n_y, n_z denote the number of states in the three directions. The energy inside a QD can only exist in discreet values. So the DOS are only dependent on the number of confined energy levels. One single isolated QD would therefore offer just two (spin-degenerate) states at the energy of each confined level, and the DOS versus energy would be a series of δ-functions. The comparison of the DOS in bulk materials (3D), quantum wells (2D), quantum wires (1D) and QDs (0D) is sketched in Fig. 2.18 [28].

2.4.2 Type I and type II quantum dots

Epitaxial semiconductor QDs are very commonly covered by another semiconductor material during the growth for device applications. In a similar manor to bulk semiconductors, the conduction and valence bands of the QDs can form type I and type II band alignments with the external material. The band alignments and recombination mechanisms are illustrated in Fig. 2.19.

In type I QDs, both the conduction band and the valence band of the outside material have higher energy than the QDs' material, electrons and holes are both confined within the QDs. As discussed in previous section, only discreet energy levels can exist in QDs, recombination happens between the carriers sitting on these energy levels (Fig. 2.19a). In type II QDs, only one kind of carriers are confined within the QDs, thus exist on quantized energy levels, and recombination happens either between the confined electrons in the QDs and free holes in the outside material (Fig. 2.19b), or between the confined holes in the QDs and electrons in the outside material (Fig. 2.19c).
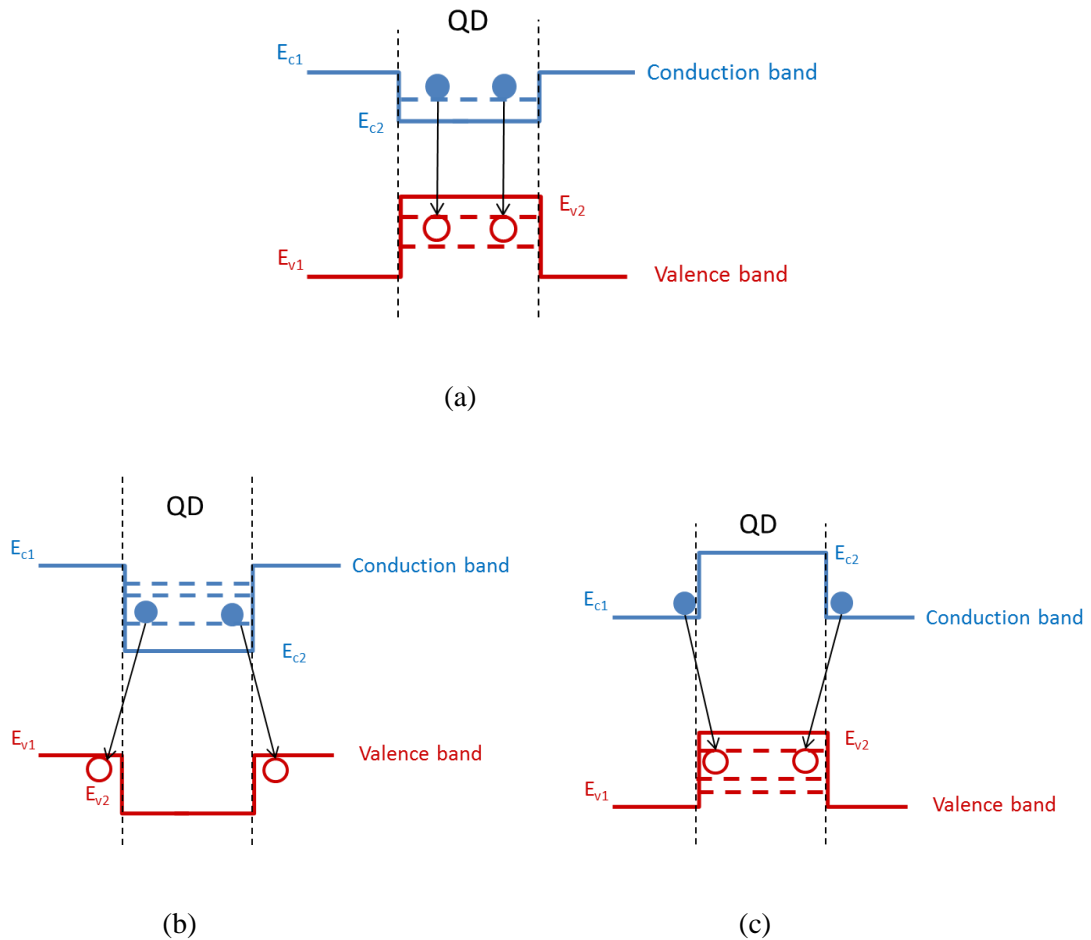
Fig. 2.19 Schematic diagrams of the band alignments and electron-hole recombination in (a) type I QDs, (b) and (c) type II QDs.

2.4.3 Fabrication of quantum dots

There have been a few different approaches in fabricating QDs. The first realization of QDs was the semiconductor inclusions in glass (e.g. CdSe), which has been commercially available as colour filters (Fig 2.20a). However, since this kind of QDs are electrically isolated, it is very difficult to integrate them in electronic or optoelectronic devices. QD nanostructures can also be fabricated using lithographic techniques (top-down), which is size-limited by the minimum feature lithography can produce. As shown in Fig 2.20b, one example of this approach is to grow thin GaAs layers between lattice-matched AlGaAs material and then etch out GaAs/AlGaAs QDs. The most heavily investigated method to make QDs is the self-

organized growth manner, in which QDs can naturally form during the growth of strained

hetero-structures (Fig 2.20c) [3].
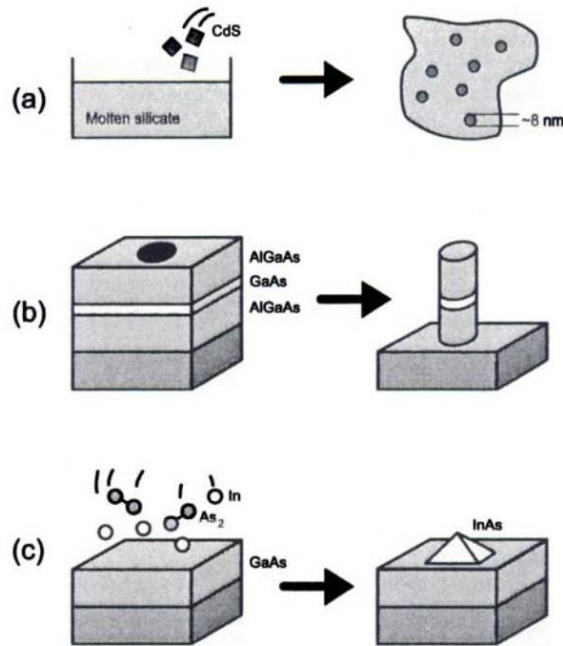
Fig. 2.20 Schematic representation of different approaches to the fabrication of QDs: (a) microcrystallite in glass, (b) artificial patterning of thin film strucutres, (c) self-organized growth of QDs [3]**.**

During the heterostructure deposition, either 2D films or 3D islands can be formed, depending

on the lattice mismatch between the two materials and the growth conditions. The most

common three modes of epitaxial growth are illustrated in Fig 2.21. In the Frank-van der

Merwe (FvdM) growth mode (Fig. 2.21a), the extension of smallest stable clusters of the

deposited material occur in two dimensions, resulting in the formation of planar films. The

atoms in this mode are more strongly bound to the substrate than to each other. In the Volmer-

Weber (VM) mode, shown in Fig. 2.21c, the smallest stable clusters nucleate on the substrate

surface and form 3D islands (QDs). It occurs when the atoms or molecules of the deposited

material are more strongly bound to each other than to the substrate. Lastly, the Stranski-

Krastanov (SK) growth mode, which is also called layer-plus-islands mode, is an intermediate

combination of the other two modes. After the initial formation of a few monolayers (often

called wetting layer) on the substrate, the 2D growth becomes unfavourable and 3D islands are automatically formed (Fig. 2.21b) [29]. However, the growth of the In(As)Sb QDs investigated in this work mainly relies on the As-Sb exchange reaction, which is different from the mechanism of SK QDs formation. The details will be given in the following chapter.

Frank-van der Merwe
(pseudomorphic)

Stranski-Krastanow
(pseudomorphic + 3D)

Volmer-Weber
(3D-Ilands)

(a)   **(b)**   **(c)**
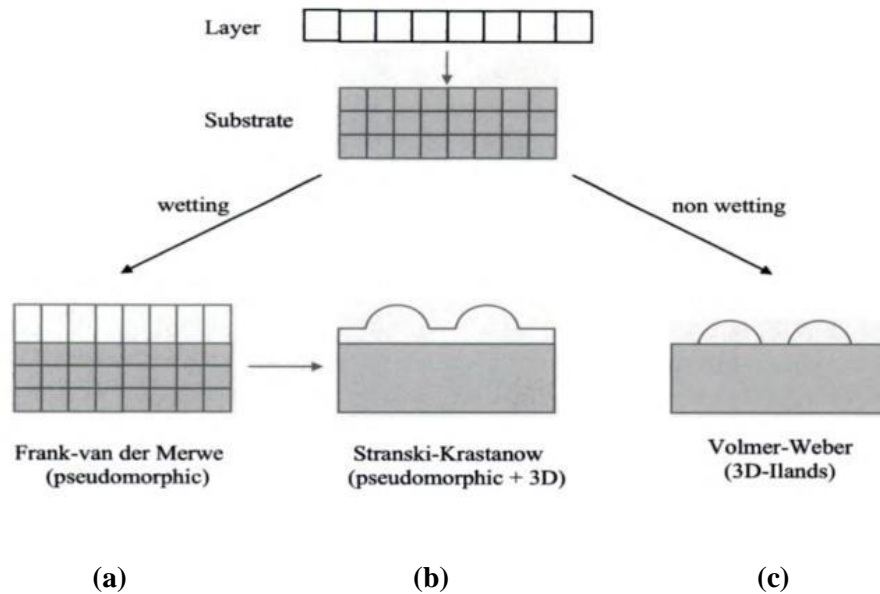
Fig. 2.21 Different epitaxial growth modes for strained layer growth. Left bottom: 2D growth of a strained layer, centre bottom: formation of 3D islands arising after wetting layer growth, right bottom: 3D islands formation without wetting layer [30]**.**

Among the most important parameters for QDs are the mean size and shape of QDs, the material composition, the QDs density and the size distribution, which are all dependent on the growth conditions. The epitaxial growth of various kinds of semiconductor QDs has now been widely made through MBE and MOCVD For III-V semiconductors, some examples of the epitaxial QDs material systems include: In(Ga)As/GaAs, GaSb/GaAs, InAs/InP, InP/InGaP, InSb/InAs and GaN/AlN.

2.5 Principle of lasers

There are three key parts in a typical laser system. Firstly, the laser should contain the gain medium which can amplify the light traveling through it. Secondly, there must be resonant optical cavities so that oscillation can happen. Thirdly, there must be means of excitation where the population of the energy levels is perturbed from equilibrium (Fig. 2.22). These three factors will be discussed in the following sections.
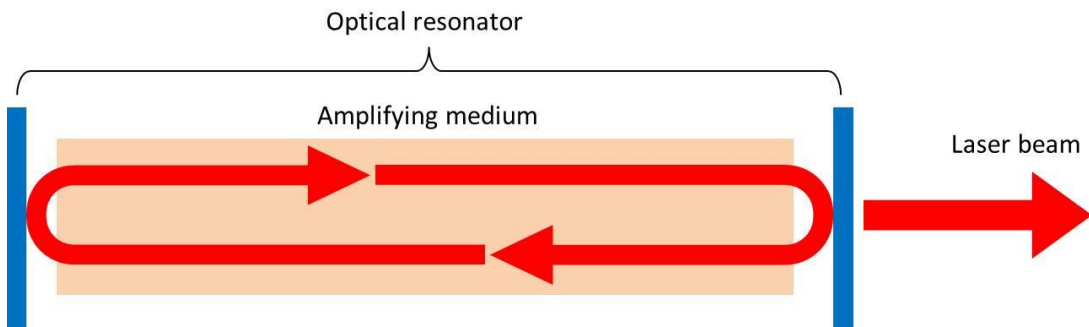

Fig. 2.22 simplified schematic of a typical laser.

2.5.1 Absorption, amplification and population inversion

In the case of a two-level atomic system as shown in Fig. 2.22, with the presence of an electro-magnetic field of energy $h\upsilon=E_2-E_1$, an atom can undergo the transition 2→1, absorbing a photon of energy $h\upsilon$ (Fig. 2.23a). If the atom happens to be in state 2, the stimulated transition 1→2 can happen, emitting a photon of the same energy $h\upsilon$ (Fig. 2.23c). The induced transition rate of 2→1 and 1→2 are equal, and proportional to the intensity of the electro-magnetic field. The total transition rate between these two states can be written as:

$$W'_{21} = B_{21}\rho(\upsilon) + A_{21} \tag{2.36}$$

$$W'_{12} = B_{12}\rho(\upsilon) \tag{2.37}$$

where B_{21} and B_{12} are constants to be determined, $\rho(\upsilon)$ is the energy density at that frequency and A_{21} represents the spontaneous transition of 2→1 (Fig 2.23b).
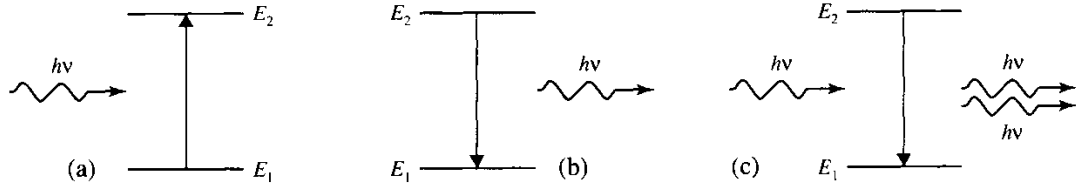
Fig. 2.23 Radiative processes: (a) absorption – an incident photon is absorbed while the atom jumps from state 1 to state 2; (b) spontaneous emission – a photon is emitted while the atoms descends from state 2 to state 1; (c) stimulated emission – an additional photon is emitted when an atomic system is under the action of an incident photon [32].

Under thermal equilibrium conditions, we have [33]:

$$\rho(v) = \frac{8\pi n^3 h v^3}{c^3} \frac{1}{e^{hv/kT} - 1} \tag{2.38}$$

In addition, the total number of atoms on state 1 and state 2 should keep stable. So

$$N_2 W'_{21} = N_1 W'_{12} \tag{2.39}$$

where N_1 and N_2 are the equilibrium population densities on these two states. W_{21}' and W_{12}' are the transition rates defined in equations 2.36 and 2.37. From Boltzmann statistics, the ratio between N_1 and N_2 should equal to:

$$\frac{N_2}{N_1} = e^{-hv/kT} \tag{2.40}$$

Using equations 2.36 – 2.40, we can obtain:

$$\frac{8\pi n^3 h v^3}{c^3 (e^{hv/kT} - 1)} = \frac{A_{21}}{B_{12} e^{hv/kT} - B_{21}} \tag{2.41}$$

which can only be valid when $B_{12}=B_{21}$, and $A_{21}/B_{21}=8\pi n^3 h v^3/c^3$. Substituting the parameters in to equations 2.36 and 2.37, we get the stimulated transition rate:

$$W'_i = \frac{c^3}{8\pi n^3 h v^3 t_{spon}} \rho(v) \tag{2.42}$$

where $t_{spon}=1/A_{21}$ is the spontaneous transition lifetime. $\rho(v)$ cannot be used to describe the radiation density in the case of narrow linewidth beams, and equation 2.42 can be re-written as:

$$W_i = \frac{\lambda^2 I_0}{8\pi n^2 h v t_{spon}} g(v)$$

(2.43)

where I_0 is the beam intensity and $g(v)$ is the laser's lineshape function. We note the induced transition rate is proportional to the beam intensity. In the absence of any dissipation mechanisms, the induced radiation will also be added to the beam. In a distance of dz:

$$\frac{dI_0}{dz} = (N_2 - N_1) \frac{c^2 g(v)}{8\pi n^2 v^2 t_{spon}} I_0$$

(2.44)

which gives the solution of:

$$I_0(z) = I_0(0) e^{\gamma(v)z}$$

(2.45)

and $\gamma(v)$ is the gain coefficient:

$$\gamma(v) = (N_2 - N_1) \frac{c^2 g(v)}{8\pi n^2 v^2 t_{spon}}$$

(2.46)

We notice that in order to have a positive gain coefficient, population inversion ($N_2 > N_1$) is required, which is a prerequisite for lasers. Otherwise, the intensity decreases, corresponding to light absorption [33].

2.5.2 Laser cavities
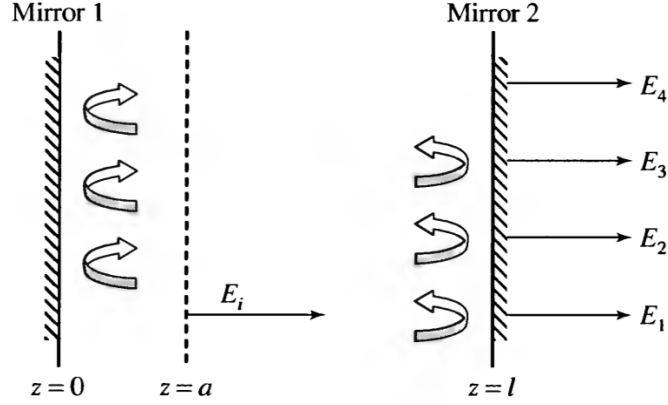
Fig. 2.24 Schematic drawing of multiple reflections inside a Fabry-Perot cavity and the corresponding partial transmission of the light beam [34]**.**

Considering Fig. 2.22, the simplest example of a laser cavity can consist of two parallel mirrors, which is basically a Fabry-Ferot etalon. As shown in Fig. 2.24, light between the two mirrors experiences multiple reflection and transmission. In the case of a random light source placed at position $z=a$ with amplitude of E$_i$, the total output of light from mirror 2 at $z=l$ can be written as:

$$E_{out} = E_1 + E_2 + E_3 + E_4 + \cdots \tag{2.47}$$

where

$$E_1 = t_2 e^{-ik'(l-a)} E_i$$

$$E_2 = \left(r_1 r_2 e^{-ik'l}\right) t_2 e^{-ik'(l-a)} E_i \tag{2.48}$$

$$E_3 = \left(r_1 r_2 e^{-ik'l}\right)^2 t_2 e^{-ik'(l-a)} E_i$$

$$E_4 = \left(r_1 r_2 e^{-ik'l}\right)^2 t_2 e^{-ik'(l-a)} E_i$$

where t_2 is the amplitude transmission coefficient and r_1 and r_2 are the amplitude reflection coefficient of the two mirrors. We can obtain:

$$E_{out} = \frac{t_2 e^{-ik'(l-a)}}{1 - r_1 r_2 e^{-i2k'l}} E_i \tag{2.49}$$

where **k'** is the complex propagation constant which equals **k+Δk+i(γ-α)/2**. **γ** is the gain coefficient and **α** represents the loss within the cavity. If we ignore the correction factor **Δk**, then the output wave becomes:

$$E_{out} = \frac{t_2 e^{-ik(l-a)} e^{(\gamma-\alpha)(l-a)/2}}{1 - r_1 r_2 e^{-i2kl} e^{(\gamma-\alpha)l}} E_i \tag{2.50}$$

If the denominator of equation 2.38 becomes zero, which can happen when

$$r_1 r_2 e^{-i2kl} e^{(\gamma-\alpha)l} = 1 \tag{2.51}$$

This corresponds to a finite output wave **E_out** with an infinitesimal source wave **E_i** (i.e. oscillation). Physically, it means the wave making a complete round trip inside the cavity and returns to the starting place with the same amplitude and phase. Separating the oscillation condition into amplitude and phase requirements gives:

$$r_1 r_2 e^{(\gamma-\alpha)l} = 1 \tag{2.52}$$

for the threshold gain constant **γ_t** and

$$2kl = 2m\pi, m = 1,2,3,\dots \tag{2.53}$$

for the phase condition. The amplitude condition can be re-written as:

$$\gamma_t = \alpha - \frac{1}{l} \ln r_1 r_2 \tag{2.54}$$

where constant **γ_t** is known as the threshold gain coefficient. Comparing with equation 2.46, the threshold condition can be written in the form of threshold population inversion [34]:

$$N_t \equiv N_2 - N_1 = \frac{8\pi n^2 v^2 t_{spon}}{g(v)c^2} \left(\alpha - \frac{1}{l} \ln r_1 r_2 \right) \tag{2.55}$$

39

2.5.3 Pumping Processes

In the stimulated emission process shown in Fig. 2.23(c), the atoms need to be on the higher energy level. It can be most commonly performed by either optical pumping (i.e. by light emitted from a powerful lamp or laser source), or electrical pumping (i.e. by a current flowing through conductive media, such as ionized gas or semiconductors).

In optical pumping, emitted light from the source is absorbed by the active medium, so that atoms are pumped into the higher energy levels. This method is particularly suitable for solid-state or liquid lasers. In the case of light with narrow spectrum from a suitable laser source, the laser wavelength needs to fall within the one of the medium's absorption band.

Electrical pumping is for the most common way to excite semiconductor lasers. Electrical pumping for semiconductor lasers proves to be quite convenient, since a sufficiently large current density can be made to flow through a semiconductor laser in the form of p-n or p-i-n diodes [35].

2.5.4 Semiconductor lasers
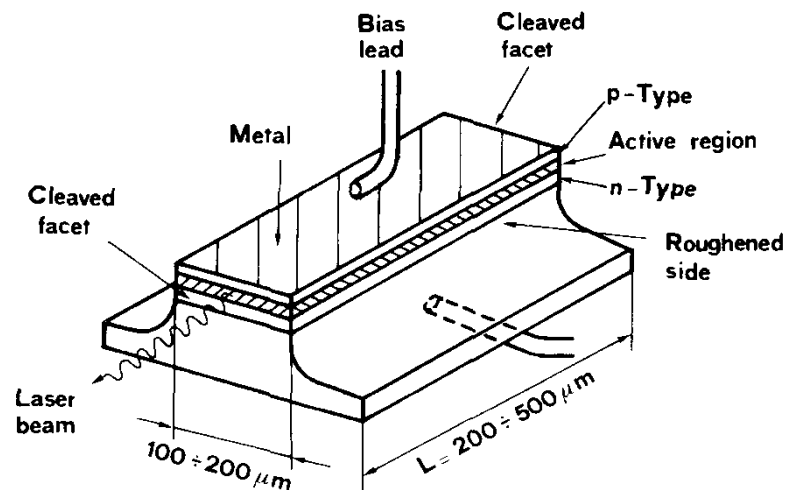
Fig. 2.25 Typical broad area double heterostructure laser [36].

Due to the large variety of direct applications, semiconductor lasers have become one of the most important kinds of lasers in use today. The simplest and the most common structures are double hetero-structure (DH) lasers, which are based on p-i-n diodes. Fig. 2.25 illustrates a typical broad area double hetero-structure laser diode. The active region is sandwiched between the *n* and *p* type cladding layers. The cleaved facets on both sides act as the reflective mirrors. It is required that the active region has a higher refractive index than the cladding layers ($n_1 > n_2$), so that light can be confined vertically (Fig. 2.26b). The laser diode is pumped electrically through the injection of carriers from both the n and p sides. Type I band alignment is favoured between the active region and the claddings to help the injection of both electrons and holes. Moreover, if proper barriers in the conduction band and valence bands can be formed, it can prevent the direct flow of carriers to the other side of the structure, making the injection more efficient (Fig. 2.26c).
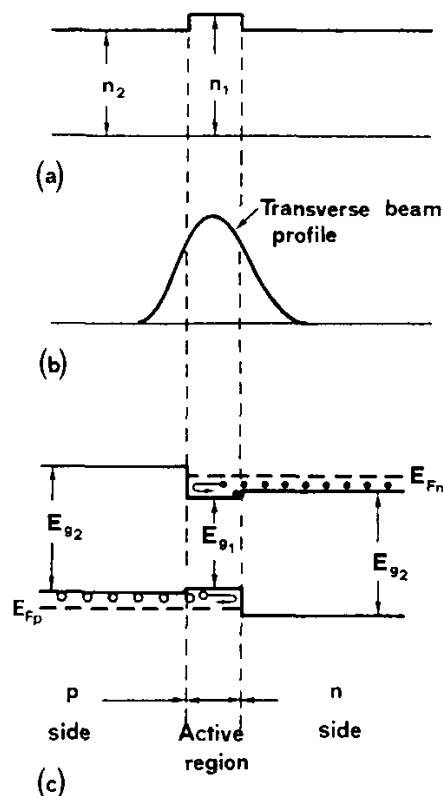
Fig. 2.26 (a) refractive index profile, (b) transverse beam profile and (c) band structure of a double hetero-structure laser [36]**.**

41

2.5.4.1 Threshold current density

In previous section, we have calculated the threshold gain (equation 2.46) and threshold population inversion (equation 2.55). As shown in Fig. 2.26(b), only part of the optical mode in the vertical direction overlaps with the gain medium. So the threshold gain in semiconductor lasers can be modified as:

$$\gamma_m \Gamma = \gamma_t = \alpha - \frac{1}{l} ln r_1 r_2 \tag{2.56}$$

where γ_m is the material gain of the gain medium and $\boldsymbol{\Gamma}$ represents the optical mode overlap with the gain medium. For electrical pumping, the threshold current density ($\boldsymbol{J_{th}}$) can also be derived as:

$$J_{th} = \frac{ed}{\eta_i \tau_r} N_t = \frac{ed}{\eta_i \tau_r} \cdot \frac{8\pi n^2 t_{spon}}{g(v)\lambda^2} \left(\alpha - \frac{1}{l} ln r_1 r_2 \right) \tag{2.57}$$

where $\boldsymbol{e}$ is the electron charge, $\boldsymbol{d}$ is the thickness of the active region, $\boldsymbol{\tau_r}$ is the radiative recombination lifetime and $\boldsymbol{\eta_i}$ is the internal quantum efficiency, defined in equation 2.28. Note that the loss inside the cavity $\boldsymbol{\alpha}$ is usually dependent on the thickness of the active region $\boldsymbol{d}$. When the value of $\boldsymbol{d}$ decreases, resulting in larger part of the optical mode leaking into the cladding layers, which have a higher absorption coefficient because of the high $\boldsymbol{n}$ or $\boldsymbol{p}$ doping concentration. So an optimal thickness $\boldsymbol{d}$ is required to have lower threshold lasing [36].

2.5.4.2 Gain from quantum nanostructures

The densities of states in different quantum nanostructures have been discussed in previous sections (Fig. 2.18). Consequently, QWs, quantum wires and QDs would have unique gain envelopes. One representative example of different types of $Ga_{0.47}In_{0.53}As/InP$ nanostructures with the same carrier injection is shown in Fig. 1.2. The peak gain increases from bulk material to QWs, from QWs to quantum wires, and from quantum wires to QDs. On the other

hand, the linewidth of the gain spectrum decreases when the material changes from bulk to 2D (QWs), 1D (quantum wires) and 0D (QDs). In this picture, the advantages of using QDs to achieve higher gain in a narrower spectral width can already be observed [36].

2.5.4.3 Characteristic temperature

As the ambient temperature increases, the output power from a laser diode gradually decreases because of the increase in threshold current I_{th} or the decrease in the external differential quantum efficiency. Examples of these temperature dependences are shown in Fig. 2.28. The characteristic temperature, T_0, is often used as a measure for temperature dependence of lasing characteristics and is empirically expressed for I_{th} as:

$$I_{th} = I_{th0}exp(\Delta T/T_0) \tag{2.58}$$

where I_{th0} and I_{th} are the threshold current before and after temperature change ΔT. A large T_0 indicates a small change of I_{th} with temperature. T_0 is not a physical parameter but is associated with some physical mechanisms determining the temperature dependence of lasing characteristics. The main factors determining I_{th} are the following: overflow of injected carriers, Auger recombination and inter-valence band absorption. The free carrier absorption also increases according to the I_{th} increase.
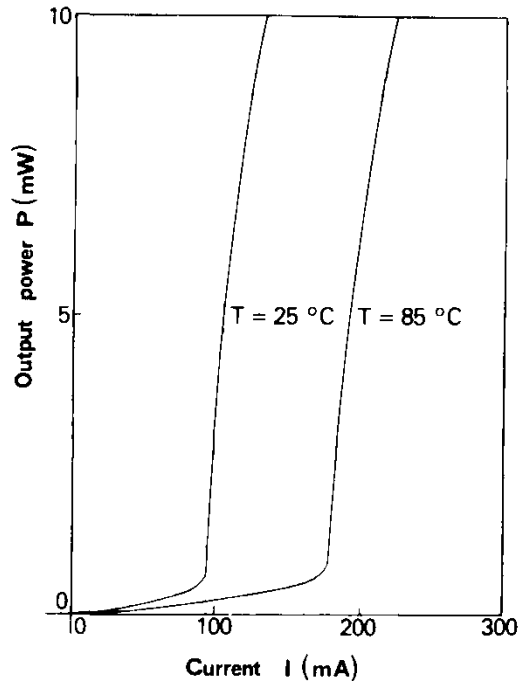
Fig. 2.27 Schematic plot of output power versus input current of a DH laser diode at different temperatures [36]**.**

2.5.4.4 Differential quantum efficiency

The differential quantum efficiency, η_d, is a measure of the overall efficiency of the device. Practically, η_d can be measured from the gradient of the graph of optical power against drive current, since [37]:

$$\eta_d = \frac{e}{hv}\frac{dP}{dI} \tag{2.59}$$

where *e* is the charge on an electron, *hv* is the photon energy, and *dP/dI* is the gradient of the power–drive current curve after threshold where stimulated emission is occurring. *hv* is generally taken to be the band gap energy, and *hv/e* therefore can be taken to equal to the value of band gap energy in eV.

3. Literature review

3.1 Introduction

In this chapter, the development of different types of laser sources in the mid-infrared range will be presented. The advantages and disadvantages of each will be discussed. The performances of different lasers will be compared in terms of the highest working temperature (T_{max}), the threshold current density (J_{th}), the characteristic temperature (T_0) and the output power.

3.2 Bulk semiconductor lasers

InGaAsSb is the first bulk gain material used to achieve lasing in the mid-infrared range in a semiconductor DH laser structure. It was first reported by Caneau et al. in 1985. The laser structure contains InGaAsSb gain layer sandwiched between AlGaAsSb cladding layers on both sides. The structure was grown on GaSb substrates using LPE [38]. The laser emitting at around 2.2 μm at RT required a J_{th} of 6.9 kA/cm^2 with pulsed excitation. InGaAsSb alloys were grown lattice-matched on GaSb substrates by controlling its composition, resulting in band gap energy between 0.29 and 0.73 eV, which covered the wavelength range between 1.7 μm and 4.3 μm. However, due to the large miscibility gap, the longest emission wavelength of LPE grown InGaAsSb is limited to 2.5 μm [8]. Baranov et al. achieved the highest working temperature of 120 °C for the InGaAsSb laser emitting at 2.1 μm [39], and the longest wavelength laser of 2.5 μm at RT was also reported [40]. To further extend the wavelength MOCVD and MBE technologies were adopted to grow the InGaAsSb DH lasers, which do not have the miscibility gap limitation. 3 μm lasers grown by MBE were reported working up to 255 K at pulsed excitation and 170 K at continuous wave (CW) operation, with CW output power of 45 mW at 100K and pulsed J_{th} as low as 9 A/cm^2 at 40 K [41]. The RT CW operation of the InGaAsSb/AlGaAsSb/GaSb lasers using MBE technology was achieved by

Choi et al. in 1991 [42]. The device emitted at around 2.2 μm with an output power of 4.6 mW (at 20 °C). The J_{th} at RT was reduced to 940 A/cm^2 at pulsed excitation.

Extension of the emission wavelengths beyond 3μm is difficult for the GaInAsSb/AlGaAsSb system because the valence band offset and refractive index difference between the active layer and cladding layers becomes smaller. InAsSb(P) as the gain material has been investigated to achieve longer wavelength lasing. The LPE grown InAsSb/InAsSbP/InAs laser structure on InAs substrates emitted up to 3.9 μm at 180 K at pulsed mode [43]. In CW operation, these lasers can work up to 82 K, with an output power of about 10 mW [44]. MOCVD growth improved the T_{max} up to 220 K in pulsed mode, with an output power of 660 mW and a J_{th} of 34 A/cm^2 at 78 K, and the devices emitted at around 3.2 μm [45]. Recently, an optimized 5 layer structure grown by LPE emitting at around 3.5 μm also achieved T_{max} of 210 K [46].

To make even longer wavelength lasers, InAsSb/AlAsSb DH structures were grown on GaSb substrates by MBE. The devices emitted at around 4 μm, and worked up to 80 K and 155 K in CW operation and pulsed excitation respectively [47]. Ashley et al. reported 5.1 μm stimulated emission from InAsSb/InSb DH laser structures grown by MBE. At pulsed excitation, the J_{th} was 1.48 kA/cm^2 at 77 K and the lasers can work up to 90 K with a J_{th} of 2.68 kA/cm^2 [48].

Up to date, RT CW operation of bulk semiconductor lasers above 3 μm has not yet been achieved. By comparing the aforementioned reports, we can observe that in general, to achieve longer wavelength lasing, higher J_{th} is required and the devices typically have lower T_{max}. In addition, it needs to be stressed that, none of these devices has a T_0 higher than 45 K even at low temperatures. The low values of T_{max} and T_0 for longer wavelength lasers are related to the strong Auger processes in the InAs-rich materials [49]. In these compounds, the resonance between the band gap and the spin orbit splitting band is very likely to happen, which dramatically enhances the CHSH Auger process. The consequence is that at T > 77K

the threshold current density is dominated by the CHSH Auger mechanism which prohibits RT laser operation [50].

3.3 Quantum well lasers

To further improve the performance of mid-infrared lasers, bulk gain materials were replaced by QWs in the laser structure. Compared with bulk DH lasers, QW lasers have lower threshold current density; the temperature performance, differential gain and modulation of the mid-infrared lasers can also be improved [8]. In QW lasers, the QW active region is embedded between spacer layers. The QWs have lower band gap energy but higher refractive index as compared with the spacer layers. So the carriers are confined in the QWs while the emission is confined inside the waveguide layers to prevent it penetrating into the cladding layers.
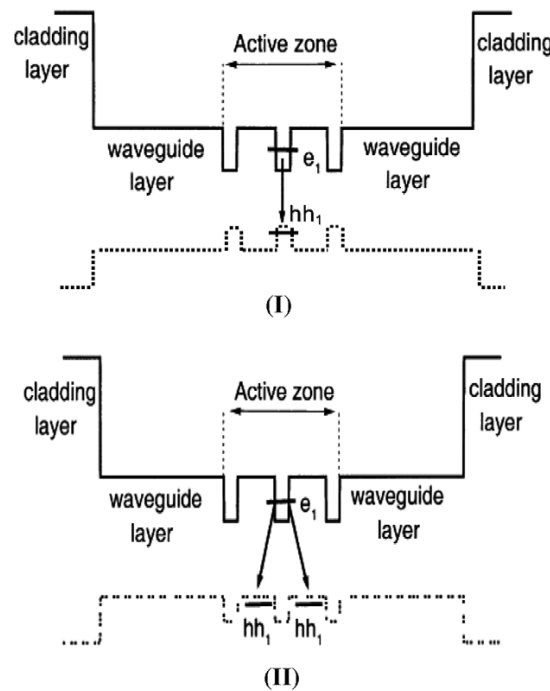
Fig. 3.1 Band alignment and fundamental electron–hole transition e1–hh1 of (i) type I and (ii) type II QW structures [8].

3.3.1 Type I QW lasers

Fig. 3.1(i) illustrates the typical type I QW laser structure. The InGaAsSb/AlGaAsSb QW is among the most investigated type I structure for the mid-infrared range. To date, for wavelengths below 2.5 μm, RT CW operation of InGaAsSb/AlGaAsSb type I QW lasers with output power exceeding 1.0 W have been achieved. The lowest reported J_{th} per QW layer is 50 A/cm^2 for 2.2 μm lasers [51], 90 A/cm^2 for 2.3 μm lasers [52] and 125 A/cm^2 for 2.5 μm lasers [53] respectively. These laser structures were all grown by MBE on GaSb substrates. However, one disadvantage of the InGaAsSb/AlGaAsSb QW is the shallow energy step in the valence band between InGaAsSb and AlGaAsSb, i.e., there is only a small hole confinement in the QW, which can result in higher J_{th} and lower quantum efficiency, especially at RT. Growing the InGaAsSb with less As can add more compressive strain in the QW, which levels up the energy bands of InGaAsSb (Fig. 3.2a), resulting in stronger hole confinement. QW lasers with 1.5% strain demonstrated almost two fold reduction in J_{th} compared with the same structure with 1% strain in the QWs [54].
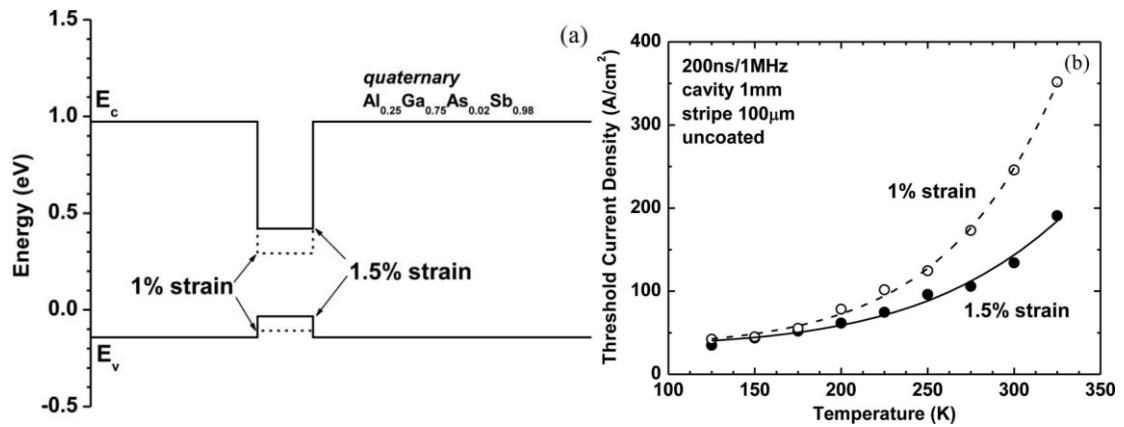
Fig. 3.2 (a) Calculated band diagram of the 1% and 1.5% compressively strained QWs, (b) Temperature dependences of the threshold current density for lasers with 1% and 1.5% compressively strained QWs [54]**.**

Although adding compressive strain can help improve laser performance, it is still difficult to have RT QW lasers at longer wavelengths from the InGaAsSb/AlGaAsSb material system. By replacing the AlGaAsSb spacer layer with quinternary AlInGaAsSb material, there can be a much deeper energy offset in the valence band of the QWs. As sketched in Fig. 3.3a, an extra

100 meV can be added in the hole confinement energy for the 3.1 μm lasers, which leads to about two-fold reduction of J_{th} (Fig. 3.3b), even though the quinternary barrier results in lower electron confinement compared with the quaternary material [55]. Vizbaras et al. reported a record-high 64 °C CW operation of the InGaAsSb/AlInGaAsSb type I QW lasers grown on GaSb substrates emitting at around 3 μm [56]. The QWs have a relatively strong hole confinement of 71 meV. At RT, the lasers exhibited a low J_{th} of 198 A/cm^2 (66 A/cm^2 per QW layer). Output powers of 190, 165 and 50 mW were reported from this type of QW laser emitting at 3.1, 3.2 and 3.3 μm respectively at RT (CW operation), with the J_{th} between 350 and 545 A/cm^2 (117 and 182 A/cm^2 per QW layer) [9]. In their work the hole confinement energy was improved by increasing the In composition in the quinternary barriers. By optimizing the waveguide geometry and material composition, Hosoda et al. demonstrated lasing at 3.44 μm from this kind of QW laser, which is the longest wavelength obtained at RT in CW operation [57]. The devices can generate a 29 mW output power, with a J_{th} of about 650 A/cm^2 (217 A/cm^2 per QW layer).
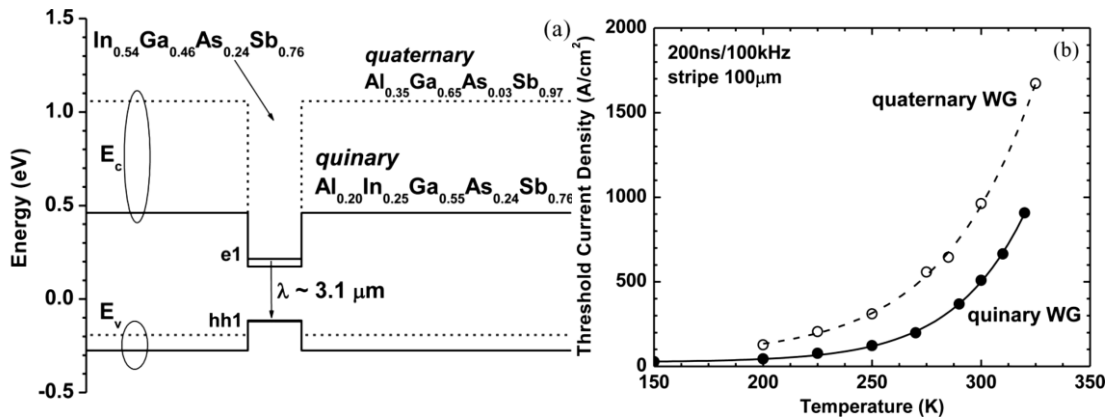
Fig. 3.3 (a) Calculated band alignment for 3.1-μm emitting lasers. Solid line shows the band edges for QW materials and for quinternary AlInGaAsSb barriers. The dashed line shows the band edge position for quaternary AlGaAsSb alloys. (b) Temperature dependences of the threshold current density for 3.1 μm emitting lasers with AlGaAsSb quaternary and AlGaInAsSb quinternary barriers [55]**.**

By increasing the In content in the InGaAsSb above 0.7, as compared with 0.57 in the 3.44 μm laser [57], the QW can emit above 3.5 μm. In order to maintain sufficient hole

confinement (40–50 meV), the In content in the AlGaInAsSb barrier also needs to be increased from 0.32 to 0.5 [58]. The number of QWs in the laser structure was also increased to five, so as to produce high enough modal gain. The laser structure is sketched in Fig. 3.4(a). The lasers can work at RT, emitting up to 3.73 μm, though only with pulsed excitation. The J_{th} was 676 A/cm^2 (135 A/cm^2 per QW layer) (Fig. 3.4b) [59].
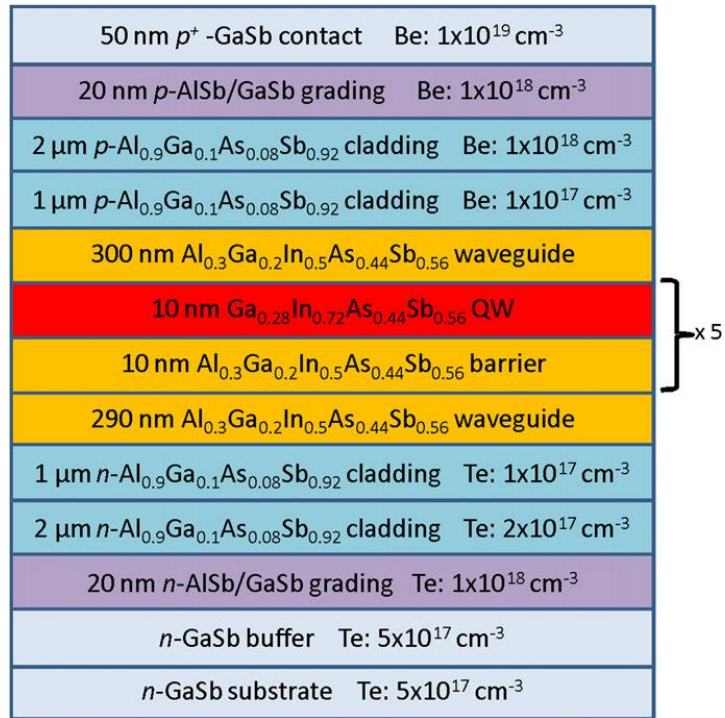
(a)
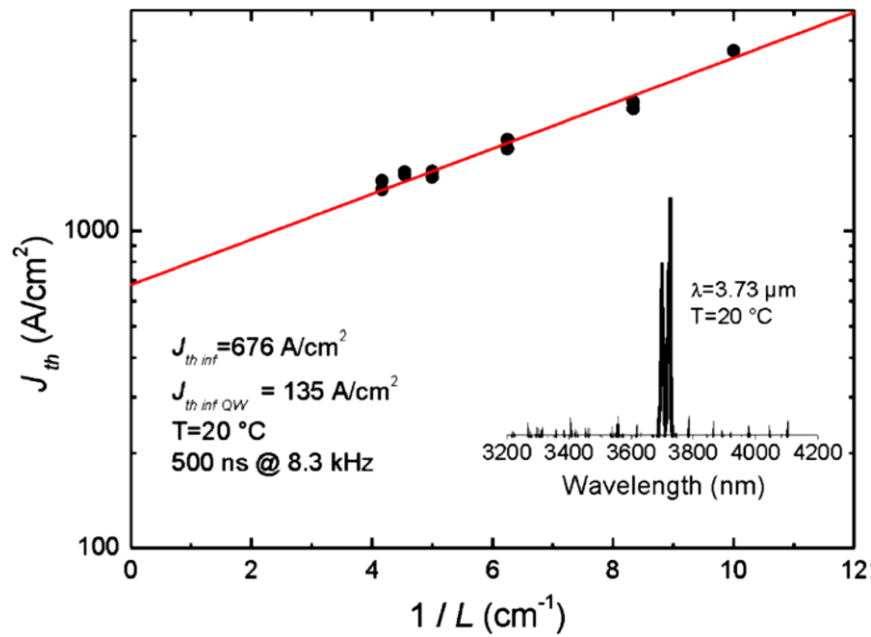
(b)

Fig. 3.4 (a) Schematic epitaxial layer structure of the investigated devices, emitting at 3.73 µm. (b) Pulsed J_{th} as a function of inverse cavity at 20 °C. The inset shows a measured emission spectrum centred around 3.73 µm for a 2 mm long laser driven at 2.5 I_{th}, at 20 °C [59].

In the meantime, GaSb-based type I QW single mode lasers in distributed feedback (DFB) structures have been made, which is highly desired in trace-gas sensing systems. 2.65 μm DFB lasers with InGaAsSb/AlInGaAsSb QWs were demonstrated. The devices worked at RT CW operation, with an output power of 25 mW and 150 mA threshold current [60]. RT CW operation of 3.06 μm and 3.4 μm single mode lasers in similar structures were also reported [61], [62]. The 3.06 μm laser can have an output power of 6 mW, with a threshold current of 50 mA.

Lasing between 3 and 4 μm from type I InAsSb QWs grown on InAs substrates has also been developed. The 3.4 μm laser contains 10 InAsSb/InAlAsSb type I QWs in the active region and AlAsSb cladding layers on both sides, grown lattice-matched to the InAs substrates [63]. The devices can work up to 220 K in pulsed mode. The output power was 215 mW at 80 K in CW operation, but decreased to 35 mW at 150 K. Allerman et al. grew the laser structure with strained InAsSb/InAs QWs as the active region, and lattice-matched AlAsSb as the cladding layers on InAs substrates by MOVPE [64]. The p-GaAsSb/n-InAs semi-metal structures were included in the devices as a source for electron injection into the active region. These lasers can perform up to 210 K in pulsed mode.

To make use of the more mature and more cost-effective GaAs and InP based technologies, type I QWs in the mid infrared have been integrated on these substrate platforms. Mid-infrared lasers on GaAs substrates were reported using two GaInSb/AlGaInSb type I QWs as the active region [65]. Lasing was observed up to 219 K at around 3.3 μm. By optimizing the strain in the QWs, the J_{th} can be reduced to 34 A/cm^2 per QW layer at 100 K. Recently, strain compensated InAs/InGaAs type I QWs were integrated on InP substrates using metamorphic InAlAs buffer layers [66]. The lasers in a separate confinement heterostructure can work up to 110 K in CW operation and 170 K in pulsed mode, emitting around 2.7 μm. Further improvements in performance can be expected by increasing the hole confinement in the QWs.

To summarize, there has been significant progress in the type I InGaAsSb/Al(In)GaAsSb QW lasers on GaSb in the mid-infrared. RT CW operation with high output powers has been achieved for the wavelengths between 2 and 3.4 µm. Strain in the QWs and quinternary barriers have been utilized to lower the J_{th} and increase output power. Lasing above 3.4 µm has been realized at RT in pulsed mode using quinternary barriers. Tunable single mode DFB lasers for gas sensing applications have also been demonstrated at RT in CW operation. At near or above room temperature, the GaSb based type I QW lasers can achieve a T_0 higher than 100 K for wavelengths below 2.6 µm [67]. At 3.0 µm, 3.4 µm and 3.7 µm, the highest reported T_0 decreased to 43 K, 17 K and 16 K respectively. The reduction of T_0 can be largely attributed to the increased free carrier absorption and Auger recombination at longer wavelengths [55]. Besides the GaSb-based material systems, different structures of type I QW lasers in the mid-infrared range have also been realized on InAs, GaAs and InP substrates. These devices exhibit reasonable values of J_{th} and T_0, though to date none of them can work at RT in CW operation.

3.3.2 Type II QW lasers

(a)   (b)
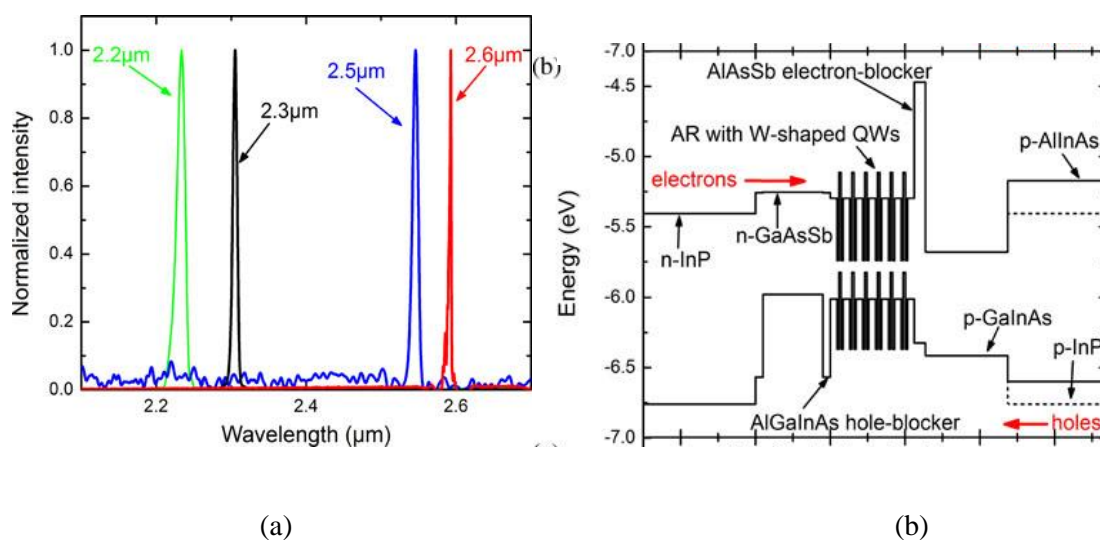
Fig. 3.5 (a) Lasing spectra of type-II InP-based lasers, measured in pulsed mode at RT. (b) band structure of the type-II laser structure [68]**.**

53

By using type II QWs as the gain medium in the laser structure (Fig. 3.1ii), the Auger recombination rate can be reduced by removing the resonance between the band gap energy E_g and the spin orbit split-off energy Δ [69]. Moreover, by choosing the appropriate QW and barrier material combinations, large band offsets can be formed on both conduction band and valence band, eliminating the problem of carrier leakage as in some of the type I QWs [55]. One disadvantage of type II band alignment is the separation of electron and hole wave functions, which can lead to the reduction of radiative recombination rate in the type II QWs. But under external excitation, this problem can be compensated by the Coulomb interaction between localized electrons and holes, which can bend the energy bands and increase the wave function overlap [67]. In addition, in type II QW laser structures, more QWs than in the type I lasers are usually placed in order to reach high enough gain.

The group of M. Amann has made significant progresses on the type II QW lasers grown on InP substrates. GaInAs/GaAsSb QWs have been used as the gain medium. The holes are very well confined in the GaAsSb layer due to their high effective mass, while the electrons are lightly confined in GaInAs. The laser structures usually also contain thin AlAsSb and AlGaInAs layers on each side of the active region to block the carriers from directly flowing to the other side of the devices. Either InP or AlInAs is used as the top p-cladding layer (Fig. 3.5b). The active region is composed of six QWs. At RT in pulsed mode, the lasing wavelength has been extended from 2.2 μm to 2.6 μm by increasing the well thickness (Fig. 3.5a). The J_{th} of these lasers lies between 1.3 and 1.9 kA/cm^2 (220-320 A/cm^2 per layer) at RT. For the 2.3 μm laser, the T_0 is 51 K in the temperature range below 285 K, but decreases to 27 K at RT, and further to 16 K when temperature is above 300 K. The decrease of T_0 can indicate the onset of an extra loss mechanism, the origin of which is still not clear. Nevertheless, the 2.3 μm laser can work in CW mode up to 0 °C [70].

Wilk et al. developed type II InAsSb/InAs QW lasers on InAs substrates emitting at 3.5 μm [71]. The active region contains ten InAsSb QWs with 20 nm thick InAs spacers in between.

54

Lattice-matched AlAsSb was used for both p- and n-cladding layers. These lasers worked up to 220 K in pulsed mode, and up to 130 K in CW operation. At 90 K, a J_{th} of 20 A/cm^2 per layer was obtained in pulsed mode, which is comparable to the J_{th} of mid-infrared type I QW lasers. In the 100 K to 125 K domain, the T_0 was estimated to be around 40 K in CW operation. However, the waveguide loss of these lasers is still relatively high (~30 cm^{-1}). By optimizing the laser structure, it is possible that the loss can be reduced and the laser performance could be enhanced.

3.4 Superlattice lasers

If the barrier thickness between adjacent QWs is reduced close to the well thickness, confinement can appear both on the valence band and conduction band. Instead of the discreet states in separated QWs, in these structures minibands will be formed due to the strong tunnelling of carriers through the thin barriers/wells. Such structures are called superlattices (SLs). GaInAs/InAs superlattices on GaSb substrates were first used by Chow et al. as the gain medium in the laser structures, which emitted between 3.28 μm and 3.9 μm [72]. The T_{max} decreased from 170 K for shorter wavelength lasers to 84 K for longer wavelength lasers. The emission wavelength of this kind of laser was then extended to the range between 2.8 μm and 4.3 μm [73] and the T_{max} increased to 255 K for the 3.2 μm laser. With an optimized active region, T_0 was improved from 30 K to 86 K for the temperature range below 200 K although at higher temperatures, the value dropped to 33 K. Zhang et al. made use of InAs/InAsSb SLs on InAs substrates, which have a type II band alignment, for lasers emitting at around 3.4 μm [74]. The devices can work CW up to 95 K, with a J_{th} of 56 A/cm^2 and a T_0 of 32 K. The InAs/InAsSb SLs exhibited an electron-hole wave function overlap of 89%, which is significantly larger than in the type II InAsSb/InAs QWs (42%). InAsSb/InAsP SL lasers were then developed by MOCVD growth, which have a type I band alignment [75]. The

large light-heavy hole splitting (70 meV) in the superlattices helped to suppress Auger recombination. The lasers displayed emission at around 3.9 μm up to 240 K, with a T_0 of 33 K.

Despite the good results reported above for SL lasers, it is important to note that the structure is non-optimal since the electrons have a quasi-three dimensional (3D) energy dispersion, like in a bulk material. QW lasers have significantly higher performance than bulk DH lasers because the more concentrated 2D density of states yields higher gain per injected carrier at threshold [76]. The SL structures fundamentally lack this advantage.

3.5 "W" lasers

A "W" structure is typically composed of a "hole" QW sandwiched between two "electron" QWs, resulting in a "W" shape in band alignment. The small effective mass of electrons and the thin "hole" QW means the electron wave function can largely spread across the whole "W" region. Using "W" structures as the active region in lasers can combine the advantages of both type I QWs (confinement for both electrons and holes, and large wave function overlap), with the advantage of type II QWs (reduced Auger recombination rate) [55]. Type II InAs/GaInSb/InAs "W" structures on GaSb substrates were proposed for the mid-infrared range (Fig. 3.6), which exhibited an electron-hole wave function overlap of 57% [69]. This structure was later optimized by adding AlGaAsSb separate confinement heterostructure (SCH) layers, which can maximize the optical confinement factor in the active region and minimize free carrier absorption losses in doped cladding layers. The laser active region was composed of 5 "W" structures, which can work up to 195 K in CW mode, emitting at around 3.25 μm [77]. The J_{th} was 13 A/cm^2 per "W" layer at 78 K, and increased to 280 A/cm^2 per "W" layer at 195 K. By increasing the number of "W" structures to 10, the lasers can work up to 310 K in pulsed excitation. Canedy et al. extended the emission wavelength of similar "W" laser structure emitting up to 3.7 μm. They used InAs/AlSb superlattices for the n-cladding, and InAs/GaInSb superlattices for the n-SCH and transitional layers between the regions to

smooth out abrupt discontinuities in the conduction band profile. The T_{max} reached 218 K in CW mode and 317 K in pulsed mode, the J_{th} was effectively reduced to 6.2 A/cm^2 per "W" layer at 78 K [78].
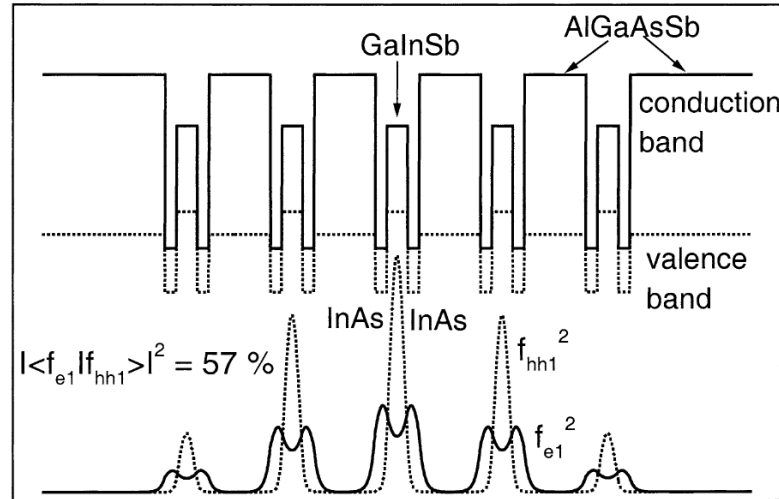
Fig. 3.6 Schematic band diagram of the InAs (15 Å)/GaInSb (27 Å)/InAs (15 Å)/AlGaAsSb (80 Å) "W" laser structure. The lower part shows the fundamental electron (e1) and heavy-hole (hh1) wave functions [67]**.**

Recently, InAsN/Ga(As)Sb/InAsN "W" lasers were also proposed on InAs and InP substrates [79], [80]. The theoretical calculations proved that dilute nitride "W" structures can achieve high modal gain and large T_0. Optically pumped GaAsSb/InAsSb/GaAsSb "M" lasers, which are in an inverse "W" shape, have been demonstrated up to RT emitting around 2.4 μm, with a T_0 of 47 K for temperatures above 250 K [81].

3.6 Quantum dot lasers

As discussed in the previous chapter, due to its delta-like DOS, QDs are promising gain media for semiconductor lasers to obtain extremely low J_{th}, high differential gain and excellent temperature stability [2]. In the last few decades, there has been great progress in QD lasers in the visible and near-infrared spectral range. For instance, at around the 1.3 μm

telecommunication wavelength, the type I InAs/InGaAs QD lasers on GaAs substrates grown by MBE demonstrated a J_{th} as low as 4.3 A/cm^2 per layer at RT [82]. Although, theoretically it was suggested that the J_{th} of QD lasers can be temperature insensitive [83], in reality there is a trade-off between low J_{th} and temperature stability for undoped QDs (i.e. QD lasers with low J_{th} typically can only have relatively small value of T_0) [84]. Although the radiative current in QDs can be approximately constant over a wide range of temperatures, non-radiative Auger recombination hampers the chance for temperature stable J_{th}. Especially for longer wavelength (1.3 – 1.5 µm) InAs QD lasers, Auger process can consume a large part of the injected carriers at RT, while for shorter wavelength lasers, thermal leakage of carriers out of the QDs is believed to be the major factor for small values of T_0 at RT [85]. By using p-doped InAs/InGaAs QDs, Fathpour et al. reported temperature invariant ($T_0 \rightarrow \infty$) lasers for above RT [86]. In the p-doped QDs, Auger recombination still exists, but the increase of Auger rate with increasing temperature is compensated by a decrease in radiative current around room temperature due to the increased potential barrier height for the electrons, making the lasers temperature stable over a limited temperature range, though at the expense of higher J_{th} [84].

It is difficult to extend the wavelength of InAs/(In)GaAs QDs beyond 1.6 µm. Other QD material systems have been explored. A single layer of InAsSb QDs was grown in an InGaAs QW on InP substrate by MOCVD. InGaAsP and InP cladding layers were included in the laser structure [87]. These lasers worked CW at RT, emitting at 2.03 µm with a J_{th} of 730 A/cm^2. The emission wavelength of InAs quantum dashes (elongated QDs) has recently been extended to around 2 µm. RT lasing of the dash-in-a-well structure grown by MBE on InP substrates has also been reported [88].
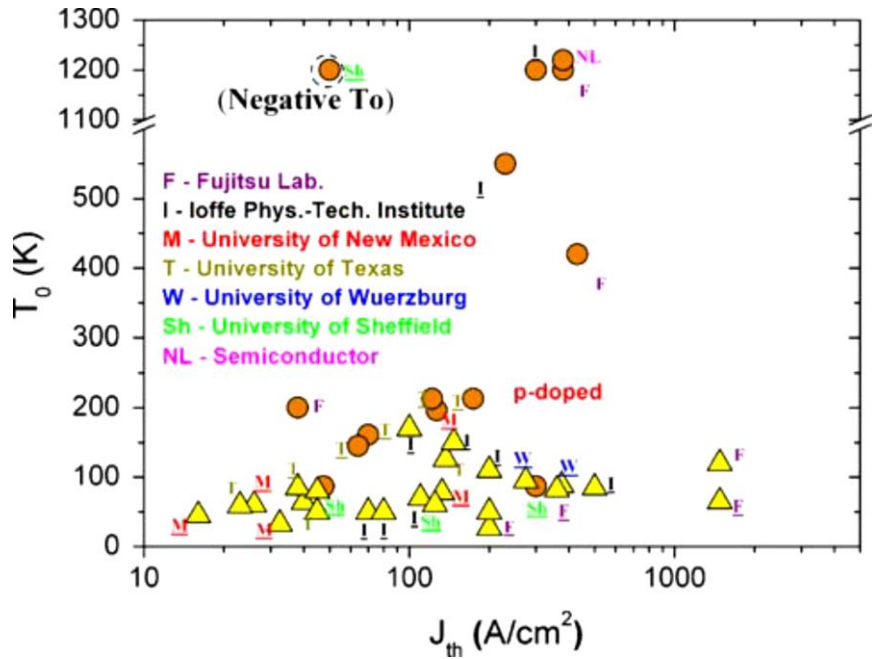
Fig. 3.7 Dependence of the T_0 on J_{th} at room temperature of 1.3 μm QD lasers based on data available from literature. The underlined symbols are DWELL structures [84]**.**

3.6.1 InSb/InAs quantum dots

In the spectral range between 3 and 5 μm, In(As)Sb QDs in an InAs matrix are the most promising candidate as the gain medium for QD lasers. Bright photo-luminescence (PL) and electro-luminescence (EL) of the In(As)Sb/InAs QDs have been demonstrated at RT [89], [90]. As shown in Fig. 3.8, the QD structure has broken type II band alignment (i.e. the valence band of InSb QD is higher than the conduction band of InAs matrix), and radiative recombination happens between the electrons in InAs and the holes in confined states of the InSb QD. The large lattice mismatch between InAs and InSb (~6.5%) ensures the QDs can be self-assembled.

Liquid phase epitaxy (LPE) has been utilized to grow the InSb/InAs QDs [91]. Under optimal growth conditions, the density of the InSb QDs can reach the order of 10^{10} /cm^2. The typical size of the QDs is between 2 to 6 nm in height, and 10 to 40 nm in radius [92]. However, no PL or EL signal from the LPE grown QDs has ever been reported.

59
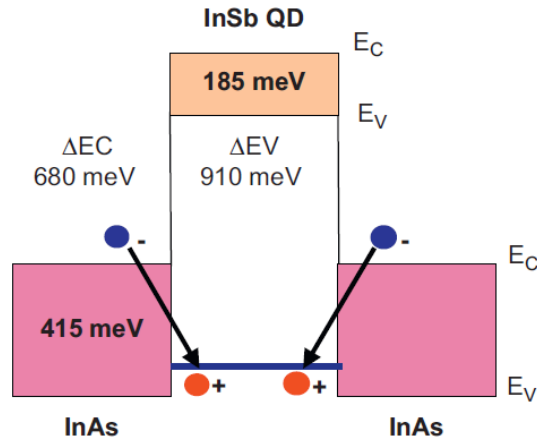
Fig. 3.8 Band alignment of InSb/InAs QDs. The holes are localized in the QDs and the electrons are in the InAs matrix [93]**.**

MBE techniques were developed to produce much higher density (~10^{12} /cm^2) InSb QDs in extremely small sizes (height: ~ 2 nm, width: ~6 nm) [94]. The cross-sectional TEM image (Fig. 3.9a) of the QD sample reveals clear insertion of InSb layers in the InAs matrix, and the plan view image (Fig. 3.9b) indicates the formation of dot-like InSb structures. These QDs are grown by exposing a flux of InSb on InAs surfaces, and the formation of QDs makes use of an As-Sb anion exchange reaction [89]. The deposition of InSb QDs using conventional epitaxy (CE) and a novel technique called migration enhanced epitaxy (MEE) have been compared [95]. During the CE growth, the shutters of In and Sb were opened simultaneously. While during the MEE growth of each QD layer, the In shutter was opened first for 4 s, followed by the Sb shutter for 20 s. It has been proved that the MEE growth technique without annealing can produce QDs of a smaller mean size and better size uniformity. To grow the InAs spacer layer between QD layers at a low temperature can also significantly enhance the emission efficiency of the QDs, suggesting that low temperatures are required to maintain good optical properties of the QDs. Both (Sb$_2$, As$_2$) and (Sb$_4$, As$_4$) have been used to grow the QDs [89] [90] [94]. At the same temperature, the growth rate by using (Sb$_2$, As$_2$) was found to be smaller than using (Sb$_4$, As$_4$). This is because there is a dynamic equilibrium between As-Sb and Sb-As exchange reactions, and the Sb-As exchange is easier under As$_2$ flux. However,

there are no observable differences in the size distribution and density of QDs caused by these two types of fluxes.
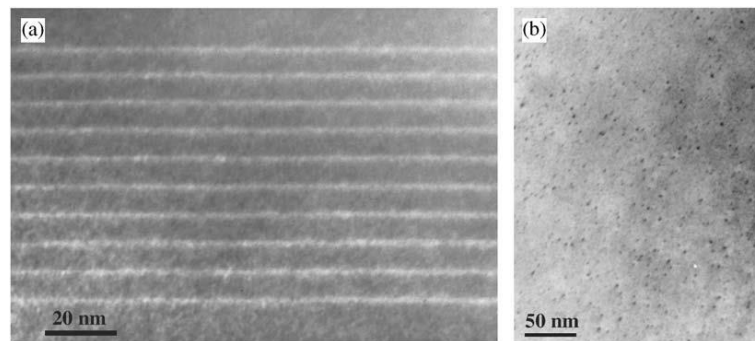
Fig. 3.9 Dark-field (002) cross-sectional (a) and plan-view (b) TEM images of ten-period InSb/InAs nanostructures (a) and single InSb insertion (b) [94]**.**

The growth of InSb QDs on InAs substrates has been experimented at different temperatures. Reflection high-energy electron diffraction (RHEED) intensity plots revealed that the As-Sb exchange is more effective at lower substrate temperatures (Fig. 3.10a) [5]. The resulting InSb/InAs QDs exhibited bright PL in the 3-5 μm spectral range. As shown in Fig. 3.10b, with thicker InSb deposition, the PL peak displays a clear red shift. The QDs' PL intensity also decreases with increasing InSb thickness, which is probably caused by smaller electron-hole wave function overlap in the lager QDs.
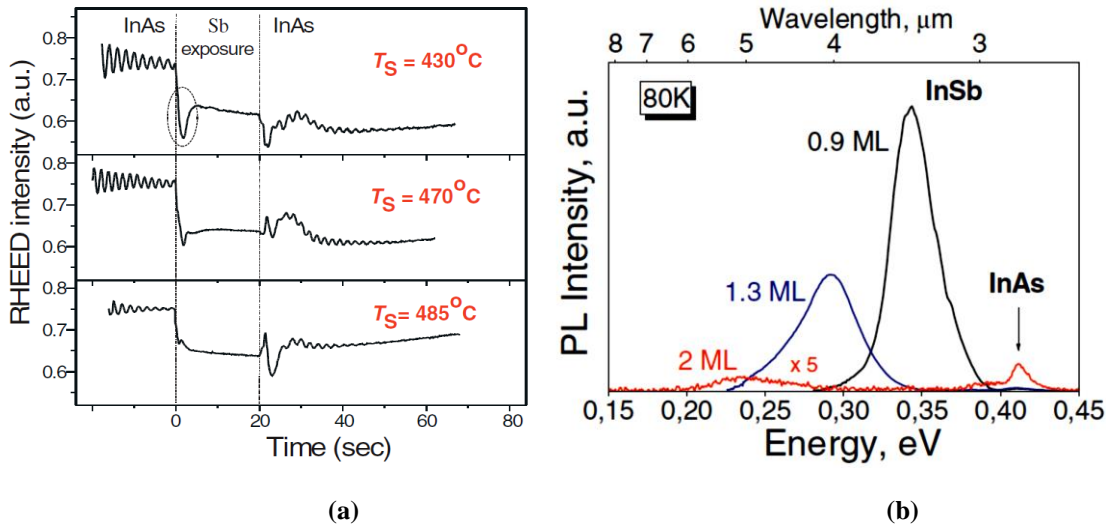
Fig. 3.10 (a) RHEED intensity variation during the growth of InSb QDs obtained at different substrate temperatures, (b) PL spectra of InSb/InAs QDs with different thickness measured at 80 K [5]**.**

The RHEED pattern also suggested that, under certain growth conditions, an extremely thin wetting layer can be formed during the QDs growth due to strong Sb segregation [96]. A weak PL peak shorter than the QD signal wavelength can be observed from some of the samples when the temperature is above 110 K, which might originate from the disordered thin wetting layer [97]. However, there is still no clear evidence from microscopic images to support the existence of the wetting layer.

Due to its extremely small sizes, it is difficult to measure the size and composition of the InSb QDs accurately. Yeap et al. used multiband *k.p* method to calculate the band structure and transition energy of the QDs with varying size and composition [98]. In their calculations, the width of the QDs was fixed to be 2.5 nm. Fig. 3.11 shows the conduction band, HH, LH and SO band alignments with varying aspect ratio (AR) by assuming the QDs are composed of pure InSb. In the type II QDs, the electrons were found to be weakly bounded by Coulomb attraction. The 3- μm QD emission involved the electron recombination with ground state HHs from QD with AR between 2.2 and 2.8. Excited hole states also existed in the QDs, but

their recombination would correspond to much shorter wavelengths. If the QDs contained a small amount of As, the emission wavelength would be longer than pure InSb QDs with the same size.
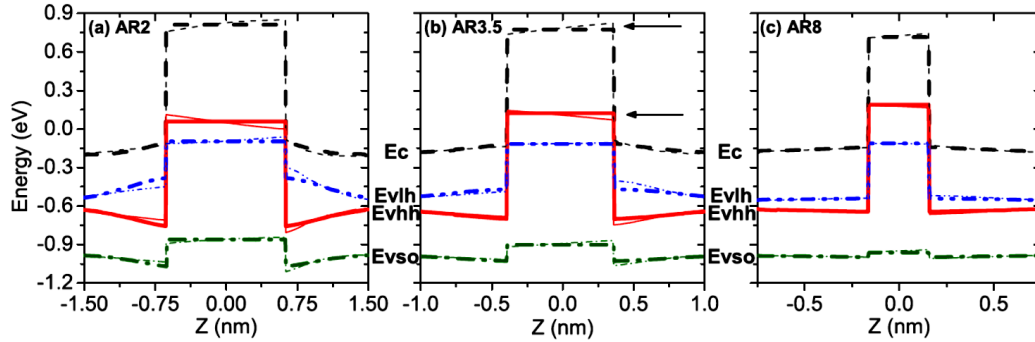
Fig. 3.11 Strain-modified band profiles along the (001) growth direction through the dot centre: dashed line—conduction band, solid line—heavy-hole band, dash-dot-dot line—light-hole band, dash-dot line—split-off valence band. (a) AR=2; (b) AR=3.5; (c) AR=8.

Despite the promising facts of high density QDs growth, strong PL and EL signals at RT, and wavelength tunability over a wide spectral range, there have been only two reports on InSb/InAs QD lasers. The first structure employed $AlAs_{0.16}Sb_{0.84}$ cladding layers lattice matched to the InAs substrate and operated up to 20 K in pulsed mode with a threshold current, J_{th}~1 kA/cm^2 (Fig. 3.12a) [93]. To avoid problems with doping the n-$AlAs_{0.16}Sb_{0.84}$, another structure used $Al_{0.8}Ga_{0.2}As_{0.15}Sb_{0.85}$ and CdMgSe as p- and n-side cladding layers, respectively, and worked up to 60 K using pulsed excitation with J_{th}~3 kA/cm^2 (Fig. 3.12b) [99]. It needs to be noticed that, for both of these two laser structures, the stimulated emission was observed around 3 μm, shorter than the typical QD PL peak wavelength, though the reason hasn't been explained yet.
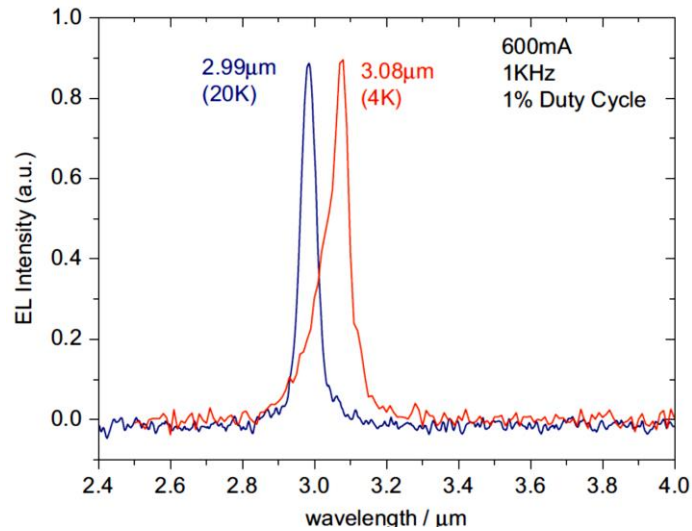
(a)
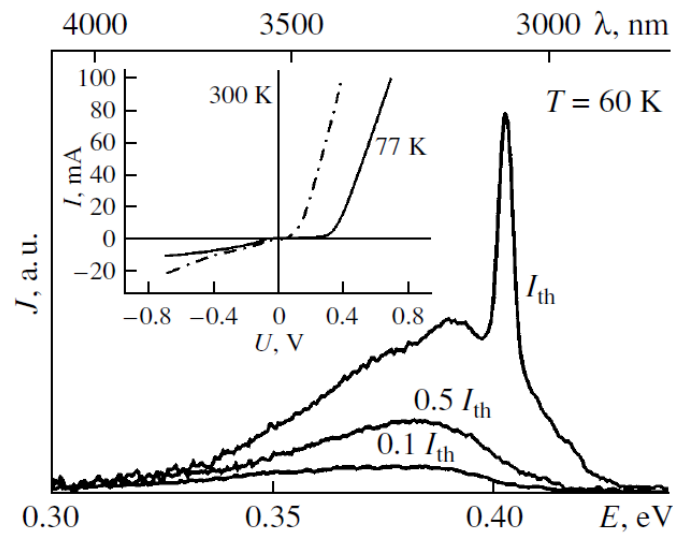
(b)

Fig. 3.12 EL spectra of QD laser structures (a) with AlAsSb cladding layers containing eight (blue curve, 20 K) and 10 (red curve, 4 K) InSb QD sheets in the active region, (b) with AlGaAsSb and CdMgSe cladding layers.

3.7 Quantum cascade lasers

The previously discussed different types of lasers (bulk semiconductor lasers, QW and QD lasers, etc) are all based on inter-band carrier recombination. The quantum cascade lasers (QCLs) differ in a fundamental way from these laser structures. The stimulated emission from a QCL relies on the electronic transition between quantized sub-bands of the multi-layered structure. The light emission mechanism of QCLs only involves the transition of one type of

carrier (electrons). The working principle of a QCL is explained in Fig. 3.13. Each active region contains a number of QWs, resulting in several quantized energy levels. Under forward bias, the electrons are first injected to level 3. The transition of electrons from level 3 to the lower energy level 2 will emit photons with energy equal to the difference between levels 3 and 2. The electrons on level 2 quickly decay to the ground level (black curve), where they can tunnel through the injector region to be re-used in the next active region. The active region is designed to get small wave function overlap between levels 3 and 2, and the transition from level 2 to the ground level is much quicker than the 3→2 transition, so that population inversion can be ensured [100]. Typical QCLs contain 20-30 cascaded active regions with several hundred layers in total [101], though single active region lasing has also been reported [102].
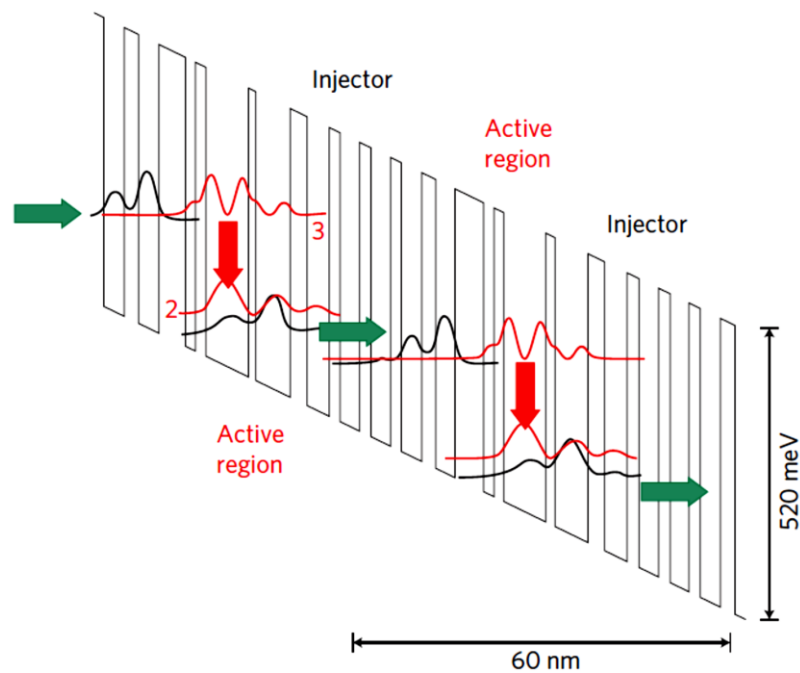
Fig. 3.13 simplified schematic of the conduction band structure for a basic QCL, where the lasing transition is between sub-bands 3 and 2 [103]**.**

The first QCL was reported in 1994, emitting at around 4.3 µm [100]. Since then there has been extensive progress in QCLs. In 1997, single mode QCL at RT in a DFB structure was demonstrated [104]. The first CW operation of a QCL at RT was reported by Beck et al. in

2002 [105]. By tuning the energy difference between levels 3 and 2, changing the layer thickness and compositions, the QCLs can now cover an extremely wide spectral range of 2.9-250 μm [106].

The realizations of mid-infrared QCLs are mainly based on three material systems: GaInAs/AlInAs on InP, GaInAs/AlAsSb on InP and InAs/AlSb on InAs. The GaInAs (well)/AlInAs (barrier) structure is the most heavily investigated gain region for QCLs, achieving RT CW operation of the QCLs with more than 10% wall plug efficiency (WPE) and output power of a few Watts in the 4-7 μm range [103]. The band offset between GaInAs and AlInAs lattice-matched to InP is only 530 meV, which is not high enough to provide sufficient confinement for short wavelength lasing. By adding 1% strain in the structure, the band offset can be greatly increased to 800 meV, and 4.6 μm QCLs were realized. When the strain was further increased to 1.6%, the lasing wavelength can be moved to 3.5 μm [107] . In both cases, the QCLs can work at RT in CW mode. The T_0 was reduced from 127 K to 88 K as the wavelength decreased from 4.6 to 3.5 μm, due to increased electron leakage to the lowest energy levels, though it is still higher than most of the QW lasers in this range. However, the J_{th} of this type of QCL at RT (1.7 kA/cm^2 for 4.6 μm laser and 2.3 kA/cm^2 for 3.5 μm laser) is still quite high compared with QW lasers. The GaInAs/AlInAs material system can be implemented by adding AlAs in the barrier. Due to the large lattice mismatch between AlAs and InP, using composite AlInAs/AlAs barrier layers can tune the layer thickness and strain almost independently. The corresponding QCLs can emit at 3.3 μm at RT pulsed mode, with a J_{th} of 3.7 kA/cm^2 and watt-level output power [108]. High output power was also reported from a 3.76 μm QCL at RT CW mode, with a J_{th} of 1.5 kA/cm^2 [109]. Single mode DFB lasers were demonstrated using this kind of QC structure between 3.19 and 3.41 μm at RT with pulsed excitation [110].

The GaInAs/AlAsSb material system on InP substrates can benefit from the high conduction band offset of 1.6 eV, which makes it the most suitable material system for shorter

wavelength QCLs. RT CW operation of this kind of QCLs have been reported in the range between 3.0 and 3.55 μm [111], [112]. However, the growth suffers from the Sb inter-diffusion problem, which makes it difficult to make high quality interfaces. By selectively incorporating AlAs into the active region instead of AlAsSb, the performance of the QCLs emitting around 3.7 μm can be significantly enhanced [113]. The output power at RT pulsed mode was increased from 31 mW [114] to 2.6 W, with a J_{th} of 3.3 kA/cm^2, and 1 W peak power can also be achieved at 400 K [113]. Recently, 3.3 μm QCLs with an GaInAs/AlAs(Sb) active region was also reported. The RT CW output power can exceed 3.5 W [115].

The InAs/AlSb on InAs substrates material system has an even higher conduction band offset of 2.1 eV, making it very suitable for shorter wavelengths QCLs. This type of QCLs at 3.3 μm can work up to 400 K in pulsed mode. The J_{th} at RT was about 3 kA/cm^2, and output power can reach 1 W [116]. QCLs with InAs/AlSb active region emitting at around 2.95 μm can also work at RT in pulsed mode [117]. The 2.6 μm QCLs can only work up to 175 K [118]. The increased carrier leakage from Γ valley to L valley with decreasing wavelength can be the main reason for the degradation of this kind of QCLs' performances [119].

3.8 Interband cascade lasers

One major problem in the development of the QCLs is the fast non radiative relaxation between sub-bands via optical phonon scattering, which is in the order of 1 ps, leading to low radiative efficiency and substantial heating which limit their performance [67]. The idea of interband cascade lasers (ICLs) was first proposed by Yang [120]. Similar to QCLs, the electrons in ICLs can also be re-used after emitting photons. However, the ICLs rely on the interband transition in the active regions, which is fundamentally different from the inter-subband transition of QCLs. The band profile and working mechanism of a typical ICL are illustrated in Fig. 3.14. The "W" active region is composed of two InAs electron wells with one GaInSb hole well in between. After the interband recombination in the "W" region, the

67

electrons on the valence band transfer via either tunnelling or scattering to the first InAs QW in the electron injection region. The semimetal interface between GaSb and InAs, which originates from their broken type II band alignment, helps to maintain the population inversion in the "W" region. The electrons generated at the interface move through the electron injector to the next active region. In a very similar manor to the "W" lasers, the lasing wavelength can be tuned over a wide range by varying the well thickness in the active region. But for longer wavelength lasing, thicker InAs layers are required in the active region, which will consequently decrease the gain due to the reduced wavefunction overlap [121].
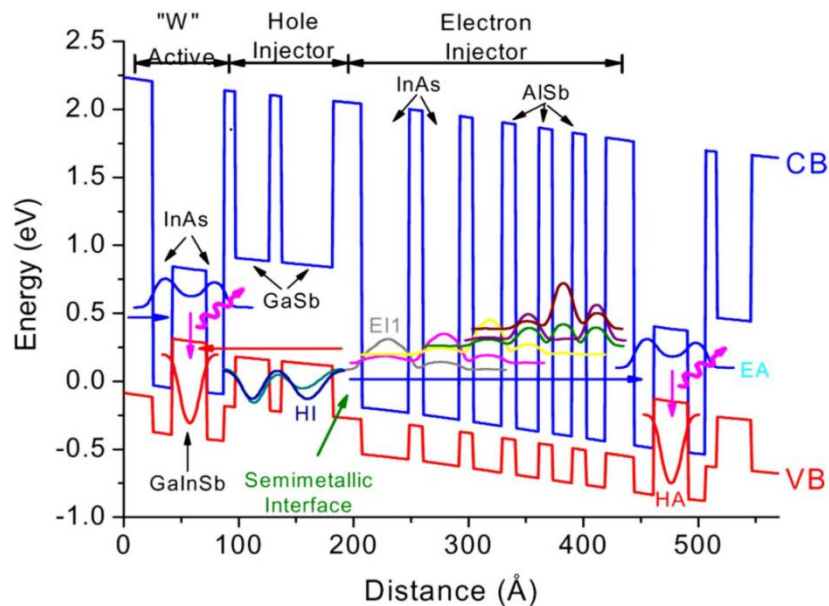
Fig. 3.14 Conduction and valence band profiles for one stage of an ICL under bias, along with the succeeding stage's active region. The "W" active, hole injector, and electron injector regions are indicated, along with some of the more important electron and hole wave functions plotted at energies corresponding to their respective subband extrema under bias [121]**.**

In recent years, very outstanding performances of the ICLs in the mid-infrared range have been reported. RT pulsed mode operation was demonstrated from ICLs containing 5 "W" structure active regions on GaSb substrates, emitting between 3.2 and 4.2 μm [122]. At RT, the J_{th} is in the range between 390 and 630 A/cm^2, and the T_0 is around 39-45 K for all the lasers. By increasing the number of active regions to 7, Canedy et al. reported reduced internal loss and enhanced external quantum efficiency from the ICLs emitting between 2.95 and 4.7

μm [123]. They also demonstrated 3.5 μm ICL working at RT in CW mode, with 592 mW output power. J_{th} below 100 A/cm^2 in pulsed mode has been achieved from an optimized ICL structure with 10 active regions emitting at around 3.7 μm [124]. The lasers can work in CW mode up to 80 °C, with 28 mW output power at RT. By heavily doping the injector regions to rebalance the concentration of electrons and holes, Bewley et al. improved the performance of ICLs between 4.7 and 5.6 μm [125]. These devices can work at RT in CW mode, with J_{th} of 480 A/cm^2 for the 4.7 μm laser and 530 A/cm^2 for the 5.6 μm, comparable with shorter wavelength ICLs.

Single mode ICLs have been made for various kinds of applications. DFB structures with laterally coupled metal gratings produced single mode ICLs working at RT in CW mode, emitting around 3.8 μm [126]. The wavelength can be tuned over 10 nm range, and output power can exceed 6 mW. Kim et al. deposited a thin germanium film to fabricate the DFB structure, which resulted in single mode ICLs around 3.8 μm working up to 80 °C in CW mode with a high output power of 27 mW at 40 °C [127].

3.9 Comparisons
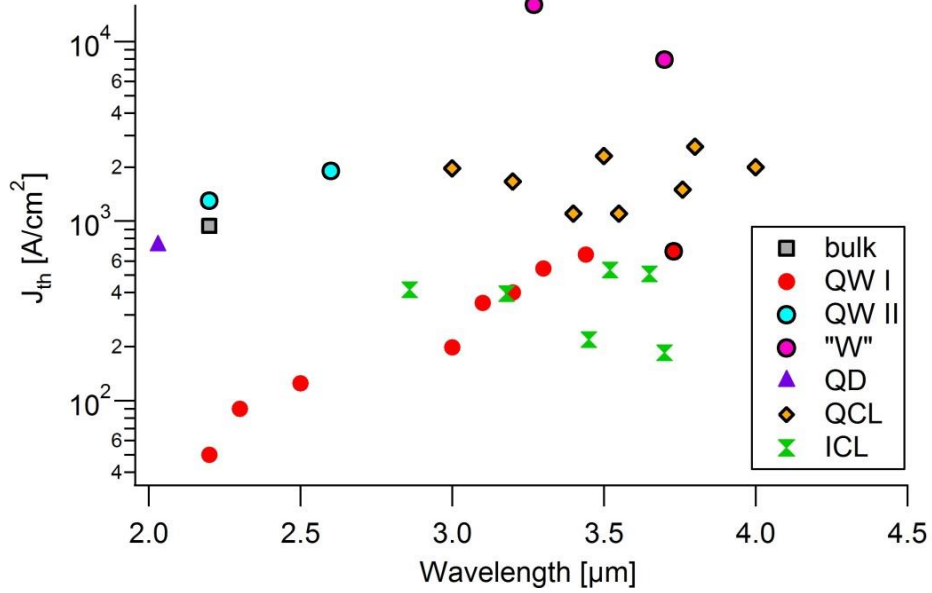
Fig. 3.15 J_{th} of different types of lasers in the wavelength range between 2 and 4.5 µm at RT. The symbols with black strokes signify the values are measured at pulsed operation.

In many different application cases in the mid-infrared range, it is required for the laser sources to work at RT in CW operation. Some types of the lasers discussed above have achieved this goal. The comparison of J_{th} at RT is illustrated in Fig. 3.15. It is clear from this plot that the J_{th} of type I QW lasers at RT in CW operation increases significantly with rising temperature, which is mainly due to the increased Auger recombination. The value of J_{th} is still below 1 kA/cm^2 for up to 3.5 µm. But this type of laser can only work in pulsed mode at RT in the longer wavelength range. Type II QW lasers below 3 µm wavelengths need J_{th} higher than 1 kA/cm^2 to work at RT in pulsed mode, and "W" lasers require J_{th} ~10 kA/cm^2 for above 3 µm wavelengths (at RT pulsed mode). The J_{th} of QCLs in pulsed mode typically falls between 1 and 3 kA/cm^2 in the 3-4 µm spectral range. However, in CW mode, the J_{th} of QCLs is significantly higher (~10 kA/cm^2). Up to date, the ICLs have achieved the lowest J_{th}'s at RT in CW mode (200 to 700 A/cm^2) for the range between 3.2 and 3.7 µm.

Regarding T_0, the values for type I QW lasers at RT decrease with increasing temperature, going down below 60 K above 3 µm. The T_0 of type I QW lasers, "W" lasers, ICLs, QD lasers

and bulk lasers all fall within the range between 20 K and 60 K at RT. Compared to this, QCLs have significantly higher T_0. Above 100 K T_0 has been achieved for 3-4 μm spectral range. It can be related to the fundamentally different transition mechanism in QCLs (inter-subband transition) compared with in other types of lasers (interband transition).
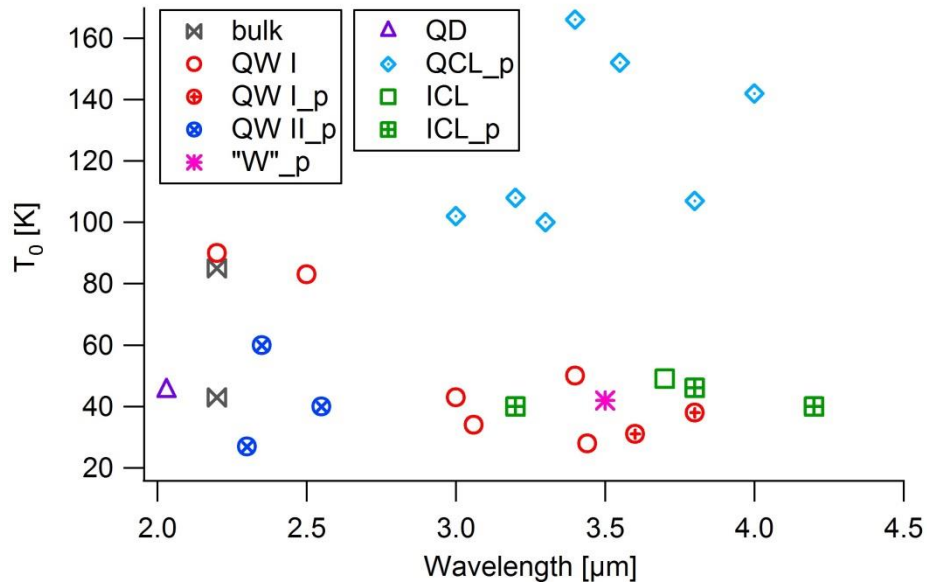
Fig. 3.16 T_0 of different types of lasers in the wavelength range between 2 and 4.5 μm at RT. The symbol '_p' in the legends represents values measured at pulsed mode.

The output power from type I QW laser at RT CW mode is reduced by almost 2 orders of magnitude (from 2 W to 30 mW) when the wavelength increases from 2.2 to 3.5 μm. On the contrary, the output power from QCLs decreases greatly as the wavelength moves from 4 to 3 μm. At around 3.5 μm, QCLs can produce several hundred mW output power, while QW lasers can only give less than 100 mW at RT in CW mode. At this wavelength, ICLs can also generate output power similar to QCLs.
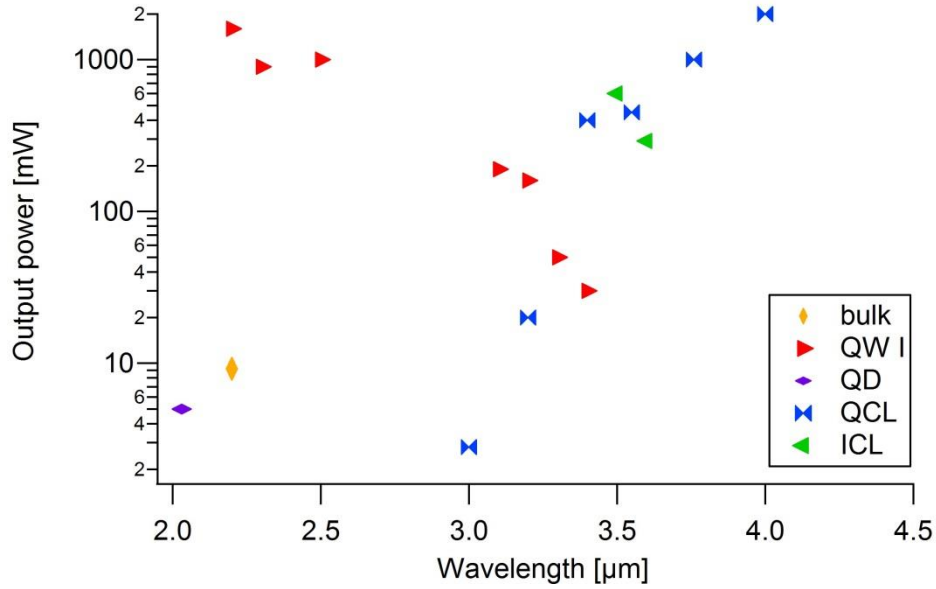
Fig. 3.17 Optical output power at RT in CW mode from different types of lasers in the 2-4.5 μm range.

Putting these three aspects together, at RT in CW mode ICLs show superior performance with low J_{th} and high output power between 3 and 4 μm, only the T_0 are not as high as QCLs. On the other hand, QD lasers only work around 2 μm at RT in CW mode, with high J_{th} and low output power. Although InSb QDs have demonstrated PL and EL within the 3-4 μm spectral range at RT, there is plenty of work to do so as to obtain lasing performance comparable with state-of-the-art mid-infrared laser sources.

4. Experimental procedures

4.1 Molecular beam epitaxy

MBE is an epitaxial process by which the growth of materials takes place under ultra-high vacuum (UHV) conditions (10^{-9} – 10^{-11} Torr) on a heated crystalline substrate by the interaction of adsorbed species supplied by atomic or molecular beams [128]. The deposited layers or structures have: (i) the same crystalline structure of the substrate or a structure with a similar symmetry and (ii) a lattice parameter differing from that of the substrate by no more than ~10%. The atomic or molecular beams are generated by evaporation or sublimation of suitable materials contained in ultra-pure crucibles [129]. The growth rate of MBE is in the order of 1 monolayer per second. With the help of the shutters placed in front of the crucibles, this slow rate ensures the control of the deposited material composition in monolayer precision.

4.1.1 Growth apparatus
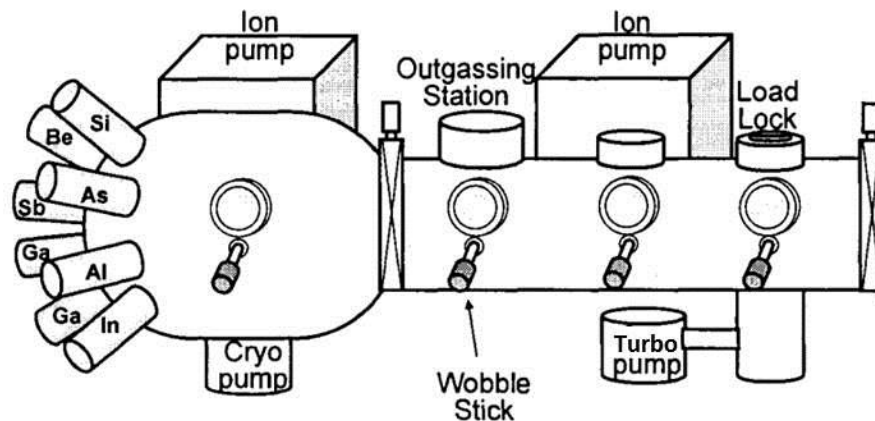
Fig. 4.1 Schematic drawing of the VG V80H MBE system used in this work.

A VG V80H MBE system was used to grow the materials and structures in this work, which is illustrated in Fig. 4.1. The substrates are first introduced into the system through the load lock, and then baked at the outgassing station, typically at 350 °C. Before opening the valve to the growth chamber, the turbo pump and the ion pump ensure the pressure in the introduction

chamber is in the range of 10^{-9} mbar. The ion pump together with the cryo-pump keeps the UHV condition in the growth chamber. The growth chamber is equipped with group-III, Ga, Al and In effusion cells, group-V As and Sb effusion cells, Si and Be effusion cells for *n* and *p* type doping. A liquid nitrogen cooled cryo-panel is placed around the growth chamber, which provides thermal isolation between different cells and help maintain the ultra-low pressure inside the chamber.

Fig. 4.2 gives more details of the inside of the growth chamber. The substrate holder is mounted on the wafer manipulator which rotates the substrate during the growth to improve sample uniformity. The vertical axis can also be rotated so that the ion gauge faces the cells. The ion gauge is used to measure the beam equivalent pressure (BEP). High energy electrons are emitted from the reflection high energy electron diffraction (RHEED) gun, after striking on the surface of the sample, reflect patterns on the fluorescent screen.
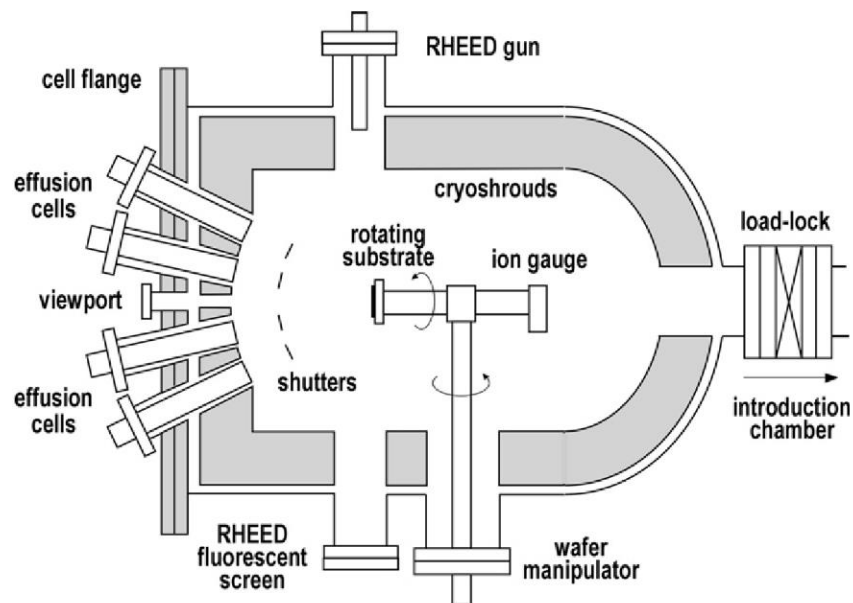
Fig. 4.2 Schematic view inside an MBE growth chamber [129]**.**

The material fluxes are generated from Knudsen cells. Inside a Knudsen cell, the solid state material is contained in an inert crucible which is radiatively heated by Ta ribbons or wires. The cell temperature is monitored by a thermocouple, and accurately controlled by a closed-

loop controller. By changing the cell temperature, the material flux can be varied. For In, a dual element cell is used, which consists of a tip heater for the crucible lip at the aperture region, and a base heater for the crucible body. Valved cracker cells are used for group-V materials. Fig. 4.3 below shows an example of As valved cracker cell. As is first thermally evaporated from the crucible in the form of As_4. After passing through the needle valve, the As_4 enters into the cracking stage, where it can be transformed into As_2. The cracking is achieved by interactions of tetramers with surfaces at a high temperature (set at 950 °C in the experiment). The base temperature is kept at 360-380 °C for As and 580-590 °C for Sb. The fluxes of the materials can be controlled by the position of the needle valves [129].
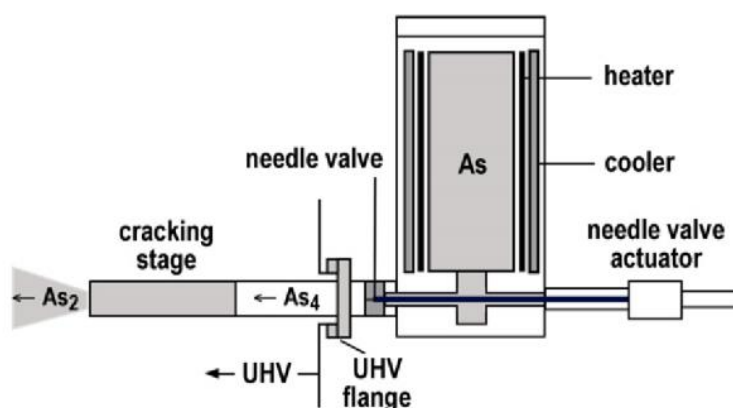
Fig. 4.3 Schematic cross-sectional view of a As valved cracker cell [129]**.**

4.1.2 RHEED

RHEED is an important tool in monitoring the growth in MBE systems. The technique is based on an electron gun that produces a beam of electrons with energies of 10-15 keV and a fluorescent screen where electrons diffracted from the sample surfaces form the diffraction pattern. The angle between the beam and the surfaces is in the range of 0.5-2.0 °. The patterns can be analysed visually or by image processing tools, providing real-time in-situ analysis of the growth.

The RHEED pattern can be used as an indication of surface morphology. On a perfectly smooth surface, the electron beam under grazing incidence (0.5-2.0 °C) is diffracted by a two-

dimensional lattice, resulting in streaky patterns on the screen. In the case of a rough surface, the electron beam interacts with a three-dimensional lattice, which is represented by spotty patterns on the screen. The diffraction pattern depends on i) the azimuth of the impinging electron beam with respect to the crystallographic directions of the surface, and ii) surface reconstruction during the growth. Fig. 4.4a gives examples of the RHEED patterns from GaAs growth under As-rich condition. After a few seconds from the start of growth, the pattern transforms from spotty to streaky, indicating layer-by-layer growth has been established. The integer order streaks correspond to the position of spotty patterns at the beginning. In (011) and (0-11) azimuths, the pattern is characterized by one or three fractional streaks between the integer ones respectively, indicating a 2x and 4x periodicity of the GaAs surface in these two directions. The 2x4 surface reconstruction is a feature of As-stabilized growth. Under Ga-rich growth conditions, the pattern would have 4x2 periodicity [129].

(a) (b)
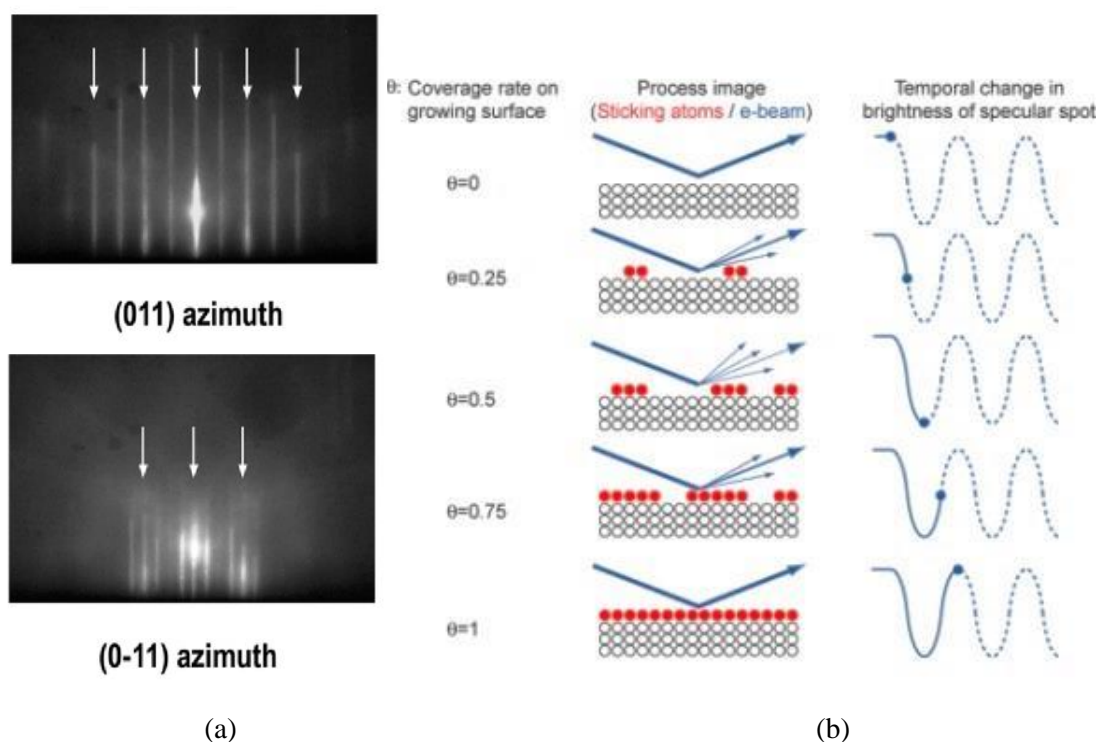
Fig. 4.4 (a) RHEED patterns observed along the (011) and (0-11) azimuths during the MBE growth of epitaxial GaAs on a (100) GaAs substrate. The arrows mark the position of integer order streaks [129]**. (b) Different stages of 2D layer-by-layer growth mode and the corresponding RHEED intensity with time.**

In 2D layer-by-layer growth, the RHEED pattern can also be used to estimate the growth rate. On a smooth surface, the RHEED pattern is bright. When the deposition of one additional monolayer starts, islands and atoms on the surface can make the pattern become dim. As half of the surface is covered, the pattern would become the darkest. Finally, when the whole monolayer is formed, the smooth surface can be reconstructed and the RHEED recovers to be bright again. These different stages are illustrated in Fig. 4.4b. This one circle of the brightness oscillation corresponds to the deposition of one monolayer. One monolayer of (001) GaAs has the thickness of 0.283 nm. So by estimating the RHEED oscillation frequency, the growth rate of GaAs can be measured.

4.1.3 Flux calibration

The fluxes from the material sources cannot be directly measured in the MBE system. The reading of BEP is proportional to the flux arriving at the sample surface and hence the growth rate. In the calibration stage, for group-III material, the BEP dependence on cell temperature was measured. And for group-V material, the values of BEP's were measured with different valve positions. By comparing the BEP values, the cell temperature or valve positon can be adjusted to obtain the desired growth rate.

4.2 Material characterization

Before processing the material into devices, the composition and crystal structure of the materials grown in MBE need to be characterized by X-ray diffraction and photo-luminescence from the materials and nanostructures was carried out to determine the band gaps and emission characteristics.

4.2.1 X-ray diffraction

Double crystal X-ray diffraction (XRD) was used to study the composition of the grown materials and to estimate the layer thickness of nanostructures. The wavelength of X-rays is in

the same order of the atomic spacing in semiconductors, so the periodic structural characteristics can be probed from the diffraction patterns of the X-ray. For the rays to interfere constructively, the Bragg condition must be satisfied:

$$2d_{hkl}sin\theta_B = n\lambda \tag{4.1}$$

where d_{hkl} is the lattice plane spacing, θ_B the Bragg angle dependent on the material, n an integer and λ the wavelength of the X-ray. Materials with different lattice plane spacing require different angles to meet the Bragg condition [130].

A QC200 Double Crystal XRD system from Bede Scientific Instruments was used. A schematic drawing of the set-up is shown in Fig. 4.5 below. High energy electrons are produced from a hot filament, and accelerated to strike a copper target which causes electrons in the innermost K-shell to be ejected. An electron from a higher L-shell falls into this vacant site in the K-shell and the radiation is emitted in the form of X-Rays Cu κα1 and Cu κα2. A slit in front of the detector was used to screen Cu κα2 radiation. Double axis rocking curve measurements were performed using this XRD set-up. The sample was first aligned by adjusting the position of the plate, the rotation angle and the tilt angle. The Bragg angle of the substrate material was found by changing the X-ray incident angle ω. The position of the detector was represented by the 2θ angle shown in Fig. 4.5, which equalled twice the value of the incident angle ω. During the ω-2θ scan, both the sample plate and the detector were moved at the same time (i.e., if the plate was rotated by α degree, the detector was rotated by 2 α degree). RADS Mercury software was used to analyse the rocking curves. The lattice mismatch, strain, and layer thickness of the grown material can be estimated from the measured data.
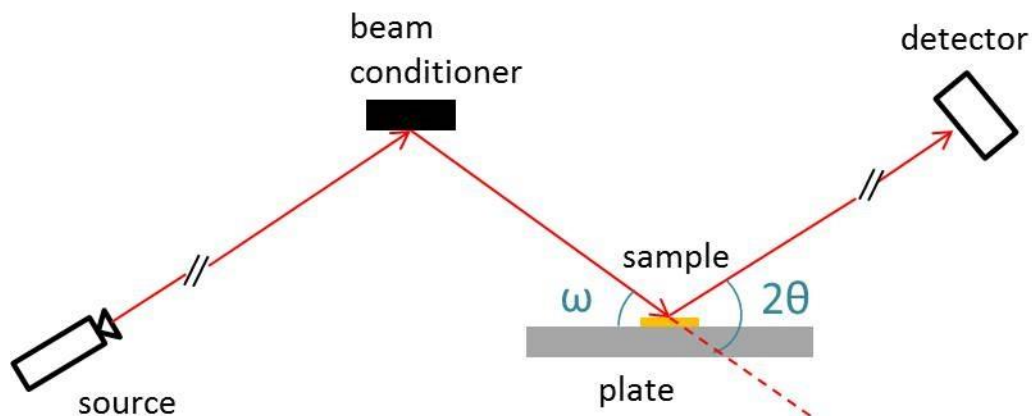
Fig. 4.5 Schematic drawing of the XRD set-up.

4.2.2 Photo-luminescence

The Photo-luminescence (PL) spectroscopy measurement set-up is sketched in Fig. 4.6. A class 4 Argon ion laser with a drive current of 20 A emitting at 512 nm was used to excite the samples. The laser light was chopped on its path by the chopper at a frequency of ~ 180 Hz. After reflections from the three beam steering mirrors and passing through a focusing lens, the laser light hit the sample surface with a spot size of around 1 mm^2. The highest intensity from the Ar laser was 1.4 W, neglecting the losses in the optical path, it corresponded to up to 14 W/cm^2 on the sample surface. The sample was placed inside the cryostat which can be cooled down to 4 K using liquid helium. The emitted light from the sample together with the laser light reflected by the sample surface travelled through three focusing lenses. Before entering into the monochromator, the laser light can be blocked out by the optical filters placed in front of it. Depending on the PL wavelengths, 1.04, 1.9 and 3.8 μm optical filters can be used. The two slits at the entrance and the exit of the monochromator can be adjusted in width to help improve the resolution. The smallest step of the monochromator corresponded to 1 nm in wavelength. A Graseby liquid nitrogen cooled InSb photo detector behind the monochromator exit slit collected the PL signal, which, after passing through the pre-amplifier, was fed into the Stanford SR830 DSP lock-in amplifier. The chopper provided the lock-in reference signal. After the two amplifiers, the signal was send to the Labview program in the PC, which also

controlled the grating position of the monochromator through the stepper motor controller. It needs to be noted that the amplified signal sent to the program was in the unit of volt, not the intensity of the PL signal, so this set-up can only measure the relative intensity of the PL emission.
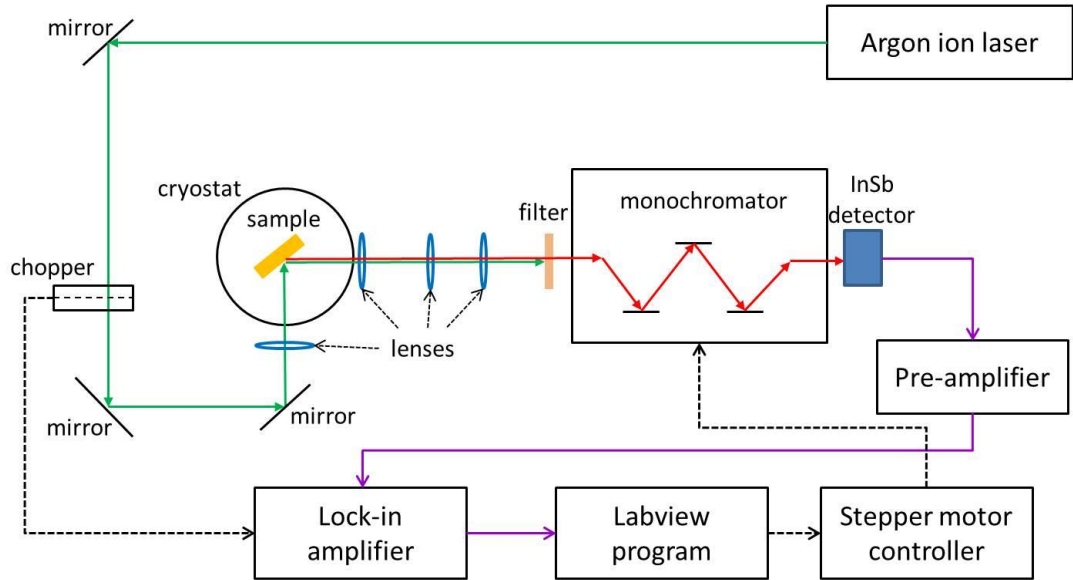
Fig. 4.6 Schematic drawing of the PL measurement set-up. Green lines: Ar laser optical path; red lines: PL emission optical path; purple lines: detected signal flow; dashed back lines: electronic control signal flow.

The excess carrier concentration generated in the sample from the Ar laser excitation can be estimated from:

$$n = \frac{I\alpha\tau}{h\nu} \tag{4.2}$$

where I is the incident power intensity, α is the absorption coefficient (2×10^4 cm^{-1} for InAs), τ is the carrier lifetime and $h\nu$ is the photon energy of the argon laser (2.4 eV). At 10 W/cm^2 excitation, and assuming a carrier lifetime of 1 ns, the carrier concentration in the material can be estimated to be around 5×10^{14} cm^{-3}.
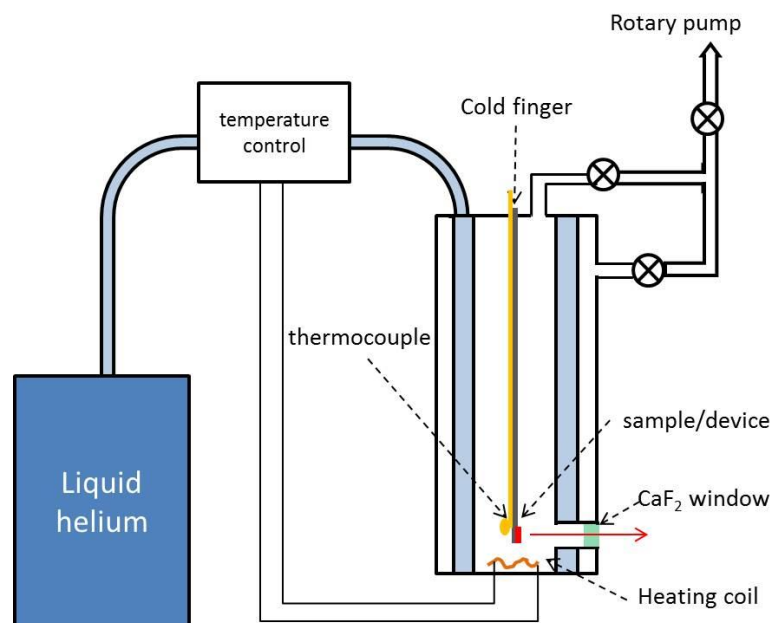
Fig. 4.7 Illustration of the cryostat for PL measurement.

The temperature of the sample can be controlled by the cryostat in the range of 4-300 K. The sample was attached at the end of the cold finger, which was then put into the inner chamber of the cryostat. Thermal exchange gas (helium) was delivered to this chamber and sealed inside it. The outer chamber acted as the thermal isolation. During the measurement, it was connected to the rotary pump which kept the pressure around 4×10^{-2} mbar. Liquid helium flew constantly between the two chambers to cool the inner chamber and the sample through the exchange gas. A heating coil at the bottom of the chamber can heat up the inner chamber to adjust the temperature. The temperature was set on the temperature control panel, which can adjust the flow of the liquid helium and the current in the heating coil. A thermocouple was attached near the sample on the cold finger, which can measure the actual sample temperature during the experiments. The cryostat structure is shown in Fig. 4.7.

4.3 Laser processing

In this section, the procedures to make Fabry-Perot broad area laser diodes will be discussed in detail. (The laser stripes are 75 μm in width, between 0.3 and 1.5 mm in length).

4.3.1 Photolithography

The samples were first rinsed in acetone, IPA and de-ionized water, blown dry with compressed nitrogen gas. After that, they were mounted on a Suss Microtec spinner, in which the samples were held by the vacuum chuck. A few drops of LOR 3B photoresist were applied on the sample surfaces, and spun at 4000 rpm for 30 seconds, resulting in a thickness of about 400 nm for the photoresist. Then the samples were baked at 180 °C for 2 minutes. Afterwards, S1805 photoresist was applied on top of the samples and spun for the same speed and time, baked at 120 °C for 2 minutes. The thickness of S1805 was about 500 nm. A mask with parallel stripes in 75 μm width and 225 μm spacing was used to define the laser geometry. The samples with photoresists on top were mounted on a Suss Microtec MJB4 mask aligner. Soft contact mode was used during the exposure, which means the sample and the mask were in contact, but no additional pressure was added between them. The ultraviolet lamp (260 W) illuminated the samples for 1.0 second. At last, the samples were developed in MICROPOSIT MF-CD-26 developer for about 30 seconds and rinsed in de-ionized water. After these processes, the patterns of the laser stripes were developed on the samples.

4.3.2 Metallization

The samples with photoresist patterns were put into a Moorfield evaporator, together with cleaned Au and Ti wires into their respective coils. The pressure inside the evaporation chamber was first reduced to the order of 10^{-6} mbar, and the shutter of the samples was closed. The Ti coil was first heated by gradually increasing the current through it to about 70 A. Once the pressure inside the chamber became stable, the shutter can be opened, which started the deposition of Ti. The current can be finely tuned so that the deposition rate was about 1 Å/s. About 20 nm thick Ti needed to be deposited on the sample and then the shutter was closed.

The current in Ti coil was gradually reduced to 0 and in the Au coil it was increased to around 27 A. The shutter was opened again so that the deposition of Au can start. About 180 nm thick Au was needed on top of the Ti at a rate of around 2 Å/s.

4.3.3 Lift-off

The samples deposited with Ti/Au were dipped into MICROPOSIT 1165 remover for at least 5 minutes. The undercut effect of LOR 3B resist assists the remover to dissolve the resists quickly. The metal on top of the photoresists should come off the sample automatically, leaving only metal stripes on the sample surfaces.
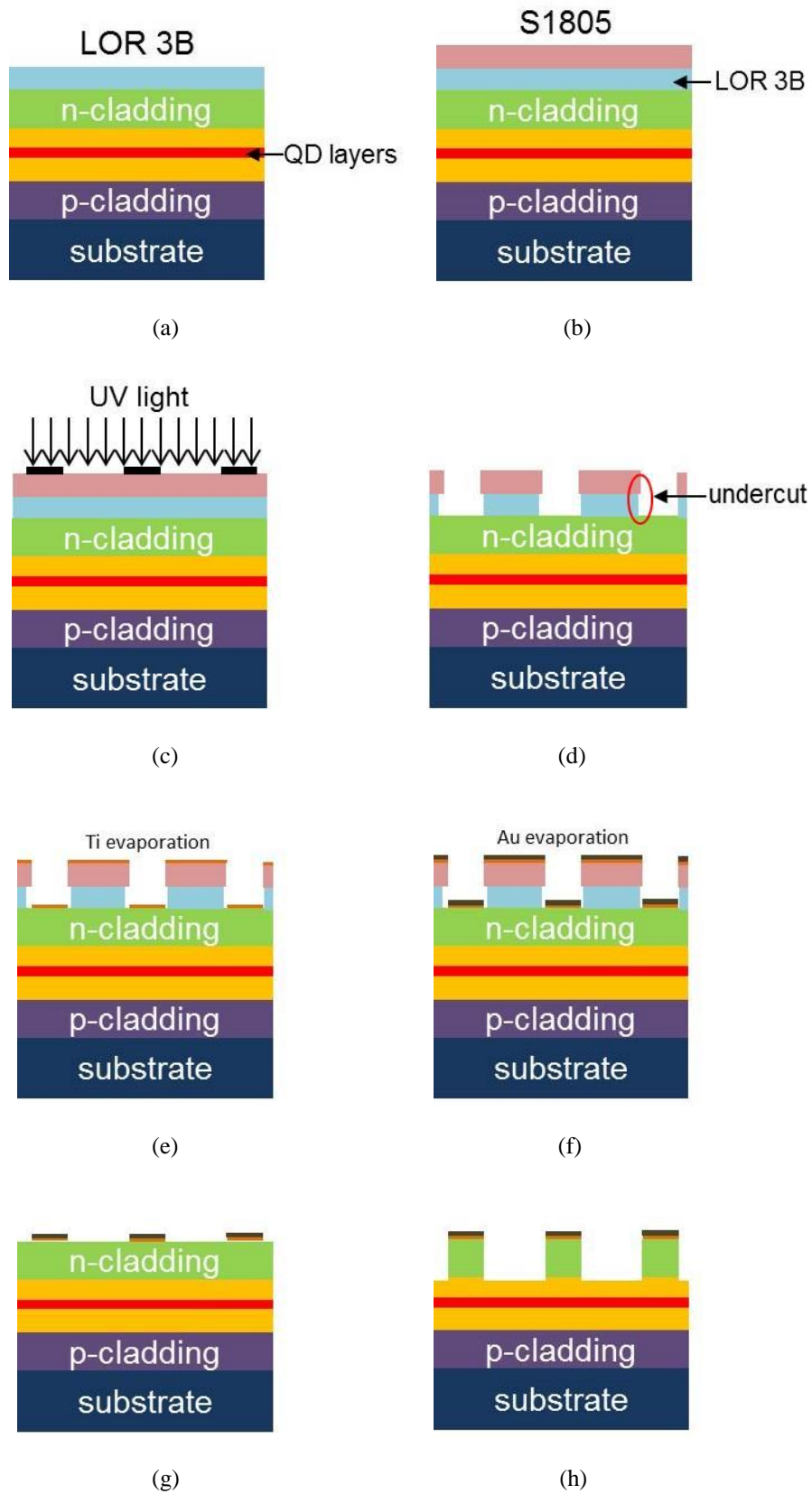
Fig. 4.8 Clean room laser processing steps of (a) LOR 3B deposition, (b) S1085 deposition, (c) photolithography, (d) developing, (e) Ti evaporation, (f) Au evaporation, (g) lift-off and (h) wet etching.

4.3.4 Wet etching

In order to form a waveguide structure, the upper part cladding layer without metal coverage needs to be etched away. In the case of the 2.0 μm thick n+ InAs cladding layer, two-step wet etching was used. The sample was first dipped in H_3PO_4: H_2O_2: H_2O (1: 1: 1) to etch away 1.5 μm thick n+ InAs with an etching rate of about 1.3 μm/min. Then the sample was dipped into H_2SO_4: H_2O_2: H_2O (1: 8: 80) to etch away the rest of the cladding layer and the top fraction (about 100 nm) of the InAs waveguide with an etching rate of about 1.0 μm/min. After each step, a profile meter was used to measure how much material had been removed. This two-step etching technique can help reduce the surface leakage current in the laser diodes [131].

In the case of AlAsSb top cladding layers, a solution of HCl: H_2O_2: H_2O (1:1:10) was used. The etching rate can be around 8 μm/min. It is more problematic than the InAs etching, because of the fast etching rate and quick oxidation of Al on the material surface once exposed into the air, which can terminate the etching process. To avoid this issue, the etching of AlAsSb must be done in one dip, though it would be more difficult to control the etching depth.

4.3.5 Lapping

After etching, the sample was mounted upside down in the slot of a metal chuck with melted wax on a heated plate. The slot was 200 μm in depth. Al_2O_3 powder in 3 μm mean size was mixed with water to create slurry on a glass plate. The sample on the metal chuck was then lapped on the slurry in an "S"-shaped path for a few minutes. After that, the backside sample surface was polished in the same way in a slurry with 0.3 μm mean size Al_2O_3 powder. By heating the chuck on the hot plate again, the thinned sample can be removed from the chuck, and the remaining wax on the sample was cleaned in boiling n-butyl acetate for 2 minutes. The sample thickness was reduced to 150-200 μm after this process. Lapping is a necessary

step in laser processing, which ensures high quality end facets when cleaving the samples and reduces the series resistance of the lasers.

4.3.6 Backside metallization

After lapping, the sample was put back into the evaporator. In the same way, a Ti/Au metal contact of the same thickness was deposited on the backside of the sample. Backside metallization can help to make good ohmic contacts between the laser diodes and the headers.

4.3.7 Cleaving and mounting

The sample was cleaved using a knife or a diamond pen into laser chips with several parallel laser stripes in 0.3 to 1.5 mm length. The chips were then attached to T0-46 header by using Epotek H20E two part epoxy mixed in the ratio of 1:1, which was cured by baking in the oven for 2 hours at the temperature of 180 °C.

4.3.8 Wire bonding

An Accelonix TPT HB05 manual wire bonder was used to connect the top electrical contacts of the laser chips to the headers with 15 μm thick gold wires. The bonder worked in ball bonding mode, in which a ball-shaped contact was formed between the chip and the wire, and a fishtail-shaped contact was used between the wire and the header. During the process, the header with the laser chip was mounted on a heated plate set at 100 °C. 150 and 450 Watt ultrasonic powers were generated when forming the contacts on the chip and on the header respectively. A microscopic picture of a laser chip on a T0-46 header after wire bonding is shown in Fig. 4.9 below.

Fig. 4.9 Microscopic picture of a laser chip on a T0-46 header and wire bonded to it.

4.4 Device characterization

The electrical properties of the devices can be characterized from the current-voltage measurement set-up. The electrical luminescence can be measured by the EL set-up. The multimodal spectra of the lasers can be measured from FTIR spectroscopy.

4.4.1 Current-voltage measurement

Current-voltage (I-V) characteristics of the devices were obtained using a Keithley 2400-LV SourceMeter (C) interfaced to a Labview program. The computer software allowed an increasing voltage to be passed across the device in small steps and at the same time the corresponding current was recorded. An upper current limit can be set to avoid damage to the device.

4.4.2 Electro-luminescence
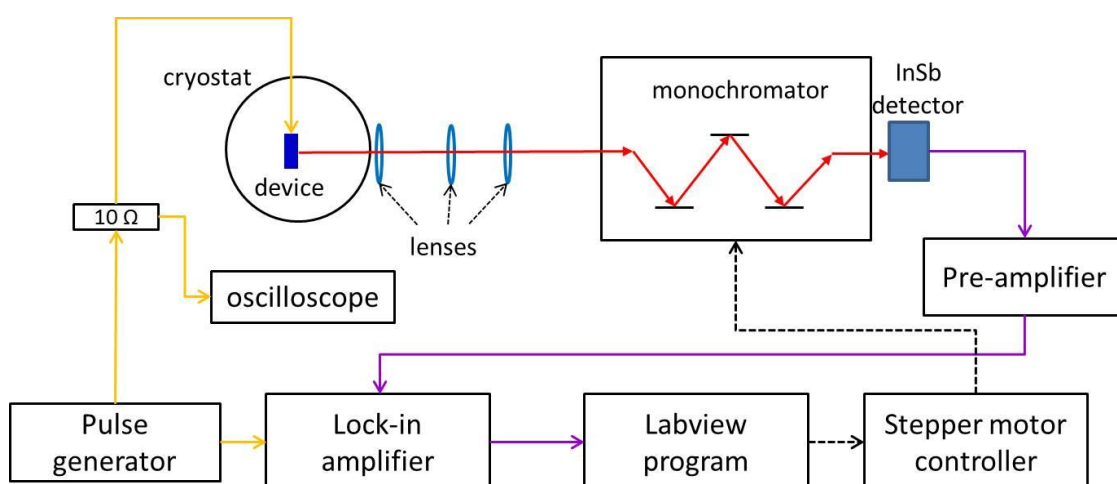
Fig. 4.10 Schematic drawing of the EL measurement set-up. Red lines: EL emission optical path; yellow lines: electrical excitation signal flow; purple lines: detected signal flow; dashed back lines: electronic control signal flow.

Electroluminescence (EL) measurement can be carried out by modifying the PL measurement set-up. The Ar laser excitation was replaced by the electrical output from an Agilent 8114A pulse generator. Before going to the devices, the electrical pulses first passed through a 10 Ω resistor, through which the exact current was measured by an oscilloscope. The reference signal for the lock-in amplifier was also from the pulse generator. Fig. 4.10 sketches the EL set-up, which is the same as in the PL set-up, the output power cannot be measured directly in this experiment, but the integrated EL intensity is proportional to the emitted power.

4.4.3 Fourier transform infrared spectroscopy

Fourier transform infrared spectroscopy (FTIR) can obtain an infrared spectrum of absorption, emission, Raman scattering, etc. from a solid, liquid or gas sample. An FTIR spectrometer simultaneously collects spectral data in a wide spectral range. This confers a significant advantage over a dispersive spectrometer which measures intensity over a narrow range of wavelengths at a time.

4.4.3.1 Working principles

The mechanism of FTIR spectroscopy is based on the Michelson interferometer. The structure of a Michelson interferometer is sketched in Fig. 4.11. Broadband infrared light originates from the light source L, and impinges upon a beam splitter BS. The BS transmits 50% of the light to the mirror M2 and reflects the other 50% light to the mirror M1. The light reflected off the two mirrors is passed/reflected by the BS again, and the two beams (E1 and E2) recombine on the other side of the BS. Finally the recombined beam hits onto the detector D. In FTIR spectroscopy, one mirror (M1) is held in a fixed position relative to the BS during the measurement. The other mirror (M2) scans back and forth relative to the BS.
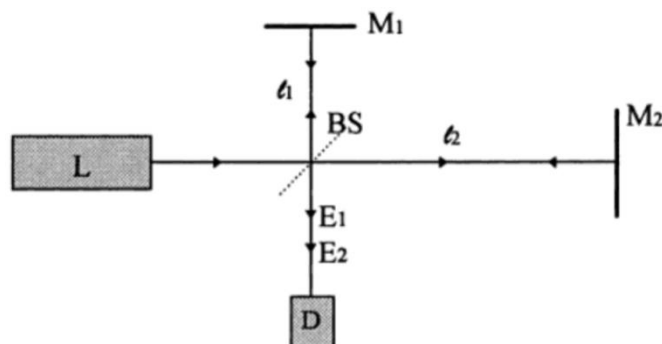
Fig. 4.11 The Michelson interferometer: L is the light source, BS is the beam splitter D is the photo detector and M are mirrors [132]**.**

At each position of the moving mirror, the detector collects the interfered light of the two beams for the whole wavelength range. The interference is dependent on the optical path difference of the two light beams, which is determined by the position of the moving mirror. So the intensity registered at the detector is a function of the moving mirror positon. This relation can be translated through a Fourier transform to extract the spectrum of the light source.

4.4.3.2 Rapid scan

In the rapid scan mode, the moving mirror scans forward and backward in a rapid continuous fashion. At the same time, a Helium-Neon (HeNe) laser beam travels in the exact same optical

path as the infrared light source, before it finally hits the detector. The monochromatic light from the HeNe laser results in constant frequency and constant amplitude interferogram as the mirror moves at a constant speed. This signal generates electronic "counts" which triggers the detector to digitize the detected infrared light intensity. Although in rapid scan mode, the mirror moves in a continuous fashion, the stored infrared interferogram is actually a digital point-by-point plot of detector intensity against the mirror position.

4.4.3.3 Step scan

In the step scan mode, the moving mirror is stepped to a fixed position and held there when the detector is collecting the signal. Then the mirror is stepped to the next position and the measurement is repeated. The resolution is determined by the distance between steps. In order to improve the signal to noise ratio (SNR), one can co-add time slices "in-step", that is, the moving mirror continues to remain at the given position, while the light source was triggered for a number of times and the detected signal is averaged before being stored.

4.4.3.4 Emission measurement

A Vertex 70 FTIR set-up from Bruker was used in our experiments to measure the emission spectra form lasers and LEDs. Both rapid scan and step scan can be used. The set-up for rapid scan measurements is illustrated in Fig. 4. 12. The tested device was cooled in the liquid helium cryostat in the same way as for PL/EL measurements. The emitted light was collected through two lenses and a concave mirror before going into the FTIR system. An InSb detector was used for the mid-infrared spectral range. The same set-up of the electrical excitation as in EL measurement was used. Typical pulse frequency was set as 30 KHz. The scanning frequency of the FTIR system must be at least twice lower than the excitation pulse frequency, and was typically set at 10 KHz. In order to improve the SNR, more than 8 times of scans were repeated for one measurement. Unlike the aforementioned PL/EL measurement using a monochromator, the resolution of FTIR spectroscopy is not limited by diffraction. The highest

resolution of the FTIR system was 0.5 cm^{-1}, corresponding to 0.45 nm at 3 μm wavelength, which is significantly higher than in PL/EL measurements.
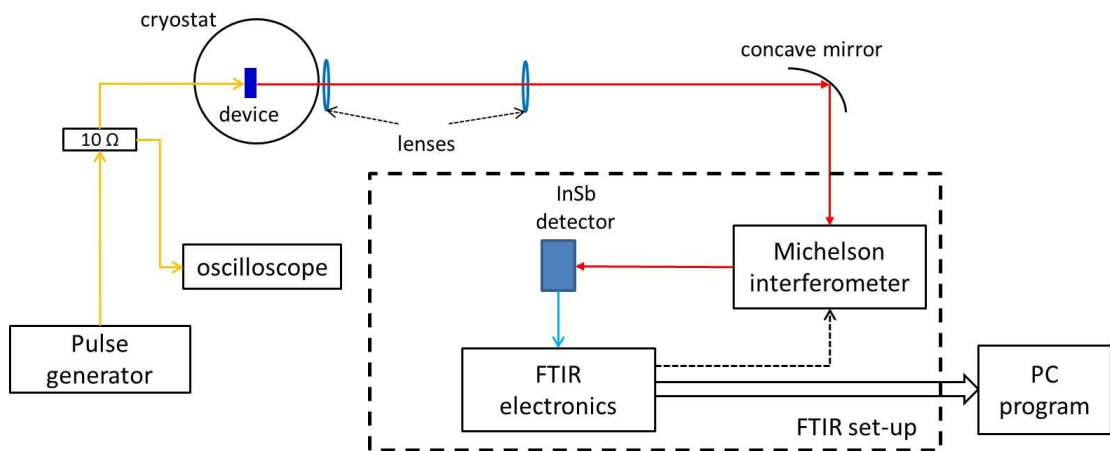
Fig. 4.12 Rapid scan FTIR spectroscopy of emission from lasers or LEDs. Red lines: optical path of the emitted light; yellow lines: electrical excitation signal flow; blue line: detected signal flow.

Using step scan instead of rapid scan can boost the SNR and increase the sensitivity to detect weak signals (e.g. below threshold emission from the end facet of a laser). The set-up needs to be modified, and is sketched in Fig.4. 13 below. At each mirror position, the detected signal was first sent to the lock-in amplifier, which was synchronized with the pulse generator. The amplified signal was then sent back to the FTIR system. During the measurement, the stabilization delay time, which was the time difference between each mirror step, was typically set to be 600 ms. The number of co-added counts needed to exceed 20 to achieve both high SNR and high sensitivity. The high resolution in step scan is the same as in rapid scan (0.5 cm^{-1}). The advantages of step scan compared with rapid scan are obtained at the cost of the time. Typically, a high resolution step scan can take 20 minutes or even longer.
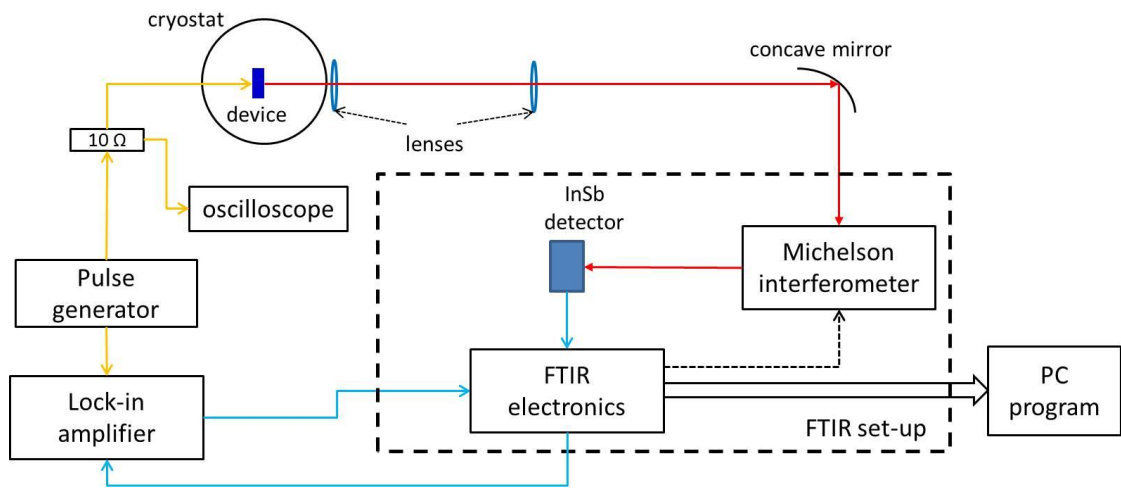
Fig. 4.13 Step scan FTIR spectroscopy of emission from lasers or LEDs. Red lines: optical path of the emitted light; yellow lines: electrical excitation signal flow; blue line: detected signal flow.

5. Metamorphic integration of InSb quantum dots on GaAs substrates

5.1 Introduction

In previous chapters, we have shown the growth of type II InSb/InAs QDs by using molecular beam epitaxy (MBE) [95]. PL of the QDs between 3 and 4 µm has been obtained up to room temperature [133]. In addition, room temperature InSb QD light emitting diodes (LEDs) grown onto InAs substrates have been demonstrated [90]. These QD PL and LED samples were all grown on InAs substrates. Integrating the InSb QDs onto GaAs substrates would provide access to the mid-infrared spectral range, using a more convenient and inexpensive substrate with associated mature processing technology, opening up new possibilities for device applications.

In this chapter, we investigated and compared the use of different buffer layer designs to accommodate the lattice mismatch between InAs and GaAs and then evaluated the properties of the InSb QDs grown on the resulting InAs metamorphic buffer layer in each case. High resolution X-ray diffraction (XRD) and cross-sectional transmission electron microscopy (TEM) techniques were used to study the strain, interfaces and the dislocations in all the grown samples. The optical properties of both the buffer layers and the QDs were examined using PL spectroscopy and were compared with QDs grown onto homo-epitaxial InAs. Subsequently, electroluminescence (EL) from the InSb QDs on GaAs was examined from p-i-n diodes fabricated containing 10 layers of InSb QDs in the active region.

5.2 Metamorphic growth techniques

To deposit the InSb/InAs QDs on GaAs substrates, one must first accommodate the large lattice mismatch between InAs and GaAs ($\Delta a/a_0 = 7.2\%$). Depending on the growth conditions,

during the initial stages of InAs deposition on GaAs either self-assembled islands or 2D films can be formed [134][135]. Experimental work has shown that during MBE growth the strain becomes fully relaxed after 7 nm of InAs being deposited under indium rich conditions [136]. Consequently, a high density of threading dislocations can be expected to appear in the epilayer, which serves as the major strain relief mechanism [137]. Previous studies of thick InAs epilayers on GaAs substrates have revealed that the structural and transport properties of InAs are dependent on the substrate temperature during the MBE growth [138]. However, thick buffer layers are often undesirable and besides direct metamorphic growth, other techniques can also be used for the growth of highly lattice-mismatched materials by MBE. For example, the epitaxial growth of GaSb on GaAs substrates has been demonstrated by inserting AlSb interlayers with different thickness and surface treatments [139], such that a 1.2 nm thick AlSb interlayer can give the smallest roughness and best interface quality [140]. Another approach is to intentionally form an interfacial misfit (IMF) dislocation array with large lattice mismatch, in which the strain energy is released through the laterally propagating dislocations (90º misfit dislocations) localized at the interface [141], rather than by the threading dislocations which propagate up through the epilayer. The IMF technique has been demonstrated using MBE in a range of material systems including, GaSb/GaAs, InP/GaAs, InAs/GaAs, GaP/Si and AlSb/Si, with the lattice mismatch ranging from 0.4% to 13% [142].
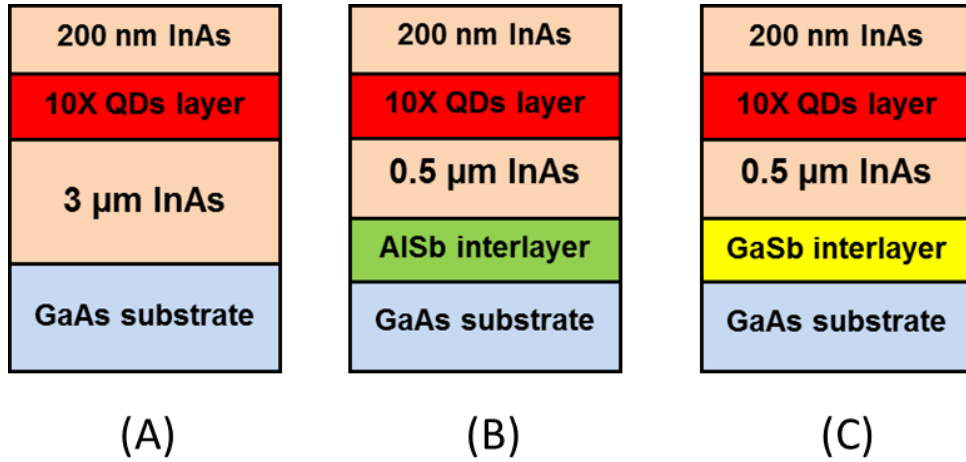
Fig. 5.1 Schematic diagrams of the three QDs samples grown on GaAs substrates. (a): Sample (A), 10 layers of QDs deposited on top of 3 μm thick InAs buffer layer grown directly on GaAs substrate. (b): Sample (B), 10 layers of QDs deposited on top of 0.5 μm thick InAs buffer layer with AlSb interlayer on GaAs substrate. (c) Sample (C), 10 layers of QDs deposited on top of 0.5 μm thick InAs buffer layer with GaSb interlayer on GaAs substrate. All samples are capped with 200 nm InAs.

As shown in Fig. 5.1, three different metamorphic buffer layers were used for the growth of InAs on GaAs substrates before the start of the InSb QD growth. In sample (A), a 3 μm thick InAs buffer layer was grown directly on GaAs. In sample (B), an AlSb interlayer was first deposited on the GaAs, followed by a 0.5 μm thick InAs buffer layer. In sample (C), a thin GaSb layer was grown on the GaAs substrate using the IMF technique, followed by a 0.5 μm thick InAs buffer layer. In all three samples, ten layers of InSb QDs were grown on top of the respective InAs buffer layers using the same growth parameters. The InSb QD growth originates from an Sb-to-As anion exchange reaction [94]. For all the present samples, 0.8 monolayer of InSb was deposited during the growth of each QD layer. The InAs spacer between QD layers was set to be 20 nm and the samples were each capped with a 200 nm layer of InAs. In each case, at the beginning of the growth, a 15 nm thick GaAs layer was first deposited to smooth the substrate surface. The InAs buffer layers were all grown at 550 ℃. The AlSb interlayer in sample (B) and the GaSb interlayers in sample (C) were deposited at 620 ℃ and 600 ℃ respectively. The substrate temperature was reduced to 490 ℃ for the growth of QDs layers and the InAs spacers in all samples.

5.3 TEM observations

Cross-sectional dark field TEM images were taken for all the three samples in order to investigate the interface structure and dislocation density. Fig. 5.2a shows the cross-sectional TEM image of sample (A), where the inset shows details of the InSb QD region. As expected, a large density of threading dislocations nucleated at the interface between the GaAs and the InAs buffer layer, after which the threading dislocation density becomes reduced with increasing InAs thickness. It is clear from the TEM picture that, after 3 μm thick InAs growth, the dislocation density becomes much lower than at the interface. Although QD layers can be used for dislocation filtering [143], in our case threading dislocations were seen to penetrate through several layers of QDs, as shown in the inset of Fig. 5.2a, which is perhaps because of the sub-monolayer thickness of our InSb QDs. In fact it may be noticed that the first few QD layers actually result in the formation of some additional dislocations. For the exchange growth of InSb QDs, the indium cell temperature needs to be reduced in order to lower the indium flux. During the growth of the first few QD layers, the temperature may not have fully stabilized. The spacing between the adjacent QD layers at the bottom is a little larger compared with the spacing between the top QD layers, consistent with a higher indium cell temperature which results in a higher InAs deposition rate.
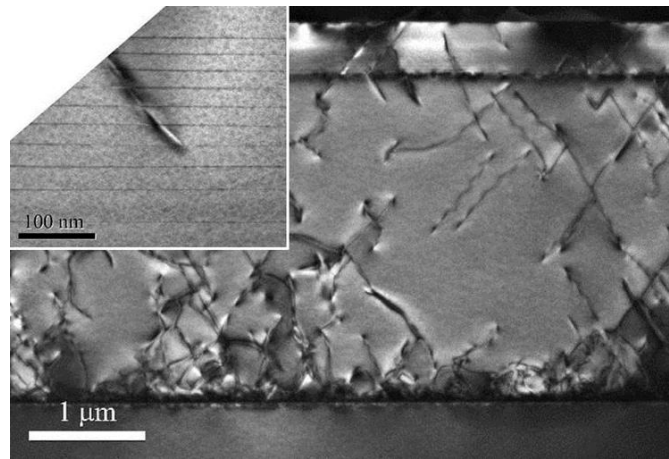
(a)
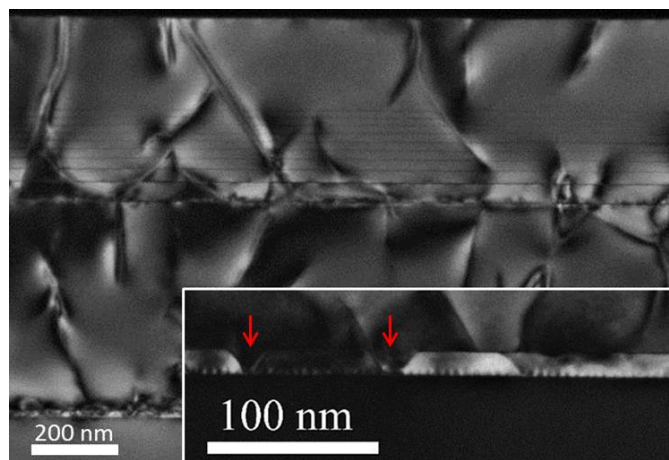
(b)
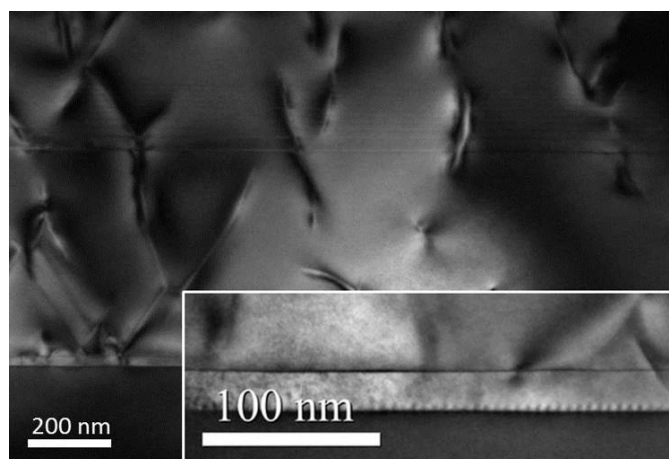
(c)

Fig. 5.2 Cross-section, dark field 002 TEM images of (a): sample (A), (b): sample (B) and (c): sample (C). The inset in (a) is a high magnification TEM image of the InSb QD region in sample (A). The insets in (b) and (c) show the details of the AlSb and GaSb interlayers in these two samples respectively.

Figs. 5.2b and 5.2c show the cross-section TEM images of sample (B) and sample (C) respectively, with the insets giving details of the interlayers. From Fig. 5.2b the IMF periods are visible at the AlSb/GaAs interface, with a measured period of about 5.7 nm. A smooth surface can be formed at the top of the AlSb interlayer and there is no large density of dislocations observed within the AlSb region from the TEM image. Under these growth conditions, self-organized trenches with non-uniform spacing were automatically formed in the AlSb layer, with a 55° {111} side wall angle to the substrate surface, as specified by the red arrows in Fig. 5.2b. In sample (C), the IMF features at the GaSb/GaAs interface with a measured period of about 5.9 nm can also be observed. The IMF periods in both samples are very close to those reported earlier [144][145]. Unlike sample (B), a continuous GaSb layer can be formed on GaAs and the density of dislocations can be effectively reduced within the GaSb layer. However, when depositing the InAs buffer on top of either AlSb or GaSb, new dislocations are once again generated, as shown in figures 5.2(b) and 5.2(c). The TEM images also indicate that the dislocation densities both near the interface and in the QD region are very similar between samples (B) and (C). From these two TEM images we cannot reliably determine which interlayer is more helpful in suppressing the threading dislocations. However, when comparing images in Figs. 5.2a, 5.2b and 5.2c, the lowest density of dislocations in the QD region still occurs in sample (A). The dislocation densities at different parts of the samples were estimated by counting the number of dislocation lines. The values obtained in this way are listed in Table 5.1. In a very similar manner to sample (A), the variation of the QD layer spacing and additional dislocations arising from the bottom QD layers was also observed in samples (B) and (C).

Dislocation density (cm^{-2})	200nm above GaAs	at QDs region
Sample (A)	3 x10^9	4 x10^8
Sample (B)	3 x10^9	2 x10^9
Sample (C)	3 x10^9	2 x10^9

Table 5.1 Estimation of the density of threading dislocations at different regions of samples (A), (B) and (C) obtained by counting dislocation lines from the cross-sectional TEM images.

5.4 X-ray diffraction

Fig. 5.3a–c show the ω-2θ XRD scan of samples (A), (B) and (C), with the XRD spectrum of a reference sample of 10 layers of QDs grown on InAs substrate (sample (D)) as shown in Fig. 5.3d. Two major peaks, one from the GaAs substrate and the other from the InAs MBL layer, both exist in all samples. Although the InAs buffer layers have different thicknesses, the position of the InAs peak is almost the same in each case, which confirms that the strain originating at the interface is almost 100% relaxed in all the samples. The ω-scans of the InAs peaks from samples (A), (B) and (C) are also given in Fig. 5.3e. Because of the thick InAs layer in sample (A), the intensity of the InAs peak in XRD is about five times stronger than from the other two samples. The measured FWHM of the InAs peak in sample (A) (236 arcsec), is also significantly smaller than that in sample (B) and sample (C) (483 and 416 arcsec respectively). This indicates that the InAs buffer layer in sample (A) has achieved smaller crystalline mosaicity than the other two samples [146], where the higher density of threading dislocations can affect the InAs layer growth more seriously. We can also notice weak fluctuations on both sides of the InAs peak in sample (A), which probably originate from the QD layers. In a similar manner to multiple quantum wells (MQWs) [147], the multiple QD layers in our samples would be expected to give periodic peaks on both sides of the InAs peak, as the XRD spectrum of sample (D) shows. However, due to the changing

thickness of InAs spacer layers between the InSb QD layers, such periodic features cannot be clearly observed from sample (A), and are absent from samples (B) and (C). In sample (C), a clear peak appears on the left side of the InAs peak which we attribute to the GaSb interlayer. In sample (B) the AlSb interlayer only results in a wide tail, which is probably because of its discontinuous nature.
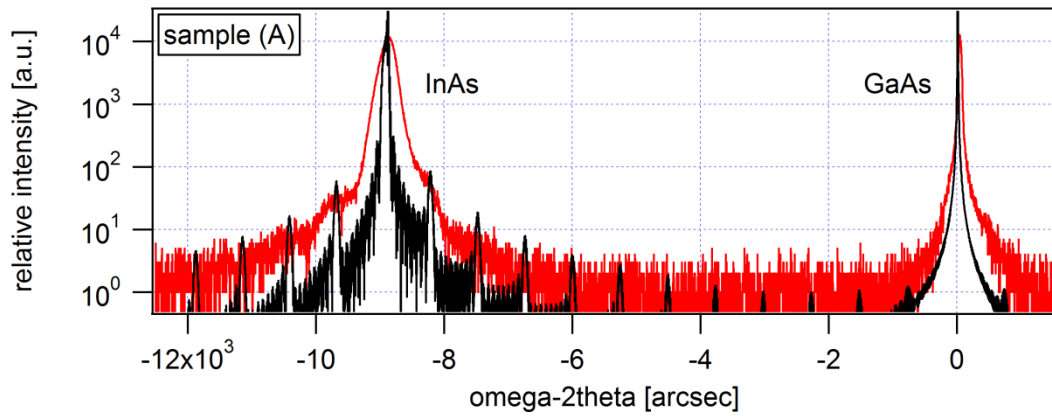
(a)
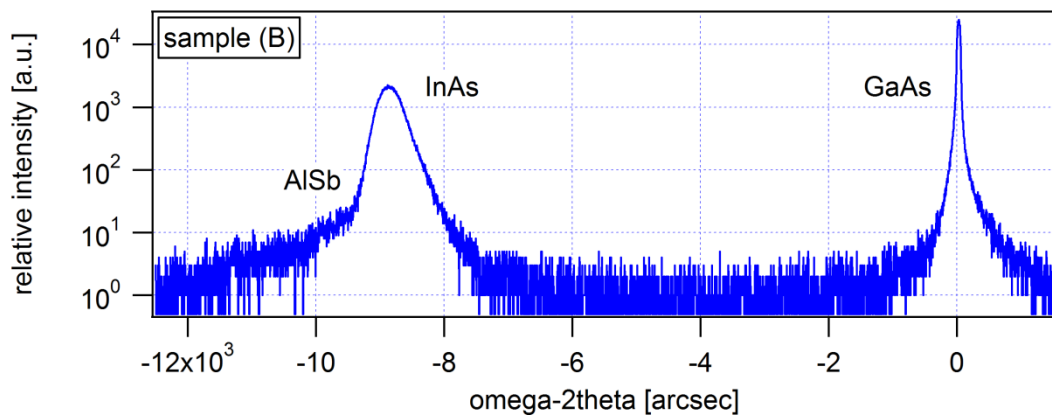
(b)
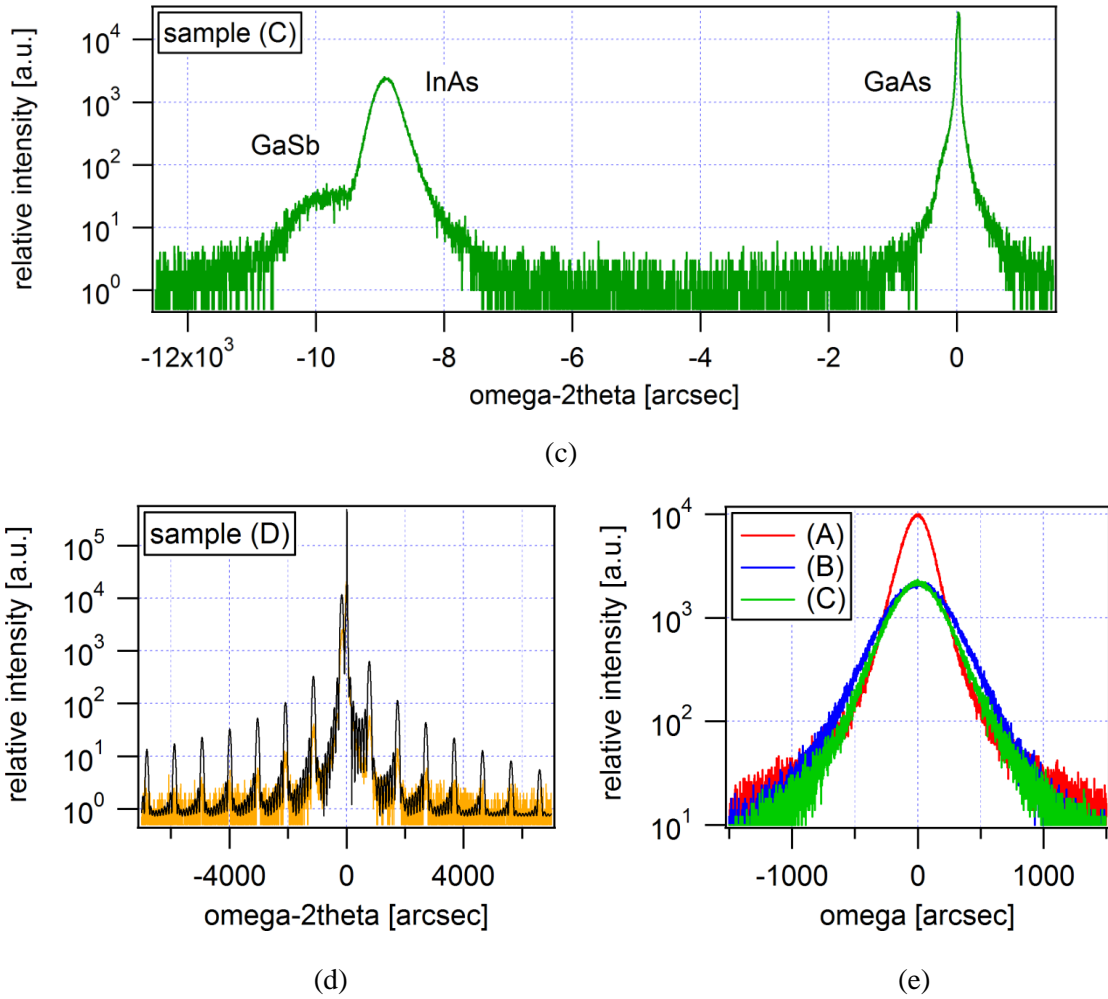
Fig. 5.3 (a): ω-2θ XRD spectrum of sample (A), the expected periodic side peaks from the QD layers are illustrated by the black curve. (b): ω-2θ XRD spectrum of sample (B), the stronger tail on the left side shoulder of the InAs peak is from the discontinued AlSb interlayer. (c): ω-2θ XRD spectrum of sample (C), the weaker peak on the left side shoulder of the InAs peak is from the GaSb interlayer. (d): ω-2θ XRD spectrum of sample (D), the side peaks are fitted by a MQW model (black curve). (e): The ω-scans of the InAs peak in samples (A), (B) and (C).

5.5 Photoluminescence

The PL from the InSb QDs grown on top of the InAs MBL can help give an indication about the quality of the surrounding InAs. Previous work has shown that the density of InSb QDs grown using the exchange technique on InAs results in a high QD density of $\sim 10^{12}$ cm^{-2} [148]. PL spectra measured from the three samples at 4 K using an excitation laser power of 10 W/cm^2 are shown in Fig. 5.4, together with the PL spectra from sample (D), which is from the InSb QDs grown on homoepitaxial InAs under optimized QD growth conditions. In all the

measured samples, both the dominant peaks from the InSb QDs and the emission from bulk InAs can be observed. The much higher relative PL intensity from the QDs than from the InAs in each of the three samples is an indication of successful growth of high density QDs using all the three metamorphic techniques. The inset of Fig. 5.4 shows the magnified PL spectra between 2.9 μm and 3.3 μm of the samples when excited with a lower laser power (1 W/cm^2) at 4 K, in which different recombination mechanisms in InAs can be more clearly revealed. Besides the peak at around 2.98 μm (peak 1) from band-to-band transitions, there is a peak at 3.1 μm (peak 2) in all samples except sample (C), which originates from bound exciton transitions and has been previously observed in the low temperature PL of InAs epilayers grown on GaAs [149][23]. According to [23], the absence of bound exciton transitions can be correlated with poor luminescence efficiency of the InAs epilayer, which in our case indicates the InAs layer in sample (C) is not of equally good quality as in samples (A) and (B). In addition, another peak near 3.25 μm (peak 3) can be observed in the spectrum of sample (A) only. Its transition energy (382 meV) agrees well with the donor-acceptor pair (DAP) recombination in InAs grown on GaAs [149][23]. It is still possible that DAP recombination is also taking place in other samples, but it cannot be clearly resolved since it lies very close to the much stronger QDs emission in these samples.
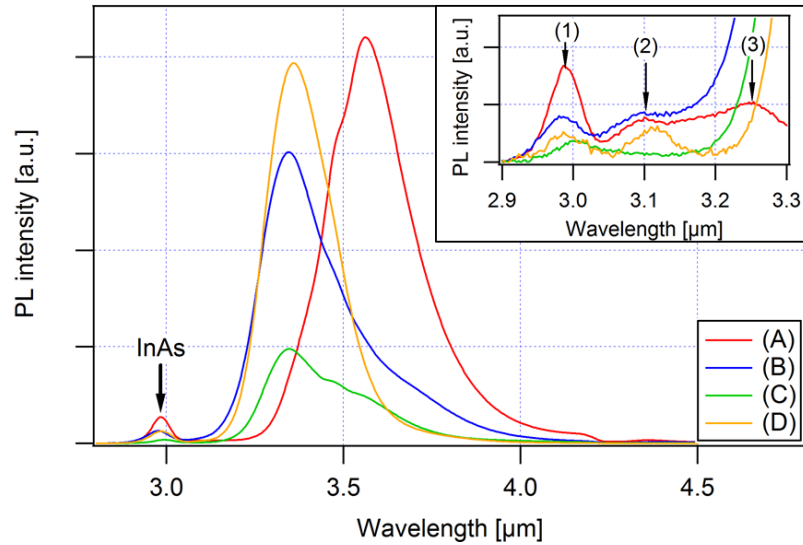
Fig. 5.4 PL spectra of samples (A) (red line), (B) (blue line), (C) (green line) and the reference sample (D) (yellow line) measured at 4 K using an excitation intensity of 10 W/cm^{2}. PL emission from the InAs matrix is also be observed from all samples. The inset shows magnified spectra of the InAs emission originating from different recombination mechanisms in all the samples at 4 K using an excitation intensity of 1 W/cm^{2}.

Comparing the InSb QDs PL spectra between samples (A) and (D), we find that both PL peaks are approximately Gaussian, originating from the size distribution of the QDs. The QDs in sample (A) also achieved similar PL peak intensity to that of the QDs grown on homoepitaxial InAs (sample (D)). The change in PL peak position between these two samples (from 3.56 µm to 3.36 µm respectively) results from differences in growth conditions which affect the dimensions and size distribution of the resulting QDs [93]. The linewidth of the QD PL peak in sample (A) is 270 nm which is only slightly larger than that of 223 nm in sample (D). These observations indicate that, (i) the density and size distribution of QDs is very similar in samples (A) and (D), (ii) although the density of dislocations in the vicinity of the QDs in sample (A) as seen from TEM images remains high, it has no significant effect on the PL of the QDs. This is probably not surprising since the QD density is a few orders of magnitude higher than the dislocation density. As shown in Fig. 5.4 the QDs PL spectra from samples (B) and (C) both have significantly stronger tails on the longer wavelength side and the peak positions have shifted to around 3.36 µm, even though the QDs were grown under

nominally the same conditions as sample (A). As demonstrated in [93], the growth conditions strongly determine the resulting QD size, shape and density. The much thicker InAs buffer layer in sample (A) can still make a difference to the heat transfer on the sample surface when the QDs were being grown, making the actual surface temperature slightly different for sample (A) compared with the other two samples during the QD growth. This can result in a significant change of PL peak position and intensity, which explains the differences in peak wavelength between sample (A) and samples (B), (C). The PL peak intensity from sample (B) is still higher than sample (C), and the PL spectrum tail is weaker. We can suppose that a higher density of QDs with better size uniformity have been grown in sample (B) than in sample (C), which also indicates the AlSb interlayer is more helpful than the GaSb interlayer for the subsequent growth of good quality InAs. However, the PL intensities from these two samples are still weaker than in sample (A). We believe that is because the top of the 0.5 μm thick InAs buffer above the (AlSb or GaSb) interlayer growth cannot yet serve as an equally good pseudo-substrate for growth of high quality InSb QDs under the same growth conditions.
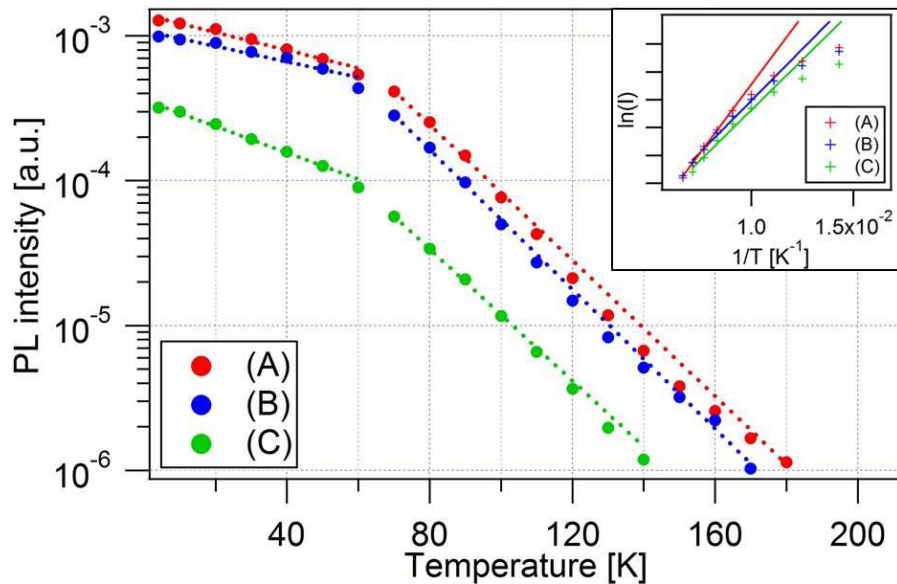
Fig. 5.5 Integrated QD PL intensities from samples (A), (B) and (C) at different temperatures. The dotted lines show the exponential fit of PL intensity with temperatures below 60 K, and the dashed lines show the exponential fit for temperatures above 60 K. The inset shows the relation between the logarithm of integrated PL intensity from QDs (ln(I)) and the reciprocal temperature (1/T) from which the activation energy can be extracted. The straight lines give the linear fit in the low 1/T region.

The QDs PL from samples (A), (B) and (C) can be measured up to 180 K, 170 K and 140 K respectively. The integrated PL intensities at different temperatures are plotted in Fig. 5.5 which shows that for all the samples investigated the PL quenching with increasing temperature accelerates significantly above 60 K consistent with thermal escape of confined holes from the QDs [150][151]. The thermal activation energy can be calculated from an Arrhenius plot, as shown in the inset of Fig. 5.5. The activation energies of 80 meV, 64 meV and 62 meV for samples (A), (B) and (C) are approximately in agreement with the heavy hole confinement energies obtained from k.p modelling . The higher activation energy in sample (A) corresponds to QDs having deeper hole confinement, which is consistent with a longer wavelength PL peak emission associated with formation of larger QDs. The difference in corresponding transition energies for (B) and (C) is also consistent with their reduced thermal activation energies. Details are given in table 5.2.

sample	QD PL peak			activation energy (meV)	heavy hole confinement energy (meV)
	PL peak energy (meV)	wavelength (μm)	FWHM (nm)		
A	349	3.56	270	80	71
B	369	3.36	255	64	49
C	369	3.36	305	62	47

Table 5.2 Summary of the QD PL emission results and activation energies from samples (A), (B) and (C).

5.6 Electroluminescence
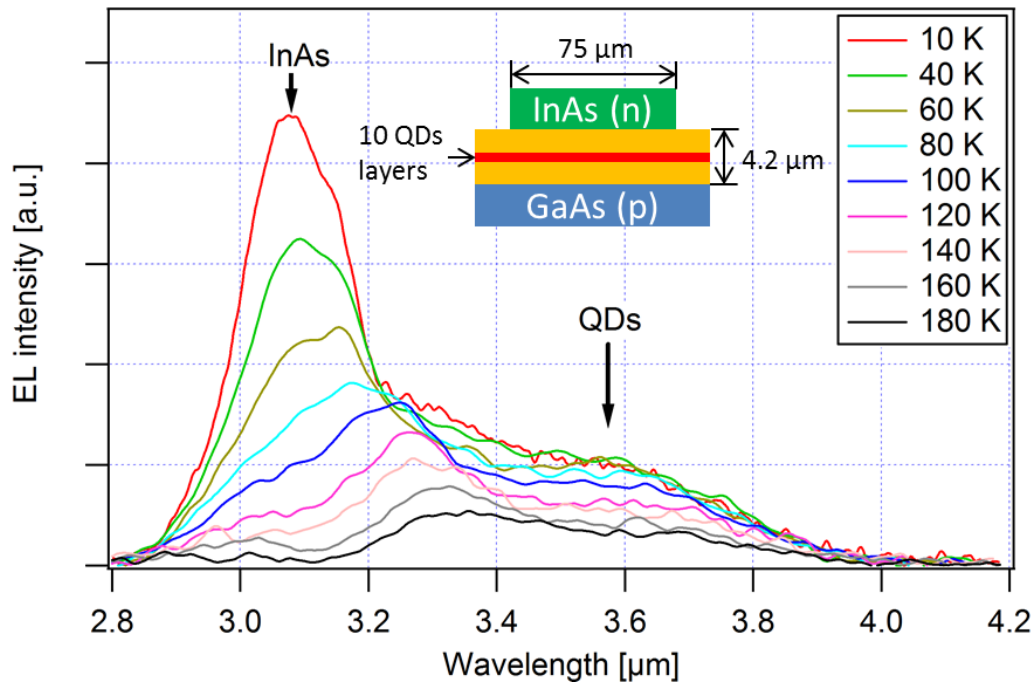
Fig. 5.6 EL spectra from the p-i-n diode structure containing 10 layers of QDs, measured from 10 K to 180 K, with a 20 kHz pulsed current of 1.0 A at 1% duty cycle. The inset illustrates the structure of the p-i-n diode.

The highest PL intensity was obtained from QDs with a thick InAs buffer (sample (A)) and so as shown in Fig. 5.6, edge-emitting p-i-n LEDs containing ten layers of QDs in the (i-) active region were grown by MBE on a p-doped ($\sim2\text{x}10^{18}$ cm^{-3}) GaAs substrate with the direct metamorphic deposition of InAs (as in (A) above). The intrinsic region was composed of a 4 µm thick InAs layer containing the ten sub-monolayer insertions of InSb QD layers in the middle, each with a 20 nm spacing. The upper layer consisted of a 2 µm thick n-doped ($\sim2\text{x}10^{18}$ cm^{-3}) InAs layer. EL emission was extracted from the 75 µm wide edge of the 1 mm long ridge structure using 1 A current pulsed excitation (20 kHz, 1% duty cycle). The measured spectra from 10 K up to 180 K are shown in Fig. 5.6, with the inset illustrating the diode structure. The highest peak at 3.07 µm at 10 K originates from recombination in the InAs, while the broader emission at longer wavelengths is from the InSb QDs. Contrary to the PL results, the EL from the InAs layer is always stronger than the EL from QDs. During the

106

EL measurement, higher densities of electron-hole pairs are injected to the sample than in the PL measurement so that an overflow of carriers into the InAs can occur, resulting in more overall emission from the InAs. The temperature dependence of integrated EL intensities for both the InAs and the InSb QDs is illustrated in Fig. 5.7. The EL of the InSb QDs is insensitive to temperature below ~ 60 K and quenches more slowly than the PL of the InAs, which is dominated by non-radiative Auger recombination. In EL, the injected carrier density is much higher than in PL and holes are constantly being provided into the QDs by the applied electric field. This reduces the net rate of escape of holes out of the QDs and helps to maintain the EL emission intensity. Consequently, the decay of the InSb QD EL emission is less rapid with increasing temperature than in PL. These results are in good agreement with our earlier findings from InSb QD LEDs grown on InAs substrates which exhibited EL at room temperature with the addition of an $Al_{0.9}Ga_{0.1}As_{0.15}Sb_{0.85}$ electron blocking layer [10]. The EL from the QDs in the present structures does not persist up to room temperature partly for this reason.
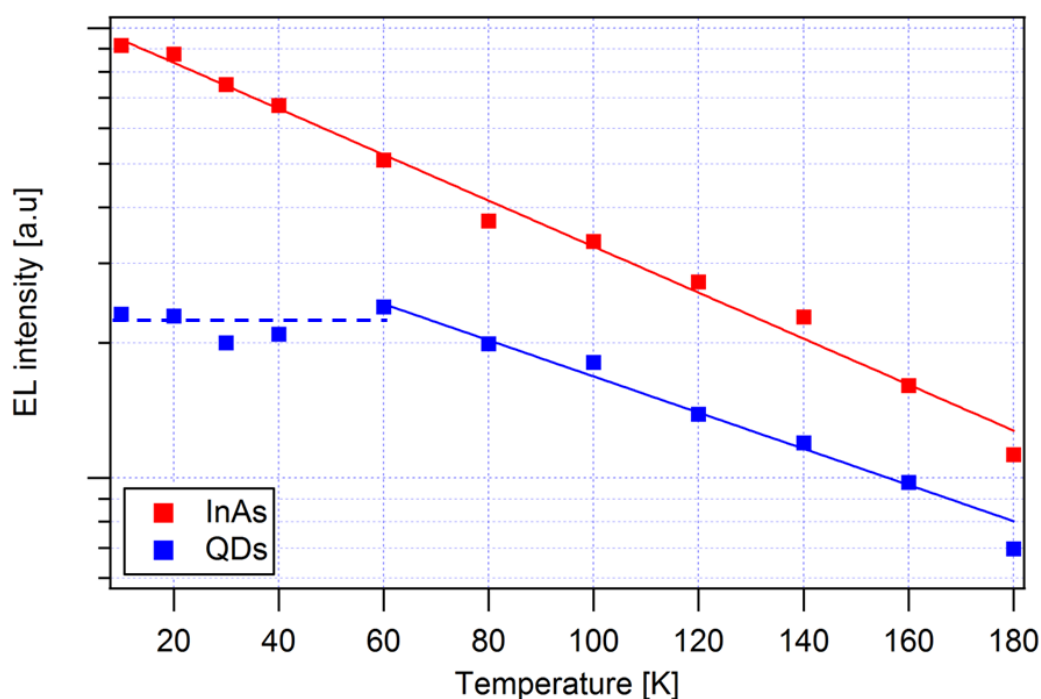
Figure 5.7 Temperature dependence of EL intensity from InAs (red squares) and QDs (blue squares). The straight lines show the exponential fit of the InAs EL from 4 K to 180 K and QDs EL from 60 K to 180 K.

5.7 Conclusions

In order to incorporate InSb QDs on GaAs substrates, we have experimented with the direct metamorphic growth of a thick InAs buffer layer, and the insertion of AlSb or GaSb interlayers with thinner InAs buffer layers, to accommodate the strain caused by the large lattice mismatch. In all samples, the QDs were grown on top of the resulting InAs buffer layers. Cross-section TEM images showed that the density of threading dislocations in the QDs region grown on a thick InAs buffer is lower than in the other two samples grown using interlayer techniques. The TEM images revealed that IMF misfit arrays are formed at both AlSb/GaAs and GaSb/GaAs interfaces. In addition, self-assembled trenches can be formed in the AlSb layer.

The 4 K PL intensity and linewidth from InSb QDs grown with direct metamorphic deposition of a thick InAs buffer are very close to that of InSb QDs grown homoepitaxially on InAs substrate, even though the threading dislocation density is still high. This is because the QD density is a few orders of magnitude higher than the dislocation density. The top surface of the thick InAs buffer is of a sufficiently good quality to serve as a pseudo-substrate for the QDs growth, and the carrier recombination within the QDs is not sensitive to the existence of a high density of threading dislocations due to the carrier confinement. However, as temperature increases and holes become thermally excited out of the InSb QDs the quality of the surrounding InAs becomes more significant since non-radiative Shockley-Read-Hall recombination influences the re-capture rate of holes. Consequently, further optimization of the MBL layer would be beneficial in achieving room temperature mid-infrared EL from InSb QDs in InAs grown on GaAs substrates. The XRD measurements confirmed that the thick InAs buffer has better crystallinity than the InAs grown on interlayers. In order to reduce the thickness of the InAs buffer layer, the use of an AlSb interlayer appears to be a better choice than the GaSb interlayer. Finally, prototype p-i-n diodes containing InSb QDs were made

using direct growth of a thick InAs buffer, and mid-infrared EL at 3.6 μm was obtained from

InSb QDs in non-optimized edge emitting LED structures up to 180 K.

6. Properties of InSb quantum dots

6.1 Introduction

In this chapter, the QD PL characteristics are discussed in more detail. With the help of the STEM images and the calculation of transition energies using COMSOL multiphysics, the PL spectra were used to interpret the size and composition of the QDs. The dot-to-dot carrier transfer was linked to the temperature dependence of PL peak positions and compared with the COMSOL calculation results. Modification of the QD structure by growing on InP substrate is also presented.

6.2 QD size and composition

From the TEM images in Figs. 3.9 and 5.2, we can only see the InSb QD layers. Due to their extremely small size and resolution limit, the exact size and geometry of individual QDs cannot be determined from these pictures. Bright field scanning transmission electron microscopy (STEM) was used to focus on one single QD. The image is shown in Fig. 6.1, in which the red colour represents the concentration of Sb. Previous 6x6 k.p calculations for this type of QDs suggested that the emission wavelengths were not sensitive to the exact shape of the QDs [98]. So it was approximated that the QD is in a a conical shape, 2.5-3 nm in base radius and 2-3 nm in height. However, this STEM image cannot give indication about the composition of the QD, nor whether the material is uniform within such a small structure. The Sb segregation in the QD layer and in the InAs spacer regions between layers can also be observed.
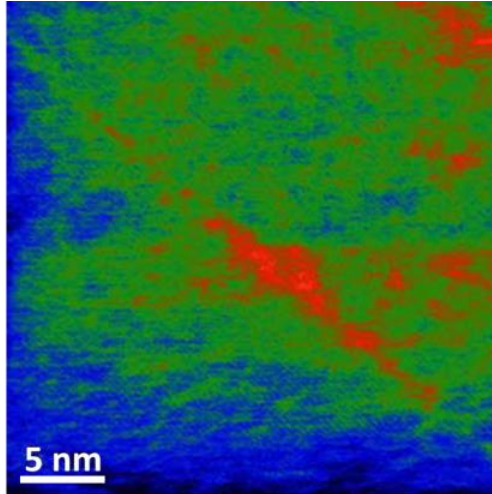
Fig. 6.1 Bright field STEM image, magnification 2MX, obtained from Sheffield University. The picture shows an individual sub-monolayer InSb QD in cross-section using an inverted false colour map, where the red colour represents the concentration of Sb.

From previous chapters, the peak emission wavelength of the InSb QDs typically falls between 3.2 and 3.8 μm at low temperature, corresponding to transition energies between 0.326 and 0.388 eV. The dependence of pure InSb QD transition energies on the radius and height of the QDs at 4 K were calculated using COMSOL multiphysics, and plotted in Fig. 6.2a. The values of band gap, electron affinity and electron/hole effective mass were taken from [18].
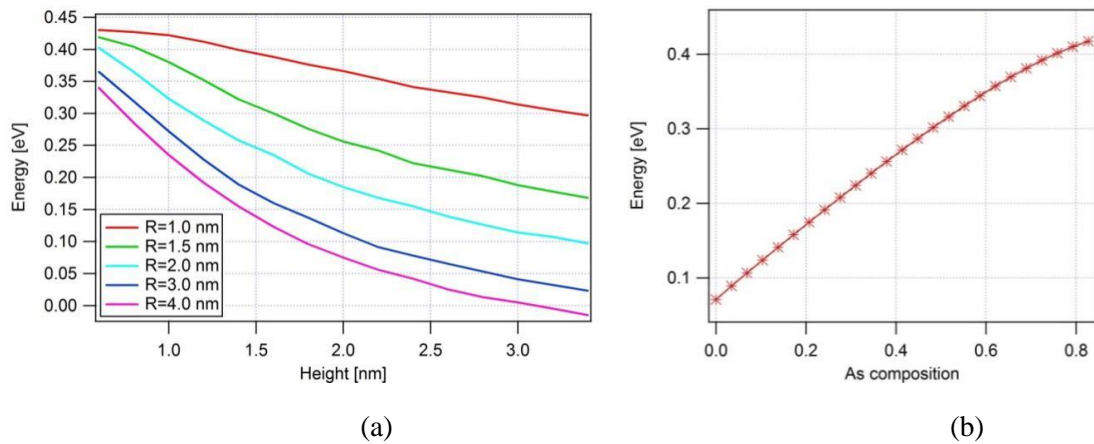
(a)   (b)

Fig. 6.2 (a) Calculated transition energy of InSb QD as a function of the QD height for different radius values at 4 K. (b) Calculated transition energy of $InAs_xSb_{1-x}$ QD as a function of As composition at 4 K, where the QD size is fixed at 3 nm base radius and 2 nm height.

The transition energy exhibited strong dependence on the QD size. For example, with a fixed radius of 2 nm, the 0.5 nm change in QD height (from 1.5 nm to 2 nm) resulted in about 70

111

meV difference in transition energy. The COMSOL calculation solves the Schrodinger equation in 3D space with predefined band offsets and carrier effective masses, without taking into account any strain effect, band-bending or Coulomb forces. Although it is a much simpler estimation than the k.p calculations, the values obtained here are in fact in good agreement with the results from 6x6 k.p calculations [98], in which the radius of the QDs were fixed at 1.25 nm in the simulation. Assuming the QD was composed of pure InSb, it was found from both k.p modelling from [98] and COMSOL calculation from Fig.6.2a that, to achieve a typical transition energy of 0.35 eV, the QD height needed to be about 1.0 nm and radius 1.25-1.5 nm. This calculated size cannot agree with the observations from Fig. 6.1. The most possible reason for this disagreement is that instead of pure InSb, the QDs may contain a larger proportion of As. By fixing the QD size according to Fig. 6.1 (3 nm in base radius and 2.5 nm in height), the transition energy dependence on the composition of As was also calculated by the same method in COMSOL and plotted in Fig. 6.2b. To obtain the 0.35 eV transition energy, the QD composition would be close to $InAs_{0.6}Sb_{0.4}$. In this case, the band alignment maintains to be type II, but is no longer broken band alignment as for pure InSb QDs. It needs to be noted that one STEM image cannot represent all of the QDs in the structure. And it is most likely that there are deviations in both QD size and composition. So both QDs with pure InSb in an extremely small size or larger QDs with more As in the composition can exist in the same sample.

6.3 Energy states

In type II InSb QDs, only holes are confined within the QDs. From the study of PL and EL spectra alone, we still cannot obtain directly how many quantized states exist in this kind of QDs. By using the same COMSOL calculation, assuming the size of 3 nm base radius and 2.5 nm height and composition as $InAs_{0.6}Sb_{0.4}$, it was found that only the ground heavy hole (GHH) state was confined within the QD, with a confinement energy of about 60 meV. The

heavy hole excited states and light hole energy states were in the continuum out of the QDs, which implies there should be no hidden multiple peaks within the PL spectra, and the width of the PL peak then corresponds to the size distribution of the QDs. From the GHH wave function distribution, we can also calculate the hole confinement factor in the QD to be 64%. The energy states calculations for pure InSb in a smaller size were performed using 6x6 k.p method [98], which also indicated in that case there was only the GHH state confined within the QDs. In that case, the confinement factor was about 60%.
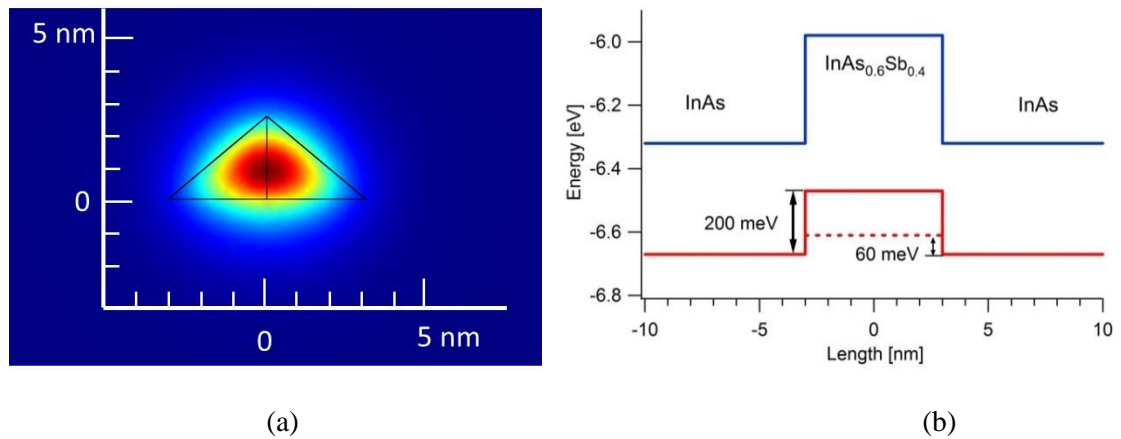
(a)   (b)

Fig. 6.3 (a) Simulated GHH state wave function probability distribution in a single InAs$_{0.6}$Sb$_{0.4}$ QD assuming a conical shape. (b) Conduction (blue) and valence (red) bands of the InAs$_{0.6}$Sb$_{0.4}$ QD, the dotted red line signifies the calculated position of the GHH state.

6.4 Temperature dependent PL

The temperature dependent PL spectra of several QD samples were measured. The examples of PL spectra measured at 4 K, 40 K and 80 K from one of the QDs samples are presented in Fig. 6.4a. It was first expected that the PL peak would move to longer wavelengths due to band gap shrinkage with increasing temperature. However, it was observed that the PL spectra from our QDs typically had a slight blue shift followed by a significant red shift when the temperature was increased. The PL peak dependence on temperature is shown in Fig. 6.4b, in which at around 40 K, the PL peak reached the shortest wavelength. This characteristic was also reported by Lyublinskaya et al. [152], who proposed that it originated from the free transfer of carriers between QDs. The explanation is illustrated in Fig. 6.4c. In their work, the

QDs showed a Gaussian distribution in lateral size, resulting in a corresponding Gaussian distribution in the density of states. The carrier distribution within the QDs should follow the temperature dependent Fermi-Dirac function if the movement of holes between QDs is not inhibited, so that the PL shape *q(E)* would be decided by the product of these two functions:

$$q(E) \sim \frac{exp\left\{-\left[(E - E_0)/\sqrt{2}w\right]^2\right\}}{1 + exp[(E - E_F)/kT]} \tag{6.1}$$

where *E* is the photon energy, E_0 and *w* the peak position and width of the Gaussian function, and E_F the quasi Fermi energy in the Fermi-Dirac function which is dependent on the excited/injected carrier densities, *T* the temperature and *k* the Boltzmann constant. Assuming the QDs grown in our work also have Gaussian size distribution as in [152], this equation can be applied to estimate the PL peak positions at different temperatures, which makes a good fit to the measured data of PL peak shift (blue curve in Fig. 6.4b).
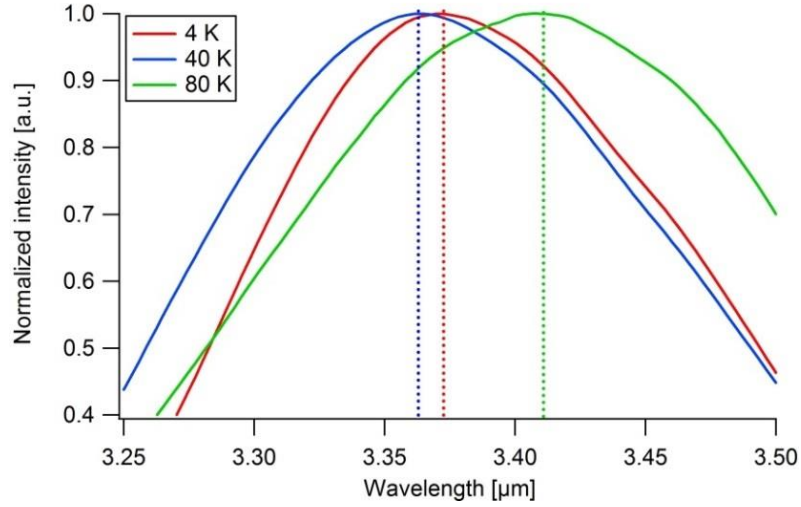
(a)
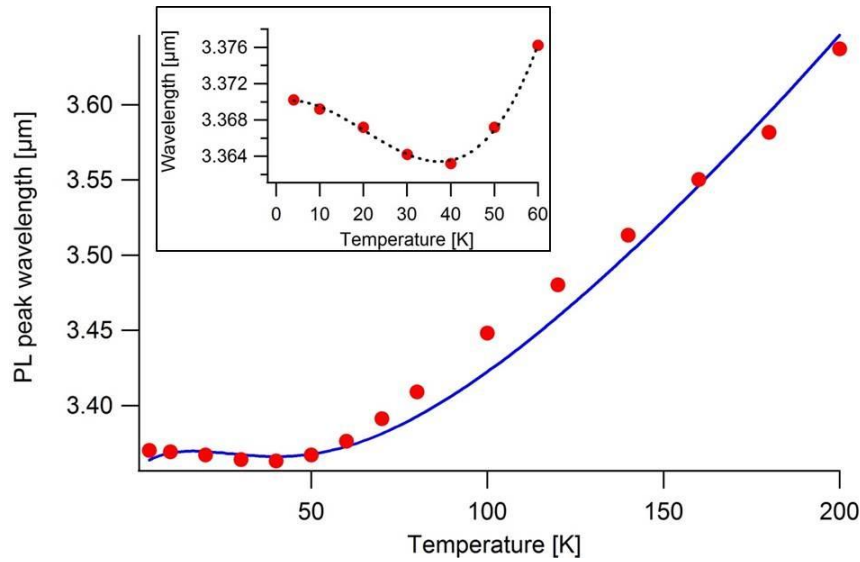
(b)
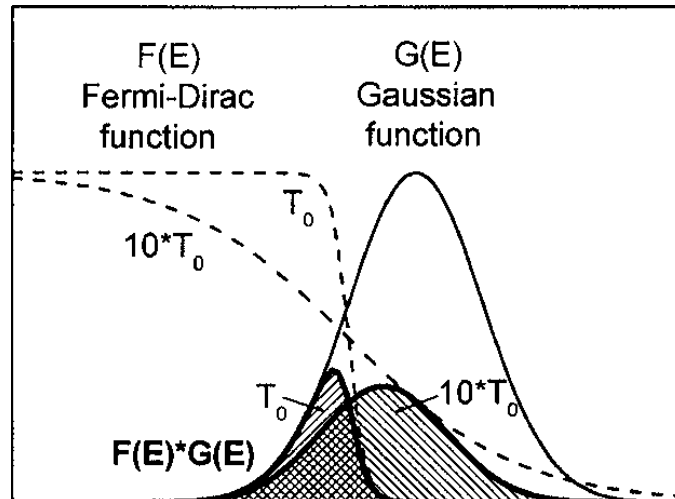
(c)

Fig. 6.4 (a) Normalized QD PL spectra measured at 4 K (red curve), 40 K(blue curve) and 80 K (green curve). The dotted lines signify the PL peak positions. (b) (Red dots) measured PL peak wavelengths at different temperatures. The data was fitted by the proposed model (blue curve). The inset magnifies the 0-60 K region, showing the slight blue shift below 40 K, and large red shift above 40 K. The dotted line is only for guidance. (c) Product (bold line) of Fermi-Dirac (dashes) and Gaussian distribution (solid line) functions at different temperatures [152].

Type II nanostructures typically have longer radiative lifetime due to the spatial separation of electrons and holes [153], making the carrier relaxation before recombination very probable. There are two possible mechanisms that can contribute to the free movement of carriers between QDs. Firstly, the holes trapped in the QDs can be thermally excited out and re-trapped by adjacent QDs. Secondly, the tunneling probability of confined holes will increase

115

with decreasing distance between adjacent QDs. The thermal excitation of carriers out of QDs has been examined in Chapter 5, where it was indicated that this effect only became significant when the thermal energy exceeded the offset between InAs valence band and the hole energy level (i.e. T > 50 K). So at lower temperatures, the migration of holes between QDs has to mainly rely on the tunneling effect. With a high QD density of ~10^{12} cm^{-2}, the average distance between adjacent QDs is no larger than 4 nm, making the tunneling process very likely to happen.

6.5 QD structure modification.

In Chapter 5, we identified the thermal excitation of holes out of the QDs as a major loss mechanism at higher temperatures. One method to reduce the thermal leakage is to insert a blocking barrier using a material with a higher valence band offset between the QDs. A modified InAsSb QD structure was designed on InP substrate with an InAs$_{0.65}$P$_{0.35}$ step buffer layer and In$_{0.84}$Ga$_{0.16}$As barrier layers, as shown in Fig. 6.5a. This structure also provides the potential for integration of mid-infrared QD light sources with the more mature InP based devices and structures, offering a wide range of application possibilities. The metamorphic layer of InAs$_{0.65}$P$_{0.35}$ on InP was grown in the Walter Schottky institute. The InAs$_{0.65}$P$_{0.35}$ and In$_{0.84}$Ga$_{0.16}$As are almost lattice matched, so the In$_{0.84}$Ga$_{0.16}$As barrier can be assumed to be totally unstrained. During the growth of the QDs, a very thin (<1 nm) layer of InAs was first deposited on In$_{0.84}$Ga$_{0.16}$As to enable the exchange reaction for the QD formation. The same method as on InAs was used to grow the QDs. After the deposition of InSb, 4 nm thick InAs was deposited to cover the QDs, although a large part of it might fill into the space between QDs, forming a dot-in-well (DWELL) structure. 4 periods of DWELL layers were grown with 20 nm In$_{0.84}$Ga$_{0.16}$As spacer layers in between. The valence and conduction band alignments are sketched in Fig. 6.5b, along with the band gaps of InP, InAs$_{0.65}$P$_{0.35}$ and In$_{0.84}$Ga$_{0.16}$As. Assuming the QDs have the same composition as grown on the InAs substrate (InAs$_{0.6}$Sb$_{0.4}$), the valence band offset becomes increased from ~200 meV in Fig. 6.3b to 280 meV. Due to

the strain effect, the conduction band of the InAs well is almost the same as the $In_{0.84}Ga_{0.16}As$ layer (~15 meV higher). The details of the valence band in the DWELL structure are shown in Fig. 6.5c. From COMSOL calculations, same as in the QDs on InAs, only GHH state (solid black line) is confined within the QD. The InAs QW provides two heavy hole energy levels (dashed green lines) and one light hole energy level (dashed purple line) within the DWELL structure.
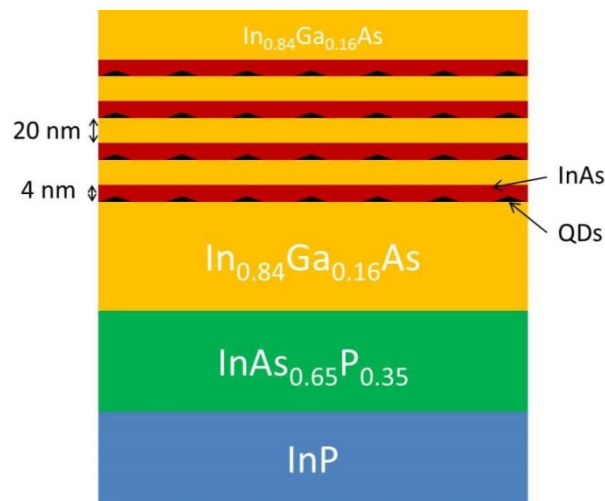
(a)
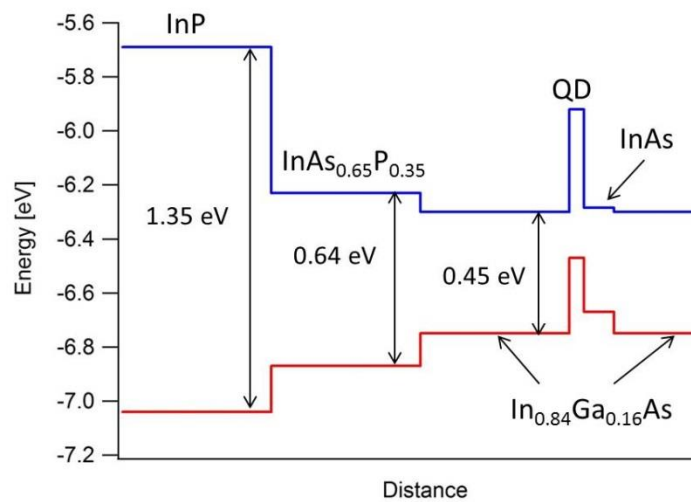
(b)
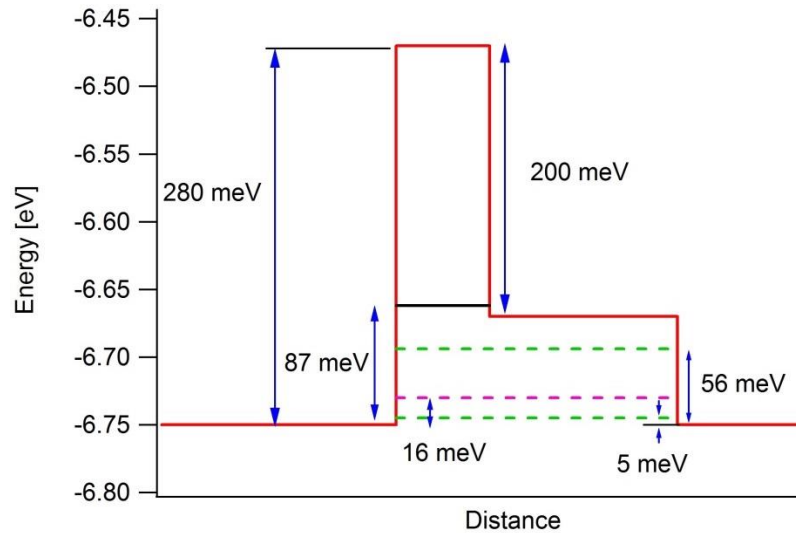
(c)

Fig. 6.5 (a) Illustration of the DWELL sample grown on InP substrate. (b) Sketch of the conduction (blue line) and valence (red line) band diagrams of the DWELL structure. The band gaps of InP, InAs$_{0.65}$P$_{0.35}$ and In$_{0.84}$Ga$_{0.16}$As are also presented. (c) Valence band alignment in the DWELL, along with the calculated QD energy state (black line),confined HH energy levels (dashed green lines) and LH energy level (dashed pink line). The values of band offsets and energy differences are also presented in the picture.

Power dependent and temperature dependent PL measurements were performed on the above DWELL sample. The results are shown in Fig. 6.6a below. At 4 K, the PL peak from the QDs was positioned at around 2.7 μm. This is significantly shorter wavelength compared with the typical QDs grown on InAs. One reason for this is the deeper hole confinement of the In$_{0.84}$Ga$_{0.16}$As barrier layers. But the COMSOL calculations also suggested that the QDs grown on In$_{0.84}$Ga$_{0.16}$As needed to be smaller in size (1.6 nm height, 3 nm base radius) so as to have the emission at this wavelength. In order to obtain emission at longer wavelengths in this structure the QDs need to be grown larger in size, which probably can be achieved by reducing the substrate temperature during the growth [93]. In the same way as for the QDs grown on InAs, with increasing laser power, a slight blue shift of the PL peak was observed. (The small dip at ~2.7 μm most likely originates from water vapour absorption in the optical path during the measurements). Another peak at around 2.27 μm was also detected, which originated from the In$_{0.84}$Ga$_{0.16}$As barrier layers. From the power dependent PL spectra at 4 K, broad emission between 2.3 and 2.5 μm can be observed, which is most likely from the energy

118

levels in the QWs. Though it's very difficult to divide it into multiple peaks corresponding to the QW energy levels shown in Fig. 6.5c. The ratios of the PL intensities between peaks A from the barrier, B from the InAs QW and C from the QD in the QW (marked as A, B and C in the picture) are plotted in Fig. 6.6b. With increasing excitation laser power, the A/C ratio increased slightly, which is most probably due to the filling-up of the DWELLs. Similar effect has also been observed in the same type of QDs grown on InAs substrates [154]. Interestingly, the B/C ratio showed a significant decrease. One possible reason is that because of the small energy difference between the excited HH energy level/LH energy level and the valence band, carriers are very likely to escape from the QW and recombine in the barrier region. So the increase of peak B is slower than peaks A or C.
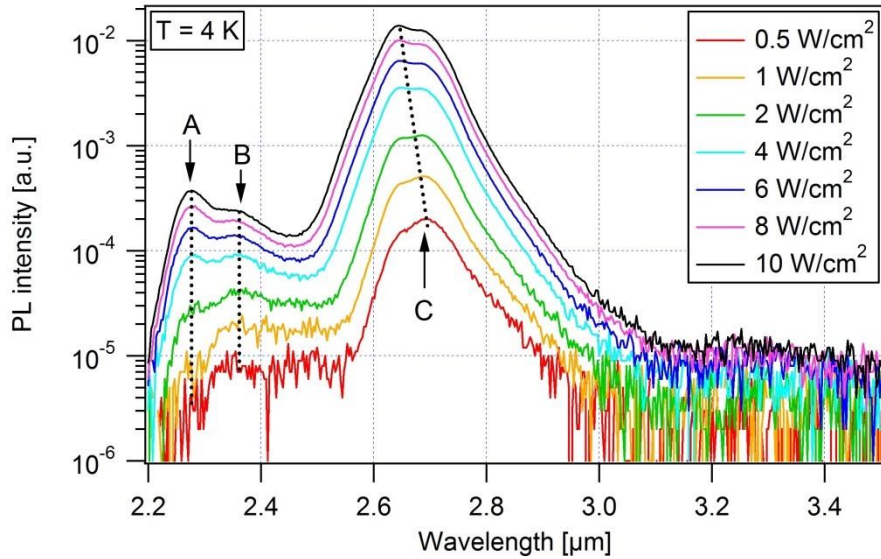
(a)
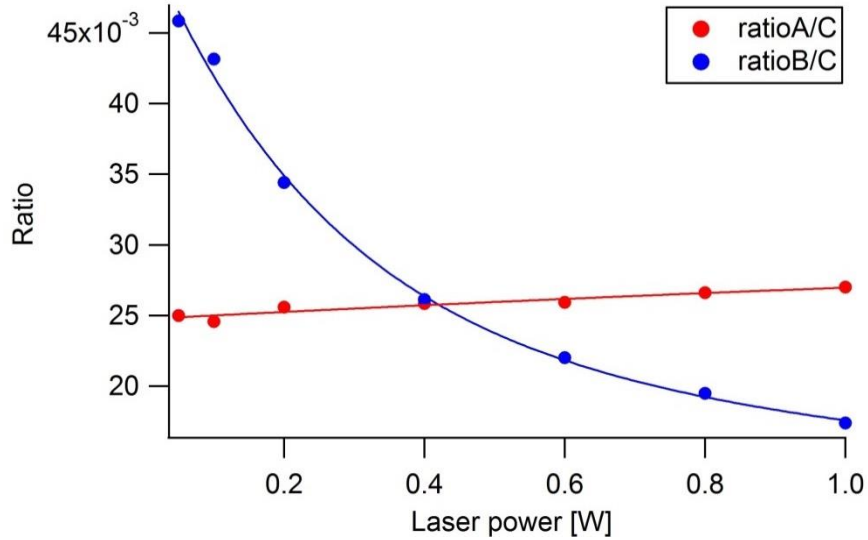
(b)

Fig. 6.6 (a) PL spectra of the DWELL sample measured at 4 K with different excitation laser powers. (b) PL peak intensity ratios between emissions from the barrier and the QDs (A/C), and between emissions from the QWs and QDs (B/C).

PL from the QDs can be detected up to RT, when the peak wavelength was shifted to around 3.05 μm. The measured spectra at different temperatures are plotted in Fig. 6.7a. The QW emission almost disappeared at 50 K and 100 K, the reason why is still unclear. For T > 150 K, the QW emission became broadened and can no longer be distinguished from the barrier emission. The percentage of the PL emission from the QDs at different temperatures is deduced from this graph and plotted in Fig. 6.7b. For T < 100 K, the QD emission maintained

a high percentage (> 90%) of the total PL signal, but for T > 100 K, the percentage drastically decreased to less than 20% at 300 K. It implies that when temperature is higher than 100 K, the confined holes in the QDs are very likely to escape and recombine at the energy levels in the QWs or in the barrier region, probably due to thermal excitation.
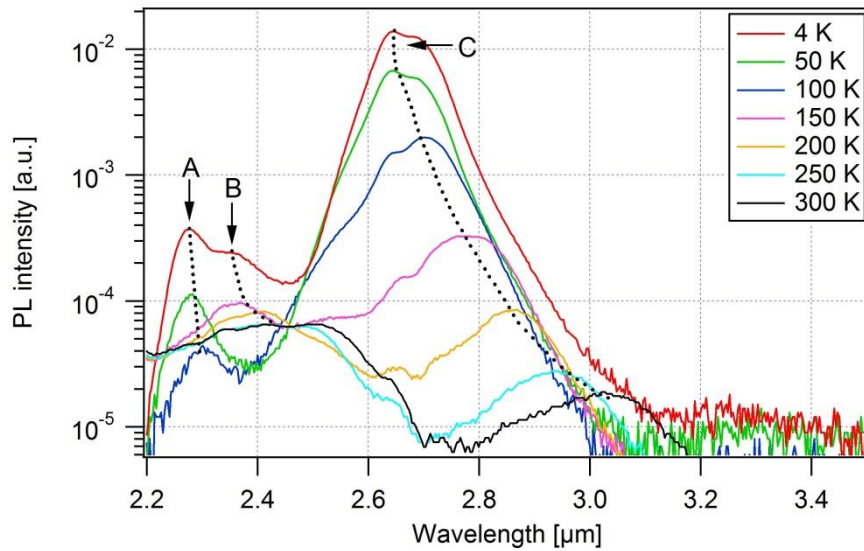
(a)
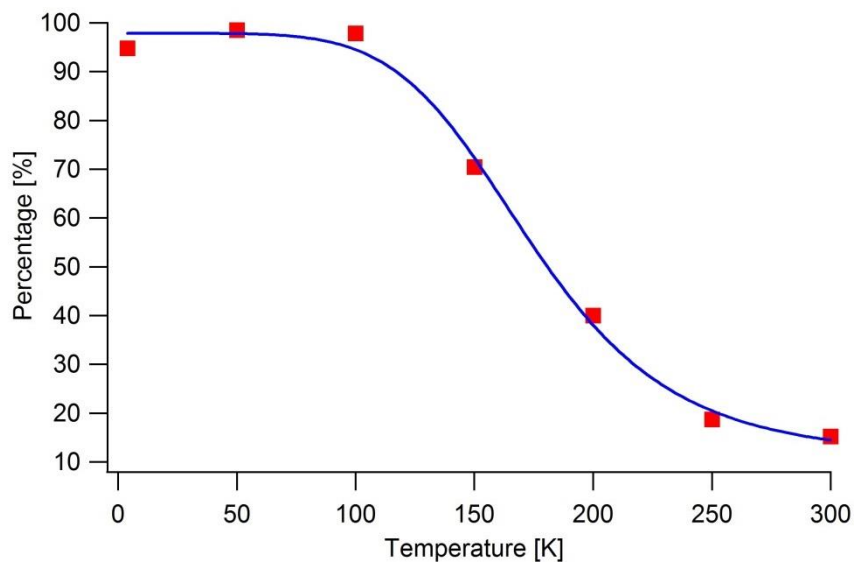
(b)

Fig. 6.7 (a) PL spectra of the DWELL sample measured at different temperatures with the same excitation laser power (1.0 W). (b) Percentage of the PL from the QDs out of the total PL at different temperatures.

Compared with the QDs samples grown on InAs and GaAs, this novel structure shows the advantage of slower PL quenching with rising temperatures. In previous chapters, we observed the PL signal decayed much faster for T>60 K due to the thermal excitation of carriers out of the QDs. In this structure, there was only very slight difference in the quenching rates between T < 100 K and T > 100 K. This agrees well with the significant drop of QD PL percentage for T > 100 K plotted in Fig. 6.7. And it is clear from Fig. 6.8 that the DWELLs on InP can maintain a much stronger PL signal than the QDs on InAs for T > 100 K. By using the same method as for QDs grown on GaAs, the excitation energy of the DWELL structure was extracted from the PL quenching plot (~80 meV), which agreed very well with the GHH state confinement energy (~87 meV) shown in Fig.6.5c.
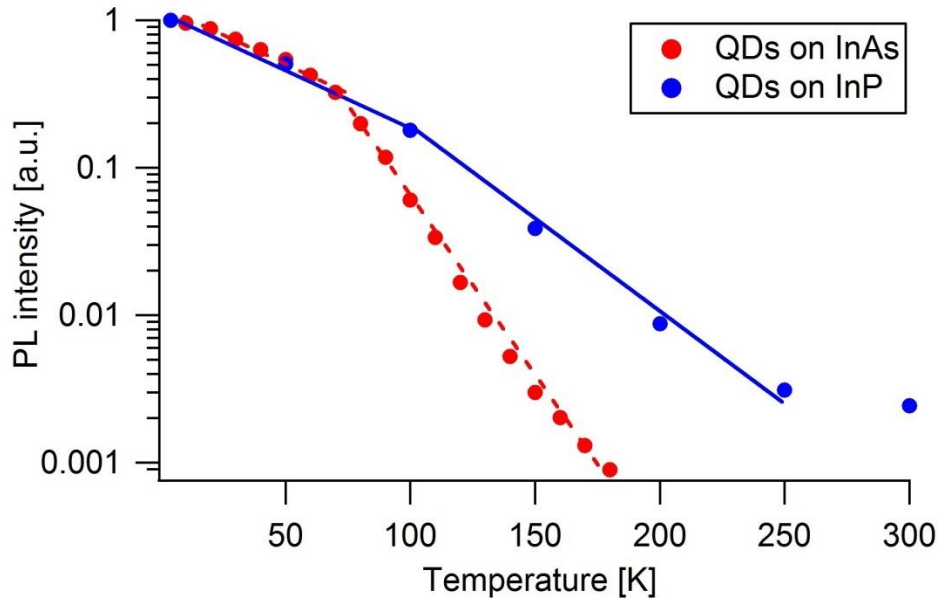
Fig. 6.8 Normalized integrated QDs PL intensities at different temperatures from the sample grown on InP substrate (blue dots) and the one grown on InAs substrate (red dots). The blue lines indicate the exponential fit for T < 100 K and T > 100 K regions of the sample on InP. The red dashed lines indicate the exponential fits for T < 60 K and T > 60 K regions of the sample on InAs.

The temperature dependence of PL intensity *I(T)* can be approximated as:

$$I(T) = I_0 exp\left(\frac{T}{T_c}\right) \tag{6.2}$$

122

Where I_0 is the intensity at 0 K and T_c is the characteristic temperature. Larger value of T_c corresponds to slower quenching of PL with temperature. From the exponential fits in Fig. 6.8, for the QDs on InAs T_c was only 18 K for T > 60 K, and for QDs on InP it was about 32 K for T > 100 K, indicating slower quenching of the QDs on InP probably due to the help of higher valence band barriers. To further reduce the hole leakage rate, the Ga composition in the InGaAs barrier could be increased so as to have even larger valence band offset. The T_c in the lower temperature range for both of the two samples was around 63 K, despite the fact that the two samples emitted at different wavelengths and had different band alignments. Apart from the thermal leakage problem, Auger recombination is still one of the possible reasons contributing to the rest of PL quenching. In bulk InAs material, the band gap E_g is very close to the split-off band Δ_{so}, making the CHSH process very likely. In both bulk InAs and InSb, due to the small value of electron effective mass, the CHCC process could also possibly be strong [155]. For the type II InAsSb QDs, it is still unclear how strong the Auger recombination can be, and which process could be dominant. Hydrostatic pressure dependent measurements can help to quantify how strong the Auger process is in our QD structure [156], [157], but due to the time limitation, these experiments are not included in this work. The role of Auger processes in the QD lasers will be further discussed in the following chapter.

6.6 Conclusions

In this chapter, the STEM image indicated that the QDs were typically about 2.5-3 nm in base radius and 2-3 nm in height. Simulation results implied that the QD composition was probably close to $InAs_{0.60}Sb_{0.40}$ instead of pure InSb. It was observed that there is a slight blue shift of PL peak wavelength with increasing temperature for T < 50 K, resulting from the Fermi-Dirac distribution of holes among QDs through tunneling. The integration of InAsSb QDs layers onto InP substrates was achieved by using an $InAs_{0.65}P_{0.35}$ metamorphic buffer layer. The structure of the QDs was also modified by growing $In_{0.84}Ga_{0.16}As$ barrier layers on both sides,

forming a DWELL structure. The QD PL signal was shifted to 2.7 μm due to the deeper hole confinement. The higher valence band offset of $In_{0.84}Ga_{0.16}As$ proved to be very helpful in reducing the thermal escape of holes which caused the quicker PL quenching at higher temperature range.

7. InSb quantum dot diode lasers

7.1 Introduction

Despite the rapid progress in QW lasers, especially QCL and ICL for the mid-infrared range mentioned in previous chapters, there have been relatively few reports of lasing from InSb QDs. In this chapter, we improved the structure of the laser by implementing a hybrid design using p-doped $InAs_{0.61}Sb_{0.13}P_{0.26}$ grown by LPE, and MBE-grown n+ InAs (with two-step n-doping) as the cladding layers. We obtained lasing at around 3.1 μm up to 120 K in pulsed mode, which is a significant improvement compared with previous results. The gain from the type II QDs and the loss in the waveguide was determined. The details of the laser wavelength tuning with temperature and injection current were also investigated.

7.2 QD laser structure

The InSb QD laser structures were grown on (100) oriented p-InAs substrates as shown in Fig. 7.1a. A 2 μm thick $InAs_{0.61}Sb_{0.13}P_{0.26}$ cladding layer was deposited by LPE from an indium-rich melt in ultrapure hydrogen using a conventional horizontal multi-well graphite sliding boat. Zn was added as the p-type dopant, resulting in a doping concentration of $1x10^{18}$ cm^{-3}. The waveguide region containing the InSb QDs and the n+ InAs cladding layer were then grown upon it in a VG-V80H MBE reactor. In-situ reflection high energy electron diffraction was used to monitor surface reconstruction. A 0.5 μm thick undoped InAs layer was deposited

on the $InAs_{0.61}Sb_{0.13}P_{0.26}$ layer first, followed by 10 layers of InSb QDs with a 20 nm thick InAs spacer between each layer. The growth of InSb/InAs QDs followed the exchange growth method described in our previous work [8-10], where small sub-monolayer InSb QDs were obtained at a high density of $\sim 10^{12}$ cm^{-2}. A further 0.5 μm thick undoped InAs layer was deposited to complete the active region. We obtained photo-luminescence from the active region in the range 3.2-3.6 μm depending on InSb thickness and measuring temperature. The n-type cladding layer (Te-doped) consisted of 0.3 μm thick n-InAs on top of the waveguide with a doping concentration of 1×10^{17} cm^{-3}, followed by 1.7 μm thick n+ InAs layer with a doping concentration of $> 1 \times 10^{18}$ cm^{-3}. Although n+ InAs cladding layers can provide plasmonic enhancement in some QCL structures, the doping concentration needs to be higher than 1×10^{19} cm^{-3} [117]. So in our laser structure, surface plasmonics will not happen at the interface between the n-cladding layer and the waveguide. The LPE grown $InAs_{0.61}Sb_{0.13}P_{0.26}$ has been previously used as the cladding layer for bulk InAs lasers which can operate above 200 K [46]. Because the free carrier absorption in the n+ InAs cladding layer can result in large waveguide loss, a two-step doping was used to reduce the loss while maintaining the optical confinement. The fundamental TE mode profile along the growth direction is shown in Fig. 7.1(b) with the refractive index profile of the constituent parts. The mode profile was simulated using the photonics and microwave module in COMSOL physics. The wavelength was set at 3.1 μm in the simulation.
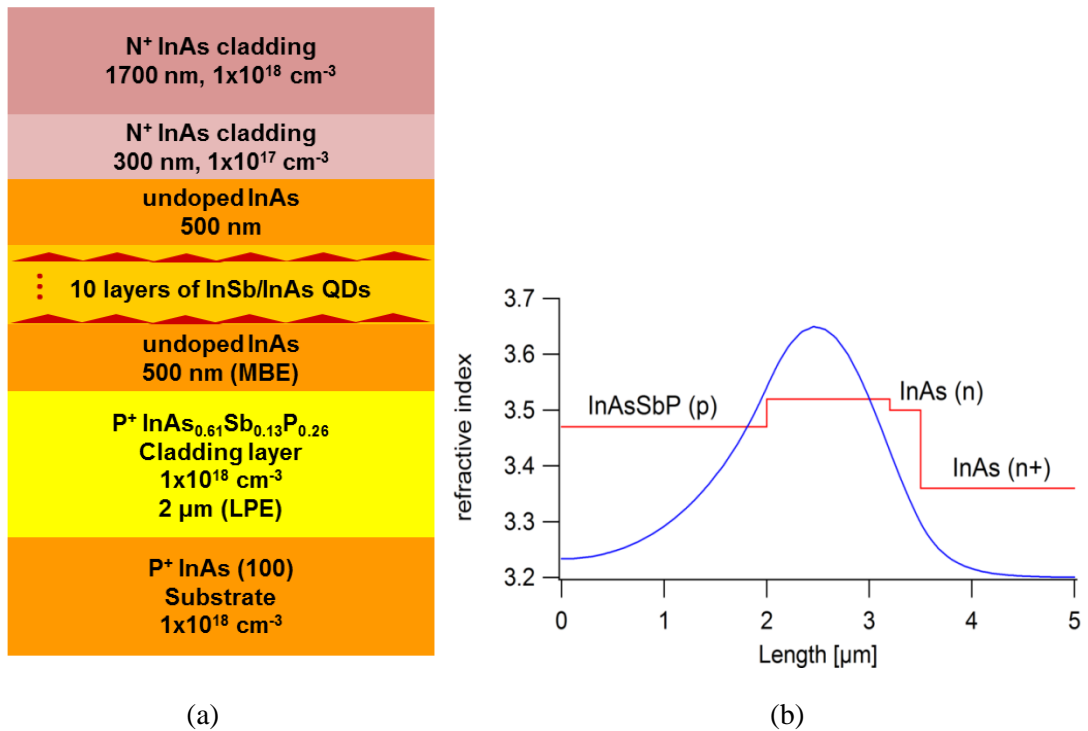
Fig. 7.1 (a) Schematic of the hybrid QD laser structure grown using LPE for the lower part and MBE for the upper part, (b) The fundamental TE mode profile along the growth direction of the laser structure (blue curve). The refractive index of different layers in the structure is also illustrated (red line).

After growth, 75 μm wide broad area laser diodes, with varying cavity lengths, were fabricated by conventional lithography and wet etching. Ti/Au (20 nm/200 nm) metallization was evaporated on both sides to form the ohmic contacts. The diodes were mounted and wire-bonded on T0-46 headers.

7.3 Electrical characteristics

Current-voltage measurements at different temperatures of a 0.74-mm-long cavity laser showed typical p-i-n diode characteristics (Fig. 7.2). The turn-on voltage decreased from 0.34 V at 4 K to 0.10 V at RT. The diode series resistance can be calculated from the slop of the I-V curve after turn-on. Its value stayed around 2.1 Ω with varying temperatures. The reverse leakage current was kept at a low level (0.5 mA with 0.5 V reverse voltage at 4 K and 4 mA at RT).
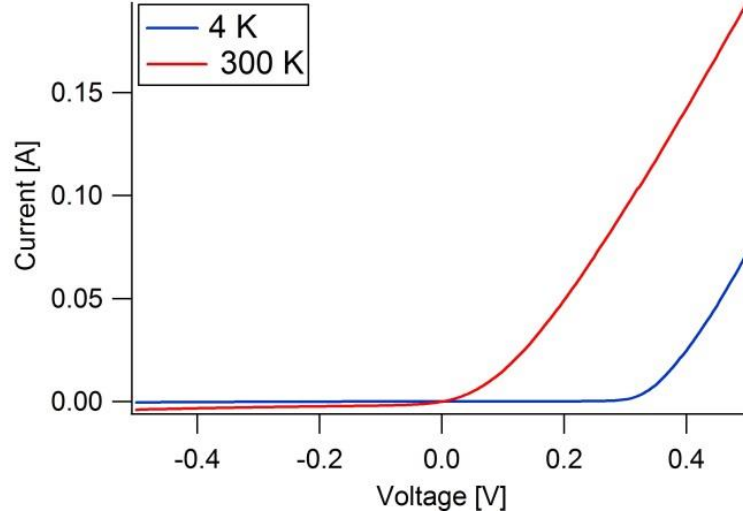
Fig. 7.2 I-V curves of the laser diode at 4 K and 300 K.

7.4 Gain and loss

The J_{th} of the laser diodes at 4 K with pulsed excitation (100 ns pulse width, 2 kHz repetition rate) increased from 1.59 kAcm^{-2} to 4.68 kAcm^{-2} as the cavity length was reduced from 1.17 mm to 0.33 mm. Using the same method as for QW lasers[159], the gain of the InSb/InAs QD lasers can be estimated from the relation between J_{th} and different laser cavity lengths L:

$$J_{th} = \frac{n_w J_{tr}}{\eta_i} exp\left(\frac{\alpha_i + \frac{1}{L} ln\left(\frac{1}{R}\right)}{n_w \Gamma_w G_0}\right)$$

(7.1)

where n_w is the number of QD layers, J_{tr} is the transparency current density per layer, η_i is the internal quantum efficiency, α_i is the waveguide loss, R is the reflection coefficient of the end facet, $\Gamma_w G_0$ is the modal gain in which Γ_w is the optical confinement factor per layer and G_0 is the material gain coefficient.

Equation 7.1 can be re-written as:

$$ln(J_{th}) = ln\left(\frac{n_w J_{tr}}{\eta_i}\right) + \frac{\alpha_i}{n_w \Gamma_w G_0} + \frac{ln\left(\frac{1}{R}\right)}{n_w \Gamma_w G_0} \cdot \frac{1}{L}$$

(7.2)

127

By making a linear fit between **ln(J_{th})** and **1/L**, the slope of the fit equals the term in front of **1/L**, in which the modal gain (**Γ_wG_0**) can be extracted.
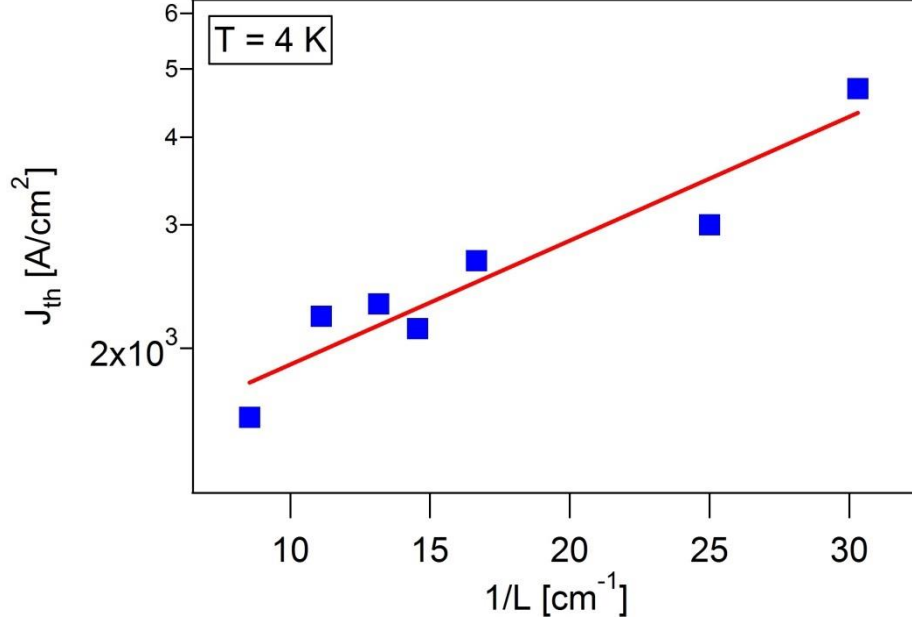
Fig. 7.3 Threshold current density vs reciprocal cavity length of the laser diodes at 4 K. The red line shows the linear fit between ln(J_{th}) and 1/L.

The J_{th} vs 1/L relation is shown in Fig. 7.3. The estimated modal gain from this plot is 29 cm^{-1}, which means 2.9 cm^{-1} per InSb QDs layer in average since there are 10 layers of QDs in our laser structure. This value is lower than that for (e.g. InAs) type I QDs emitting in the near infrared spectral range, which is in the order of 10 cm^{-1} per QD layer [160], but is close to that found in type II QW lasers emitting at a similar wavelength [159]. In type II structures, there is much larger spatial separation between electrons and holes than in type I structures, resulting in a smaller electron-hole wave function overlap, which is directly related to the lower gain per layer. In our InSb/InAs QDs, only the holes are confined within the QDs and the electrons reside in the InAs matrix. Single band Schrödinger calculations indicate that only the ground heavy hole (GHH) state is confined within the QDs. The wave function overlap is estimated to be 36% from the calculation, which is lower than in type I QDs and W-structures [67], [161]. However, because the QD density is ~10^{12} cm^{-2} per layer, an exceptionally high material gain (G$_0$) of 19 x10^4 cm^{-1} can be estimated for our type II QD,

which is in the same range as type I QDs [162]. So despite the smaller electron-hole wave function overlap, the type II InSb/InAs QDs can serve as an efficient gain medium for mid-infrared laser diodes.

The details of the laser spectrum can be revealed by using FTIR spectroscopy. The measured spectra at 4 K with different current injections are plotted in Fig. 7.4a. Two most representative groups of modes are circled in this figure. Using the Hakki-Paoli method, the net gain of these two groups at 4 K can be estimated [163]. The results are plotted in Fig. 7.4b. With increasing current, the gain of the longer wavelength mode group (red dots) became saturated ahead of the shorter wavelength mode group (blue dots), which means the longer wavelength modes can reach threshold with less current injection. This coincides with the free migration of carriers between QDs with different sizes, which results in the QDs with lower energy states being occupied first. So the longer wavelength lasing can happen first.
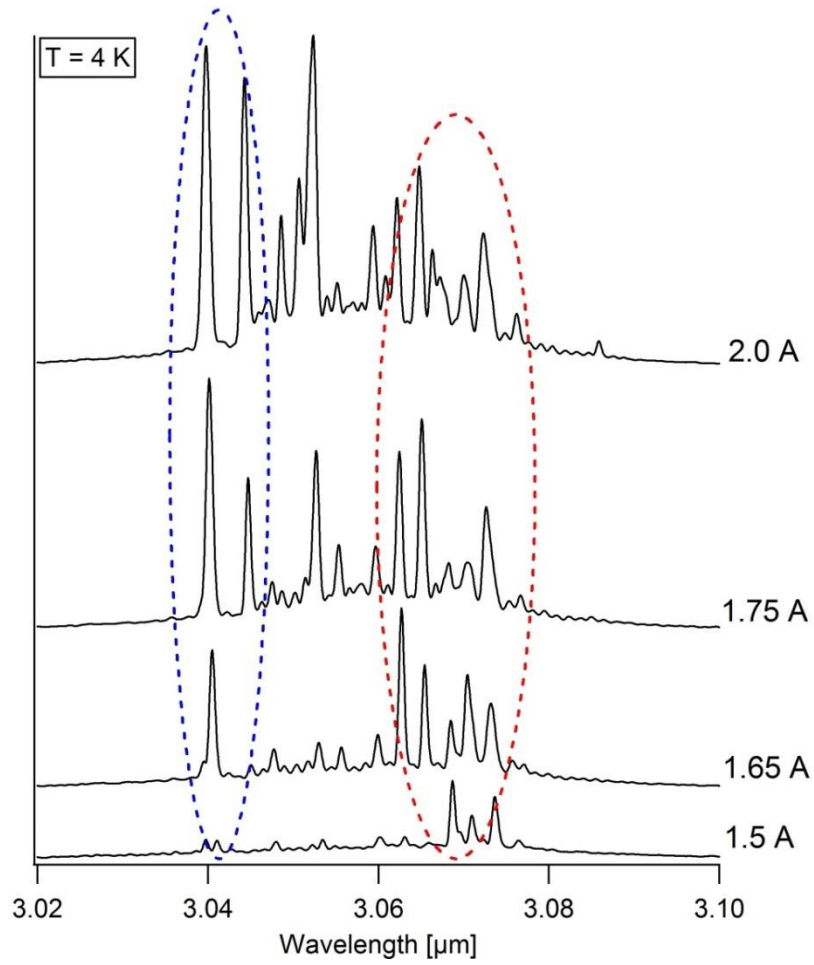
(a)
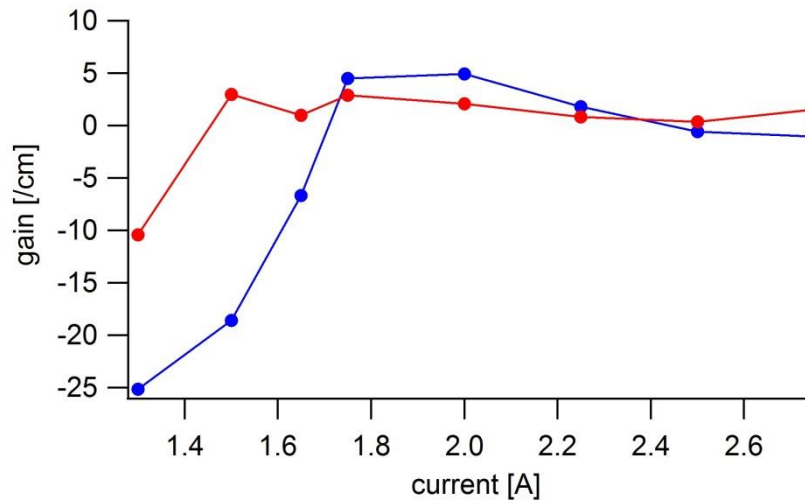
(b)

Fig. 7.4 (a) Multimodal laser spectra measured at 4 K at different current injections. Two representative groups of modes are circled in red and blue dashed lines. (b) Estimated net gain of the two groups of modes with changing currents at 4 K.

From equation 2.59, the external differential quantum efficiency (η_d) can be measured from the slope of the laser output power against the drive current. Since only a part of the coherent light is fed back by the mirrors and retained within the laser, η_d is less than the internal quantum efficiency (η_0). The relation between the two is [164]:

$$\frac{1}{\eta_d} = \frac{1}{\eta_0}\left(\frac{\alpha_i L}{ln\left(\frac{1}{R}\right)} + 1\right) = \left(\frac{1}{\eta_0} \cdot \frac{\alpha_i}{ln\left(\frac{1}{R}\right)}\right) \cdot L + \frac{1}{\eta_0} \tag{7.3}$$

As stated in previous chapters, in our experiments we cannot measure the absolute power of the laser emission, thus the value of η_d is still unknown, but the measured laser intensity is proportional to the power. The slope in Fig. 7.5a is also proportional to the η_d, so we have:

$$\frac{1}{slope} = K \cdot \frac{1}{\eta_d} = \left(\frac{K}{\eta_0} \cdot \frac{\alpha_i}{ln\left(\frac{1}{R}\right)}\right) \cdot L + \frac{K}{\eta_0} \tag{7.4}$$

where K is a constant. By measuring the slopes of laser diodes with different cavity lengths, a linear fit can be made between $1/slope$ and L ($1/slope = A + B \cdot L$). From the values of the fitted parameters A and B, one can estimate the waveguide loss:

$$\alpha_i = \frac{B}{A} ln\left(\frac{1}{R}\right) \tag{7.5}$$
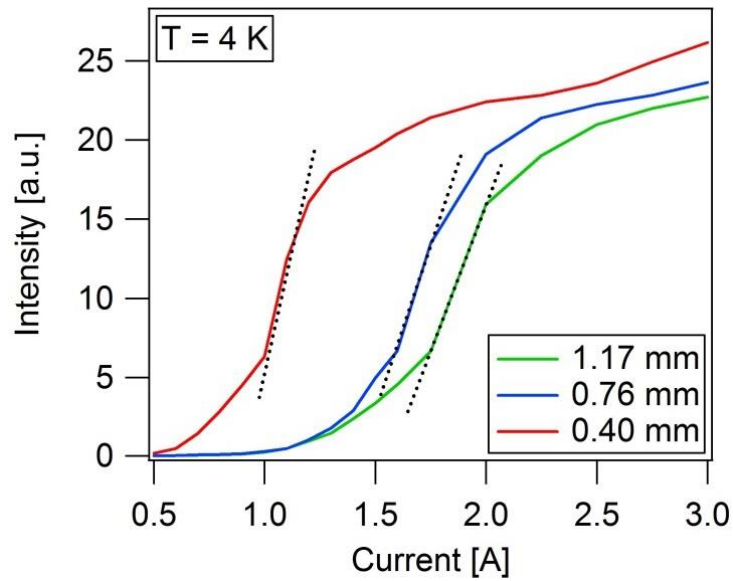
(a)
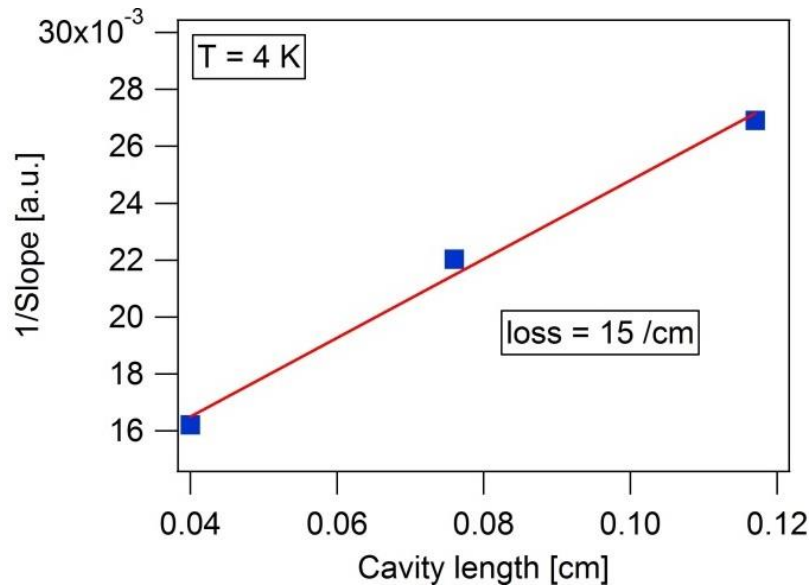
(b)

Fig. 7.5 (a) Intensity vs current plot of laser diodes in different cavity lengths at 4 K. (b) The relation between 1/slope and the cavity length. The red line is the linear fit.

The intensity vs cavity length plot is shown in Fig. 7.5a, where the slopes were extracted from, and plotted in Fig. 7.5b. The estimated waveguide loss was around 15 cm^{-1}. Possible contributions to α_i include free carrier absorption and the scattering loss caused by the relatively rough InAs$_{0.61}$Sb$_{0.13}$P$_{0.26}$ interface. Since the effective mass of holes is much higher than electrons in InAs and InAs$_{0.61}$Sb$_{0.13}$P$_{0.26}$ resulting in much smaller free carrier absorption

than n- type materials, even though larger part of the optical mode extends into the p-InAs$_{0.61}$Sb$_{0.13}$P$_{0.26}$ cladding in Fig.7.1b, the absorption in the p-region can still be neglected. this lasing wavelength is very close to the band-to-band absorption of the undoped InAs. So the absorption loss in the InAs waveguide may possibly be quite significant.

However, it needs to be noted that by using this method to estimate the waveguide loss, it is assumed that η_0 stays constant with changing current injections. Adams et al. demonstrated that in the InAs QD lasers, since most of the QDs are electrically and optically disconnected, the η_0 cannot be constant with increasing current [165], so this method might not be accurate to determine the waveguide loss. However, in our InSb QDs, we have shown the indication of dot-to-dot carrier transfer in previous chapters, which means the QDs can be assumed to be connected. So in our case, we believe this method is still valid to evaluate the waveguide loss.

7.5 Spontaneous emission

The spontaneous electroluminescence (SE) emission spectra from the laser diodes can be measured when the injected current is below threshold. An interesting phenomenon has been observed that with increasing current injection, there was a clear blue shift of the SE peak position. In Fig.7.6a, the SE peak was at 3.236 μm with 50 mA current injection, but moved to 3.094 μm with 750 mA current injection, corresponding to an energy difference of about 18 meV. The above threshold spectrum at 1.0 A (red curve) is also shown in the graph. The peak was located on the shorter wavelength side, but was very close to the peak of the SE spectrum at 750 mA (blue curve). A bump with much weaker intensity than the main peak can also be observed at around 3.0 μm from the 750 mA curve, which most likely originated from the InAs emission.

(a)   (b)
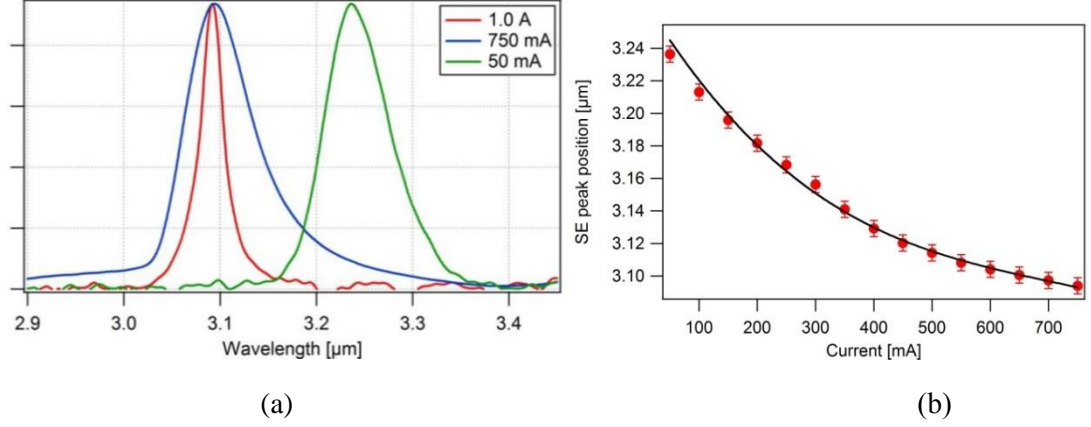
Fig. 7.6 (a) Comparison of the below threshold emission spectrum at 0.05 A current injection (green curve) and at 0.75 A current injection (blue curve) with the laser spectrum at 1.0 A current injection (red curve). The peak intensities of the three spectra have been normalized. (b) Below threshold spontaneous emission peak wavelength shift with increasing current from a laser diode measured at 4 K. The threshold current of this laser is around 950 mA.

The SE peak position against the injected current is plotted in Fig. 7.6b. It is obvious that in the lower current range the rate of the SE peak shift is greater than in the higher current range. Since in previous chapters we already confirmed that there is only one quantized heavy hole state in this kind of QDs, one possible reason to explain the SE peak shift is the band-bending effect caused by the electric field in type II structures. When the holes occupy the QDs, the electrons can be attracted closer to them, causing the conduction band to bend into a triangular shape, as illustrated in Fig. 7.7a. Quantized electron states may occur in the triangle, resulting in higher recombination energy. Blue shifts caused by band-bending have already been reported from other kinds of type II QWs [166] and QDs [167]. In the case of PL, to calculate the energy shift due to band-bending, one can start from the relation between the radiative recombination coefficient B and the absorption coefficient α [166]:

$$Bn^2 = \alpha LS \tag{7.6}$$

where L is the thickness of the absorbing layers, S the photon flux, and n the carrier density which also equals:

$$n = k\sqrt{P} \tag{7.7}$$

where k is a constant and P the incident laser power density.

In a triangular well, the ground state energy is given by:

$$E_0 = bF^{2/3} \tag{7.8}$$

where b is also a constant and the electric field F can be expressed as:

$$F = \frac{2\pi e n}{\varepsilon_r} \tag{7.9}$$

where e is the electron charge and ε_r is the permittivity. By combining equations 6.7-9, we have:

$$\Delta E_B \propto P^{1/3} \tag{7.10}$$

where ΔE is the energy shift. In the case of EL, by replacing the incident laser power P with the injected current I, equation 7.10 can still hold true:

$$\Delta E_B \propto I^{1/3} \tag{7.11}$$
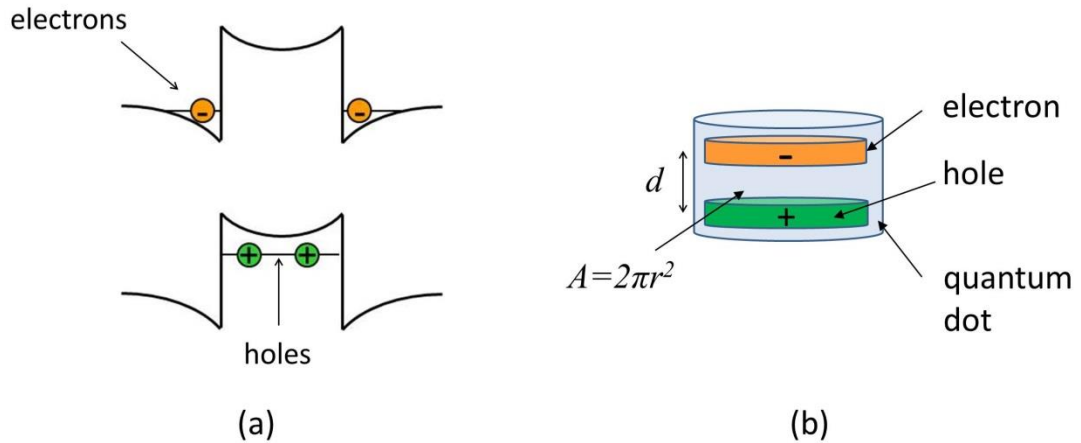
Fig. 7.7 (a) Illustration of the band-bending effects caused by the electric field in type II nanostructures. (b) Sketch of the simple capacitor model for a QD.

Another possible reason that can cause the blue shift of SE peak is the charging of QDs. In type II structures, since electrons and holes are more spatially separated, the repulsive Coulomb force between carriers of the same type (the injected holes in our case) is much

135

greater than the attractive Coulomb force between electrons and holes [168]. In a similar manner to other type II structures [169], the strong interaction between the two holes in GHH state in one InSb/InAs QD can increase the hole energy levels, resulting in a blue shift of the SE peak. For simplicity, a single QD can be modelled as a cylindrical capacitor as sketched in Fig. 7.7b. The capacitance C can be expressed as:

$$C = \frac{A\varepsilon_r}{d} \tag{7.12}$$

where A is the plate area, d the distance between the positive and negative plates and ε_r the permittivity. By placing more than one confined carrier (hole) into a QD, the capacitive charging energy needs to be taken into account. The energy difference caused by charging can be estimated as:

$$\Delta E_C = V\Delta Q \tag{7.13}$$

Since the charge Q is proportional to n, and from the relation in equation 6.7, we can have:

$$\Delta E_C \propto \sqrt{P} \tag{7.14}$$

For the same reason as in equation 6.10, we can replace P with I:

$$\Delta E_C \propto \sqrt{I} \tag{7.15}$$

By taking equation 6.11 into equation 6.12, we can also have the relation:

$$\Delta E_C = \frac{e^2 d}{2\pi r^2 \varepsilon_r} \tag{7.16}$$

where e is the electron charge.

Comparing equations 7.11 with 7.15, it can be noticed that the energy shifts caused by these two mechanisms have different relations with the injected current. The logarithm plot of the measured SE peak shift against the current is shown in Fig. 7.8 below.
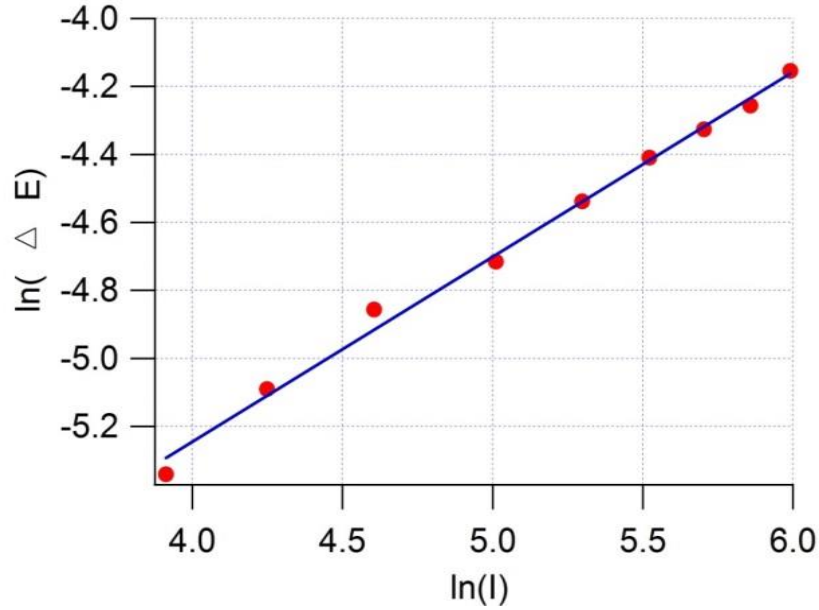
Fig. 7.8 Logarithm plot of the SE peak shift energy at different injected current. The blue line is a linear fit between ln(ΔE) and ln(I).

The slope of the linear fit (blue line) in this plot is 0.53, which is very close to the case in equation 7.15. That proves the QD charging effect is the main reason for the shift of the SE peak. By assuming a QD of 3 nm radius *r* and 2 nm height, the average distance *d* between electrons and holes can be estimated as one third of the height. Taking these values into equation 7.16, $\mathit{\Delta E_C}$ is estimated to be 16 meV, which means the charging effect from the addition of one more holes into one QD can result in an energy shift of about 16 meV. This value is close to the measured overall SE peak shift of about 13 meV. The difference between these two values may originate from the simplicity of this model. It indicates one QD can accommodate only one more hole (two holes in total), which agrees with the simulation results from previous chapters - that there is only one energy state (the GHH state) in the QDs, where the two holes occupy the two different spin states of the GHH state.

In addition, it can be observed from Fig. 7.7b that, the SE peak shifted more at lower current injection range than near threshold range. The smaller trend of the SE peak shift at higher current injection indicates that before reaching threshold, more and more QD GHH states are

becoming fully occupied, which also implies that single hole occupation on the GHH state is not enough to provide sufficient gain to support lasing.

7.6 Non-radiative current
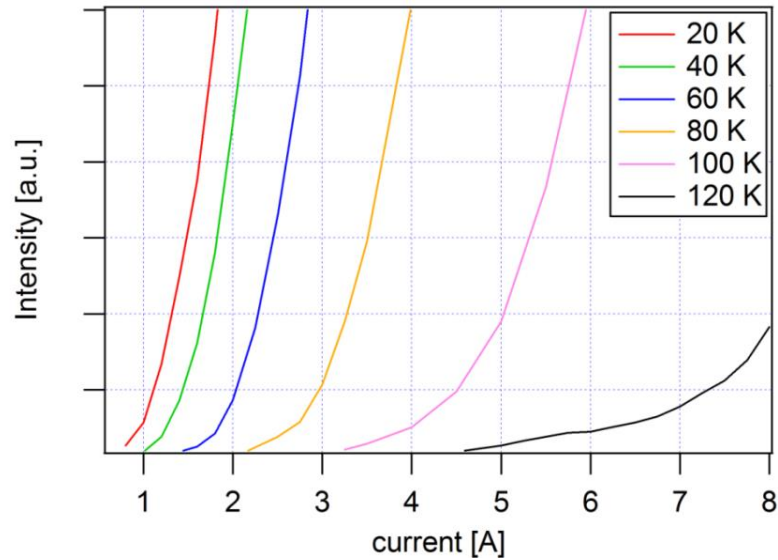
Fig. 7.9 Output light intensity vs pulsed injection current (100 ns pulse width, 2 kHz repetition rate) from a 0.68 mm long, 75 µm wide laser at temperatures from 20 K to 120 K.

Fig. 7.9 shows the measured light intensity from one facet of a laser diode with increasing pulsed excitation currents at different temperatures. Using as short as 100ns pulse width at 2 kHz, the effect of Joule heating can be minimized. The measured T_{max} was increased from 60 K in previous work to 120 K. J_{th} of this laser diode can be derived from the curves in this figure and is plotted in Fig. 7.10. When the temperature was below 50 K, the characteristic temperature T_0 was calculated to be 101 K. For the temperature range between 50 K and 120 K, the value of T_0 dropped to 48 K. Possible reasons for the increase of J_{th} and decrease of T_0 include the leakage current, Auger recombination and SRH recombination. In this laser structure, the injected electrons are very likely to escape the active region into the p-doped $InAs_{0.61}Sb_{0.13}P_{0.26}$ cladding layer because of i) the small effective mass of electrons compared with holes, ii) the shallow conduction band offset between InAs waveguide and InAsSbP

cladding layer (~50 meV), iii) the lack of electron confinement in the type II QDs. The leakage of holes can probably be very significant because in this structure there is no valence band barrier in the n-cladding, which is the same material as the waveguide region (InAs). The leakage current caused by electrons can be expressed as [170]:

$$J_{nl} = \frac{qD_nN_p}{L_n tanh\left(\frac{w}{L_n}\right)} \tag{7.17}$$

and for the leakage current caused by holes:

$$J_p = \frac{qD_pP_n}{L_p tanh\left(\frac{w'}{L_p}\right)} \tag{7.18}$$

where q is the electron charge, w and w' are the thicknesses of p- and n- cladding layers (2 μm), $D_{(n,p)}$ is the diffusion coefficient for electrons or holes, which can be expressed as:

$$D = \frac{kT\mu}{q} \tag{7.19}$$

where k is the Boltzmann constant, T is the absolute temperature and μ is the electron/hole mobility. In equations 7.17 and 7.18, $L_{(n,p)}$ is the diffusion length, which can be calculated from:

$$L = \sqrt{D\tau} \tag{7.20}$$

where τ is the carrier lifetime. For simplicity, the value is set at the constant value of 3 ns for both electrons and holes. N_p and P_n are the concentration of electrons/holes into the p-/n-cladding layers, which can be derived from:

$$N_p = N_{CC} \exp\left(\frac{-\delta N}{kT}\right) \tag{7.21}$$

and

$$P_n = N_{VC} \exp\left(\frac{-\delta P}{kT}\right) \tag{7.22}$$

where N_{CC} and N_{VC} are the effective density of states in the conduction and valence band, δN and δP are the conduction and valence band offsets.

The total leakage current density J_{leak} would be:

$$J_{leak} = J_{nl} + J_{pl} \qquad (7.23)$$

The electron/hole leakage problems are illustrated in Fig. 7.10.

In bulk semiconductor lasers, the total current density J_{tot} can be written as [171]:

$$J_{tot} = J_{leak} + ed_{eff}(An + Bn^2 + Cn^3) \qquad (7.24)$$

Where the terms An, Bn^2 and Cn^3 represent SRH, radiative and Auger recombination, n is the threshold carrier density and d_{eff} is the effective width of the active region. For our QD laser, the radiative coefficient B has not yet been decided, but as stated in previous chapters, the ideal QDs have temperature independent radiative current density. So equation 7.24 can be re-written as:

$$J_{tot}(T) = J_{leak} + J_{rad} + ed_{eff}(An + Cn^3) \qquad (7.25)$$

where the radiative current density J_{rad} is at constant value with changing temperatures.
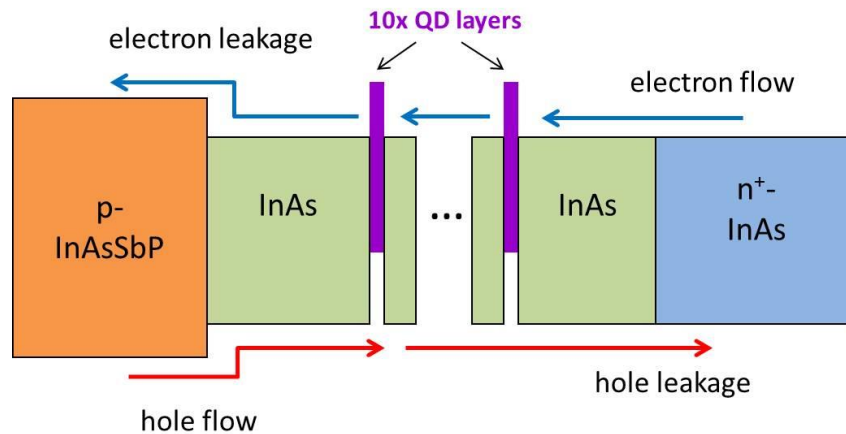
Fig. 7.10. Illustration of the band alignments and electron/hole leakage current.

Until now the Auger coefficient C of the In(As)Sb/InAs QDs is still unknown. For the purpose of evaluating different non-radiative currents, its value was set the same as the InAs/InGaSb type II QWs at similar wavelength (2×10^{-27} cm^6/s) [172]. For simplicity, SRH coefficient A was also set as a constant (2.5×10^8 cm^2/s) [170]. The temperature dependence of n was derived in the same way as in [170], and J_{leak} is from equation 7.23. The calculated SRH current J_{SRH} (orange curve), Auger current J_{Auger} (pink curve) and J_{leak} (green curve) were plotted in Fig. 7.11 below. Since the n-InAs cladding layer cannot provide any hole blockage, the δP in equation 7.22 was set to be 0. The J_{tot} (black curve) was fitted to the experimental data J_{exp} (red dots) by adjusting the value of J_{rad} (blue line). It is obvious that for T < 40 K, the current for all these three non-radiative mechanisms are negligible compared with the measured data J_{exp}. So the high J_{th} at low T region can only be attributed to the radiative recombination. The J_{rad} was fixed at 2.5 kA/cm^2 to make a reasonable fit between J_{tot} and J_{exp}. This rather high value of J$_{rad}$ at low T is most probably caused by the distribution of QD size and composition, so that only a small fraction of QDs achieve threshold at the same injection level, and a large part of the radiative current is essentially wasted. Fig. 7.4a confirms that QD of different sizes give coherent emission at different injection levels, with the larger QDs (at longer wavelengths, circled in red) being the first to reach threshold. Fig. 7.11 also implies that J_{leak} is the dominant non-radiative factor for T > 50 K. In fact, according to this calculation, at 120 K only 17% of the total current was for radiative recombination, while leakage current consumed 67% of the total current. Within the J_{leak}, the hole leakage is the dominating factor. Because the n- cladding layer is made of the same material as the waveguide (InAs). Even though the J_{Auger} increases most drastically with rising temperature, it will only become larger than J_{rad} for T > 150 K. At 300 K, the calculated J_{tot} exceeded 100 kA/cm^2, which is not practical for laser diodes. In order to improve the T$_{max}$ and reduce J$_{th}$, firstly, the J_{leak} should be effectively suppressed, probably by inserting hole blocking layers in the laser structure. Secondly, the J_{rad} also need to be reduced which can only be achieved by increasing the modal gain of the QDs.
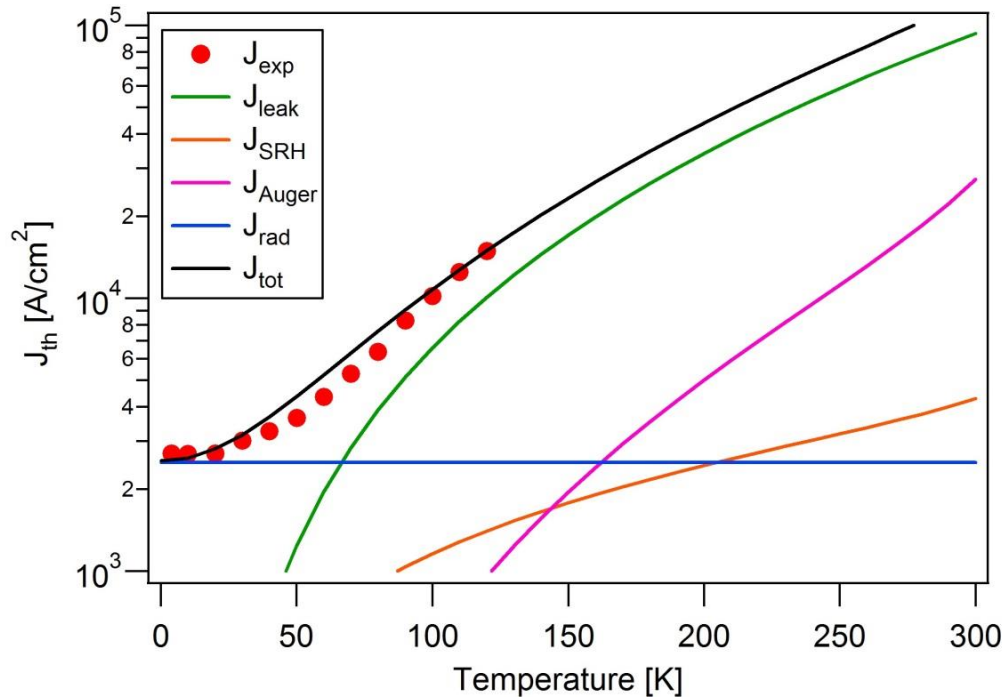
Fig. 7.11 Measured threshold current density (red dots) of the 0.68 mm long, 75 μm wide laser at different temperatures. Calculated J_{leak} (green curve), J_{SRH} (orange curve), J_{Auger} (pink curve), J_{rad} (blue line) and J_{tot} (black curve) are also presented.

The value of T_0 at different temperatures can be interpreted by taking each two adjacent data points in Fig. 7.11, and the result is plotted in Fig. 7.12, from which we can observe a significant decline of T_0 in the 40-60 K range. The upper limit of T_0 for J_{Auger} was approximated as $T_0=T/3$ [173] and the T_0 of J_{leak} was derived from the J_{leak} curve in Fig. 7.11. Both of the T_0's are sketched in Fig.7.12. The T_0 from J_{leak} is very close to the measured data for T > 80 K, which confirms that J_{leak} becomes the dominating mechanism at high T.
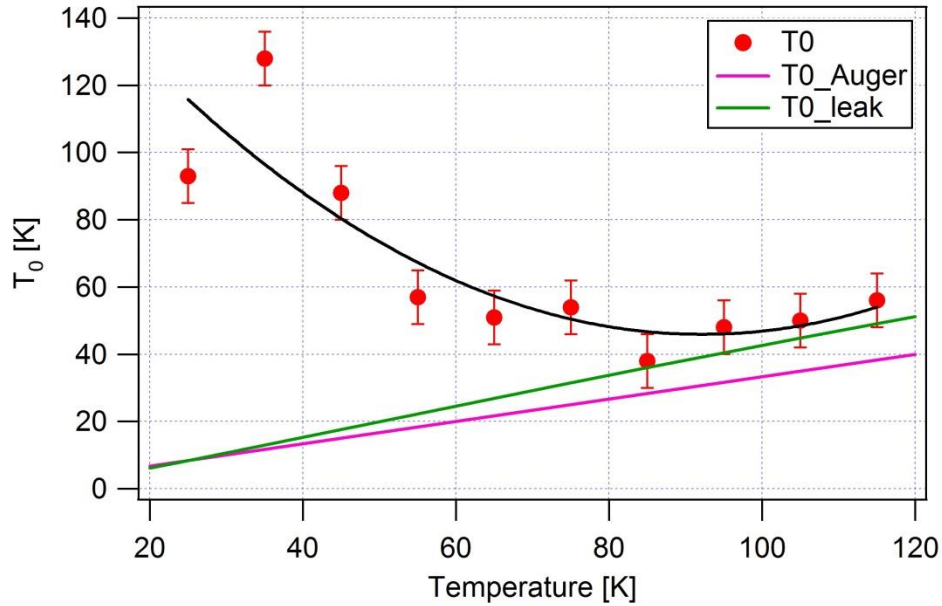
Fig. 7.12 Temperature dependence of T_0 of the QD laser (red dots), compared with the T_0 of leakage current (green line) and Auger current (pink line). The black curve illustrates the trend of measured T_0 change with temperature.

7.7 Wavelength tuning characteristics

The peak emission wavelength of laser diodes with different cavity lengths varies between 3.02 μm and 3.11 μm. The emission spectrum contains multiple longitudinal modes from the Fabry-Pérot laser cavity. The inset in Fig. 7.13 shows one envelope of the laser spectrum measured at 4 K. For the same laser diode, the emission spectrum also changed with temperature at constant current injection. The peak of the laser spectrum shifted to shorter wavelength with increasing temperature when T < 50 K. For T > 50 K, the peak moved to longer wavelength as temperature increased, resulting in a U-shaped plot as shown in Fig. 7.13. This behaviour coincided with the trends in the PL wavelength shift observed from the InSb/InAs QDs in previous chapters and reports. [97] The competition between the carrier distribution among QDs and band gap narrowing with increasing temperature causes the U-shaped tuning behaviour of the laser wavelength. It can also be expected that if the laser can operate with T > 120 K, the emission peak would move to longer wavelengths.
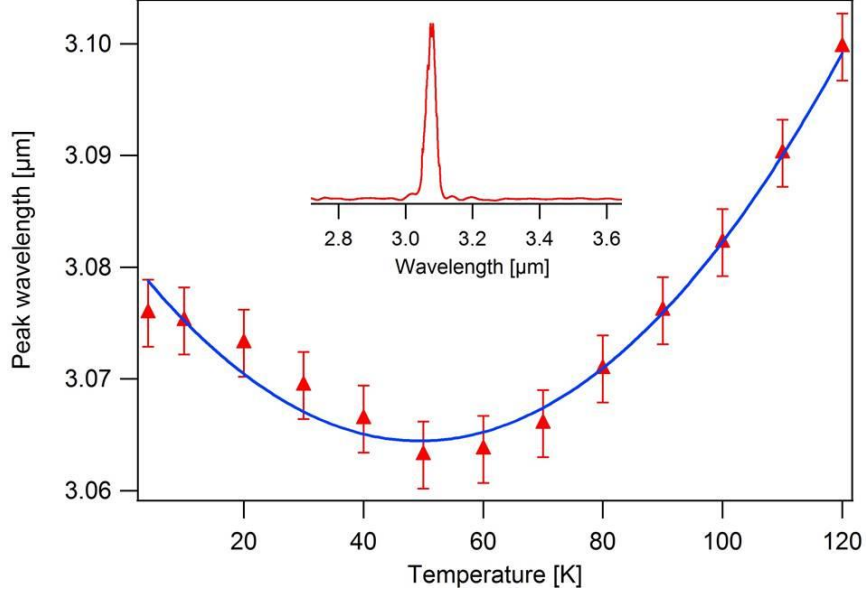
Fig. 7.13 Peak positions of the laser emission envelope with 8.0 A pulsed current injection measured at different temperatures. The inset shows the emission spectrum at 4 K.

Using FTIR spectroscopy, the multimodal spectra of the laser emission can also be measured. Fig. 7.14a gives an example of the detailed spectra of the laser with different pulsed current injection at 30 K. It was found that by increasing the injected current, each of the cavity modes shows a slight blue shift. With a pulse with of 100 ns at 2 kHz repetition rate, the thermal heating effect of the laser cavity caused by increased current can be neglected, and the shift is due to the carrier induced refractive index change. Fig. 7.14b plots the shift of one of the strongest modes with changing current measured at 30 K (indicated by the dotted line in Fig. 7.14a). The trend agrees quite well with the linear fit (solid line in Fig. 7.14b), resulting in a tuning rate of -1.76 nm/A. This movement is most probably caused by the change of material refractive index Δn with increased injection of current. The relation between Δn and $\Delta\lambda$ is [174]:

$$\frac{\Delta n}{n} = \frac{\Delta\lambda}{\lambda} \tag{7.26}$$

Assuming an electron mobility of 10^4 cm^{2}V^{-1}s^{-1} for InAs with high carrier concentration at low temperature, the electron density in the waveguide region at 2 A current injection can be approximated to be 10^{21} cm^{-3}. By taking into account the band filling effect, band gap

narrowing effect and free electron absorption [175], [176], the change of refractive index was around 3×10^{-3} when the current was increased from 2 to 5 A, resulting in a wavelength shift of 2.7 nm according to equation 7.20, which is the same order of magnitude as the measured wavelength shift of about 5 nm.
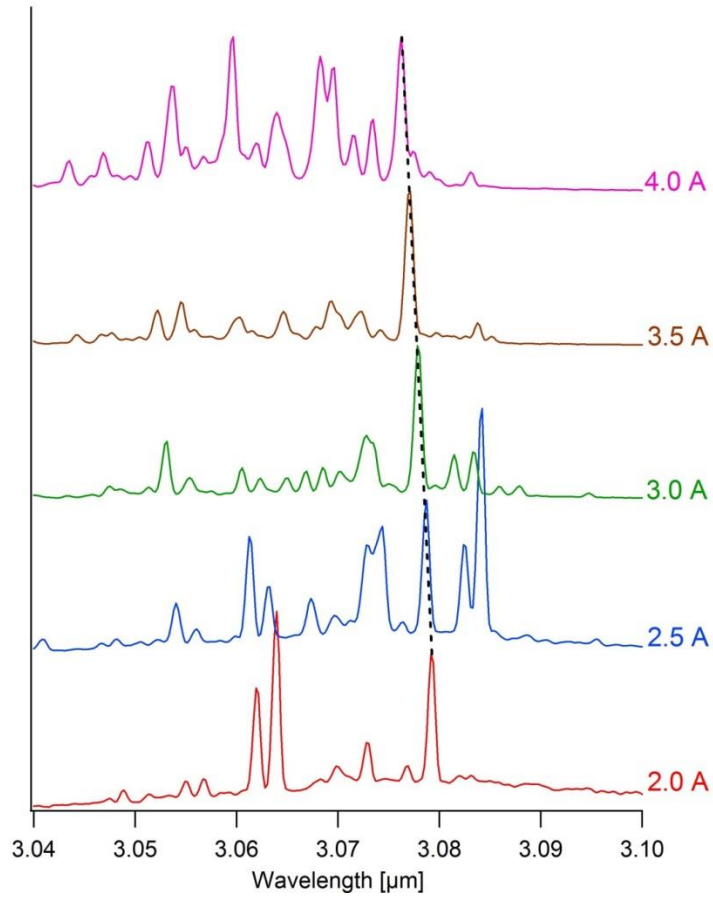
(a)
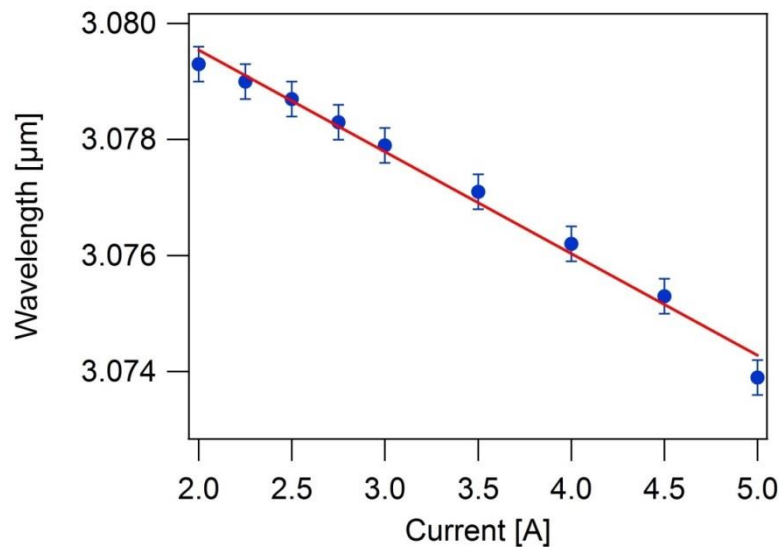
(b)

Fig. 7.14 (a) Measured laser spectra with 2.0 A, 2.5 A, 3.0 A, 3.5 A and 4.0A pulsed current injections at 30 K. The dashed black line highlights the blue shift of one of the longitudinal modes. (b) The peak position of the chosen mode at different current injections. The straight line shows the linear fit which gives a tuning rate of -1.76 nm/A.

7.8 Conclusions

In conclusion, type II InSb/InAs QD laser diodes emitting at around 3.1 μm have been demonstrated and characterized. A hybrid structure was used to fabricate the laser by combining an LPE grown p- $InAs_{0.61}Sb_{0.13}P_{0.26}$ p cladding layer and n+ InAs plasmon cladding layer which resulted in an improved maximum operating temperature due to better waveguide design than in previous work and improved cladding layer material quality compared with AlAsSb. (T_{max} was increased from 60 K to 120 K in pulsed mode). The gain was determined to be 2.9 cm^{-1} per QD layer and the waveguide loss was ~15 cm^{-1} at 4 K. Below threshold SE measurements have shown a strong blue shift of the peak wavelength with increasing current, which is caused by the charging effect of the type II QDs. It also indicates that the laser threshold can only be achieved with full occupation of GHH states in the QDs. T_0 = 101 K below 50 K but decreased to 48 K at higher temperatures. The drop of T_0 and increase of J_{th} with rising temperature are most likely due to the leakage current, especially the leakage of holes into the n- cladding layer. The radiative current at 4 K is still high, which probably originates from the size distribution of QDs. Temperature has a significant effect on the emission wavelength of these lasers, which showed first a blue shift followed by a red shift with increasing temperature, identical to the PL wavelength shift of the InSb QDs. Each peak of the modes also shifted slightly with increasing current due to the change of material refractive index. The modal gain and T_{max} of the laser can possibly be further improved by increasing the optical mode overlap with the QDs and by introducing hole blocking layers to prevent holes escaping from the active region.

8. Conclusions and outlook

8.1 Progress and achievements

The investigations in this thesis can be divided into two parts. Chapters 5 and 6 focused on the integration of the InAsSb/InAs QDs onto other material platforms and the study of the QD properties. Chapter 7 demonstrated the mid infrared QD laser and its characteristics. The major achievements of this thesis include:

- In(As)Sb/InAs QDs were integrated on GaAs substrates for the first time using different metamorphic growth techniques. Mid-infrared PL from the QDs achieved similar intensity and wavelength as for QDs homo-epitaxially grown on InAs substrates. EL from these QDs on GaAs was also demonstrated up to 180 K.

- Thermal leakage of the confined holes out of the QDs was identified as an important mechanism for the decay of QDs PL/EL intensity with increasing temperature.

- By combining the experimental results with STEM images and calculations, it was estimated that due to Sb segregation during growth the As composition in the QDs could possibly be as high as 60%.

- The QDs were integrated on InP substrates for the first time using a metamorphic buffer layer. The QDs were sandwiched between InGaAs barriers, forming a DWELL structure for this type of QDs. In this approach, the exchange growth of the QDs on InGaAs was also demonstrated. The PL appeared at shorter wavelength but can sustain until 300 K when intermediate InGaAs barriers are used between the QDs. Due to the higher valence band offset in this novel QD structure, the thermal leakage problem was less significant.

- Broad area Fabry-Perot QD lasers with an improved structure which incorporated LPE grown $InAs_{0.61}Sb_{0.13}P_{0.26}$ cladding layers were demonstrated operating up to 120 K, which is a significant improvement compared with previous work ($T_{max} = 60$ K).

- The lasers emitted at around 3.1 μm. The charging effect in the type II QDs in the main mechanism responsible for the blue shift of the spontaneous emission.

148

- The modal gain of the QDs was found to be 2.9 cm^{-1} per layer, and the waveguide loss was estimated to be around 15 cm^{-1} at 4 K.

- The size distribution of QDs caused the high value of J_{th} for T < 40 K. At higher temperature range, carrier leakage into the cladding layers was identified as the most possible reason for the increase of J_{th} with rising temperatures.

The work in Chapter 5 involved the integration of mid infrared InAsSb/InAs QDs on GaAs substrates. The growth recipe for the QDs had been developed before the start of this project. However, the QDs had only been grown on InAs substrates. Three different metamorphic growth approaches were investigated to integrate the QDs on GaAs substrates. One with a thick InAs buffer layer, the other two with GaSb and AlSb interlayers using IMF growth techniques and thinner InAs buffer layers. The TEM images implied that the density of threading dislocations in the QDs region reached the order of 10^8 cm^{-2} for the sample with thick InAs buffer, and 10^9 cm^{-2} for the other two samples. Due to their sub-monolayer nature, these QDs did not show any effect in dislocation filtering. Despite the relatively high dislocation densities, the QDs in these three samples all showed similar PL spectra as the QDs grown on InAs. The sample with a thick InAs buffer layer achieved the highest PL intensity. These three QD samples exhibited a similar PL intensity decay trend with rising temperature. For T > 60 K, the decay rate clearly became faster than in the lower temperature range. This was caused by the turn-on of the thermal leakage of confined carriers out of the QDs. EL from the QDs on GaAs substrate was also demonstrated up to 180 K. In EL, the injected carrier density was much higher than in PL and holes were constantly being provided into the QDs by the applied electric field. This could reduce the net rate of escape of holes out of the QDs and help to maintain the EL emission intensity. Consequently the quenching of EL was less rapid than PL.

The following chapter discussed the properties of the InAsSb QDs in more detail. From conventional TEM images, we can only observe layers of the QDs. The size and geometry of individual dots were revealed by STEM images. The QDs were estimated to be 2.5-3 nm in

base radius and 2-3 nm in height. The composition of QDs can only be estimated by combining the COMSOL simulations with experimental results. Apart from pure InSb QDs, the calculation indicated that the QDs may contain up to 60% As. The simulation also implied that there was only one confined state, the ground heavy hole state, in this kind of QD. For the PL peak wavelength, a slight blue shift was observed with increasing temperature for T < 50 K. It was caused by the re-distribution of holes among QDs, which required the migration of carriers between adjacent dots. At low temperature, only tunnelling can be the major migration mechanism. In addition, this chapter also demonstrated the integration of InAsSb/InAs QDs on InP substrates with $InAs_{0.65}P_{0.35}$ metamorphic buffer layer and $In_{0.84}Ga_{0.16}As$ barrier layers. Here the QD PL could be sustained up to 300 K, but the wavelength shifted to around 2.7 μm due to the higher valence band offset of $In_{0.84}Ga_{0.16}As$ barriers. However, it also resulted in improved PL quenching with increasing temperature due to the reduced thermal leakage.

Chapter 7 focused on the InAsSb QD lasers using LPE grown $InAs_{0.61}Sb_{0.13}P_{0.26}$ cladding layers and emitting around 3.1 μm. The maximum working temperature in pulsed mode was increased from 60 K in previous work to 120 K, and the Jth was around 1 kA/cm^2 at 4 K. The gain was determined to be 2.9 cm^{-1} per QD layer, close to type II QW lasers in mid infrared range. The waveguide loss was about 15 cm^{-1} at 4 K. Absorption loss in the waveguide region is high due to the fact that the lasing wavelength almost corresponds to the band gap of InAs. The below threshold spontaneous emission was also measured, and a clear shift from around 3.25 μm to 3.08 μm of the spectra with increasing current was observed. Two possible mechanisms for this blue shift, (band bending and charging effects), were examined and the charging effect turned out to be dominant. Below 50 K the T_0 was about 101 K, but it decreased to about 48 K for T > 50 K. Leakage current from the waveguide into the cladding layers could be the major cause of the increase of J_{th} and decrease of T_0 with rising temperature. The size distribution of QDs is responsible for the high radiative current at low T. For the same reason as in PL, a blue shift of the laser spectrum was also observed with

increasing temperature for T < 50 K. The multi-modal peaks from the lasers were measured using FTIR. There was a slight shift for each group of modes, which was caused by current induced change of material refractive index.

8.2 Suggestions for future work

The final goal of this project is to realize mid infrared antimonide based QD lasers for use in gas sensing and related applications. Based on the progresses to date, a lot of work in different aspects still needs to be done. i) To help reduce the Jth and increase the Tmax of the QD lasers, different non-radiative recombination mechanisms need to be studied experimentally. Spontaneous emission from the lasers for both below and above threshold conditions can be performed, as well as the laser spectral and intensity measurements at different hydrostatic pressures. ii) For the properties of the InAsSb QDs, in order to confirm their size and composition, high resolution TEM or STEM images which can clearly distinguish individual As and Sb atoms need to be obtained. iii) For the growth of the QDs, though the initial results of growing this kind of QDs on GaAs and InP substrates looked quite promising, the thickness of the buffer layers on GaAs substrates still needs to be reduced in order to make laser structures out of that. The threading dislocations may also result in additional leakage current and optical loss, so the density needs to be substantially reduced. Since the growth of QDs on InP substrates with $In_{0.84}Ga_{0.16}As$ barriers proved to be successful, this method can be transplanted to the GaAs platform. Having smaller lattice mismatch with the substrate, it should also help to reduce the threading dislocation densities. However, by using the InGaAs barriers, the QD growth recipe needs to be modified so as to maintain the PL/EL wavelength above 3 μm. iv), For the growth of the laser structure, LPE grown cladding layers may not be the most suitable choice due to the rougher surface and limitations on material compositions. Novel cladding layer structures such as superlattices will be worth experimenting. From the studies on mid infrared QW lasers and our previous work on QD LEDs, it has been suggested

that the incorporation of electron and hole blocking layers into the laser structure can very effectively boost the device performance. In addition, it will also be helpful to grow more layers of QDs with thinner spacer layers in between so that the overall gain can be increased. v) For the diode laser fabrication, narrower laser stripes buried between SiO_2 can be made, which can result in higher injected carrier concentration. The devices can be mounted on heat sinks instead of T0 headers for better heat dissipation. vi), Ideally single mode lasers are needed for the purpose of gas sensing and so prototype DFB or DBR laser structures need to be designed and fabricated corresponding to the required target wavelengths. The growth of QDs and laser structure fabrication both need to be modified so as to meet the required wavelengths. Finally, gas sensing tests should be carried out with the help of collaborators.

Index of Figures and Tables

conduction band. In the CHSH process, the energy from an electron-hole pair recombination is transferred to an electron on the split-off (SO) band and excites it to the heavy hole (HH) band. In the CHLH process, the energy from recombination lifts an electron from the light hole (LH) band to the heavy hole band.

and (c): sample (C). The inset in (a) is a high magnification TEM image of the InSb QD region in sample (A). The insets in (b) and (c) show the details of the AlSb and GaSb interlayers in these two samples respectively.

Fig. 5.3 (a): ω-2θ XRD spectrum of sample (A), the expected periodic side peaks from the QD layers are illustrated by the black curve. (b): ω-2θ XRD spectrum of sample (B), the stronger tail on the left side shoulder of the InAs peak is from the discontinued AlSb interlayer. (c): ω-2θ XRD spectrum of sample (C), the weaker peak on the left side shoulder of the InAs peak is from the GaSb interlayer. (d): ω-2θ XRD spectrum of sample (D), the side peaks are fitted by a MQW model (black curve). (e): The ω-scans of the InAs peak in samples (A), (B) and (C).

Fig. 5.4 PL spectra of samples (A) (red line), (B) (blue line), (C) (green line) and the reference sample (D) (yellow line) measured at 4 K using an excitation intensity of 10 W/cm^2. PL emission from the InAs matrix is also be observed from all samples. The inset shows magnified spectra of the InAs emission originating from different recombination mechanisms in all the samples at 4 K using an excitation intensity of 1 W/cm^2.

Fig. 5.5 Integrated QD PL intensities from samples (A), (B) and (C) at different temperatures. The dotted lines show the exponential fit of PL intensity with temperatures below 60 K, and the dashed lines show the exponential fit for temperatures above 60 K. The inset shows the relation between the logarithm of integrated PL intensity from QDs (ln(I)) and the reciprocal temperature (1/T) from which the activation energy can be extracted. The straight lines give the linear fit in the low 1/T region.

Fig. 5.6 EL spectra from the p-i-n diode structure containing 10 layers of QDs, measured from 10 K to 180 K, with a 20 kHz pulsed current of 1.0 A at 1% duty cycle. The inset illustrates the structure of the p-i-n diode.

Figure 5.7 Temperature dependence of EL intensity from InAs (red squares) and QDs (blue squares). The straight lines show the exponential fit of the InAs EL from 4 K to 180 K and QDs EL from 60 K to 180 K.

Fig. 6.1 Bright field STEM image, magnification 2MX, obtained from Sheffield University. The picture shows an individual sub-monolayer InSb QD in cross-section using an inverted false colour map, where the red colour represents the concentration of Sb.

Fig. 6.2 (a) Calculated transition energy of InSb QD as a function of the QD height for different radius values at 4 K. (b) Calculated transition energy of InAsxSb1-x QD as a function of As composition at 4 K, where the QD size is fixed at 3 nm base radius and 2 nm height.

Fig. 6.3 (a) Simulated GHH state wave function probability distribution in a single InAs0.6Sb0.4 QD assuming a conical shape. (b) Conduction (blue) and valence (red) bands of the InAs$_{0.6}$Sb$_{0.4}$ QD, the dotted red line signifies the calculated position of the GHH state.

Fig. 6.4 (a) Normalized QD PL spectra measured at 4 K (red curve), 40 K(blue curve) and 80 K (green curve). The dotted lines signify the PL peak positions. (b) (Red dots) measured PL peak wavelengths at different temperatures. The data was fitted by the proposed model (blue curve). The inset magnifies the 0-60 K region, showing the

slight blue shift below 40 K, and large red shift above 40 K. The dotted line is only for guidance. (c) Product (bold line) of Fermi-Dirac (dashes) and Gaussian distribution (solid line) functions at different temperatures.

blue line is a linear fit between ln(ΔE) and ln(I).

Bibliography

[1]   T. Suhara, *Semiconductor Laser Fundamentals*. Marcel Dekker, Inc, 2004.

[2]   J. J. Coleman, J. D. Young, and A. Garg, "Semiconductor Quantum Dot Lasers : A Tutorial," *J. Light. Technol.*, vol. 29, no. 4, pp. 499–510, 2011.

[3]   D. Bimberg, M. Grundmann, and N. N. Ledentsov, *Quantum dot heterostructures*. Chichester: John Wiley & Sons, 1999.

[4]   B. R. Nag, *Physics of quantum well devices*. Norwell, MA: Kluwer Academic Publishers, 2000.

[5]   A. Krier, M. Yin, V. Smirnov, P. Batty, P. J. Carrington, V. Solovev, and V. Sherstnev, "The development of room temperature LEDs and lasers for the mid-infrared spectral range," *Phys. Status Solidi*, vol. 205, no. 1, pp. 129–143, Jan. 2008.

[6]   I. Melngailis, "Maser action in InAs diodes," *Appl. Phys. Lett.*, vol. 2, no. 9, p. 176, 1963.

[7]   R. J. Phelan, A. R. Calawa, R. H. Rediker, R. J. Keyes, and B. Lax, "Infrared InSb diode in high magnetic fields," *Appl. Phys. Lett.*, vol. 3, no. 9, p. 143, 1963.

[8]   Z. Yin and X. Tang, "A review of energy bandgap engineering in III–V semiconductor alloys for mid-infrared laser applications," *Solid. State. Electron.*, vol. 51, no. 1, pp. 6–15, Jan. 2007.

[9]   W. Range, T. Hosoda, G. Kipshidze, G. Tsvid, L. Shterengas, and G. Belenky, "Type-I GaSb-based laser diodes operating in 3.1- to 3.3-um wavelength range," *IEEE Photonics Technol. Lett.*, vol. 22, no. 10, pp. 718–720, 2010.

[10]   N. Dasgupta and A. Dasgupta, *Semiconductor devices: modelling and technology*. New Delhi: Prentice-Hall of India, 2004.

[11]   M. Fukuda, *Optical semiconductor devices*. New York: John Wiley & Sons, 1999.

[12]   O. Svelto, *Principles of lasers*. New York: Springer, 1998.

[13]   A. Yariv and P. Yeh, *Photonics: optical electronics in morden communications*, 6th ed. Oxford University Press, 2007.

[14]   H. C. Casey, *Heterostructure lasers*. London: Academic Press, 1978.

[15]   R. Anderson, *Solid state electronics*, 5th ed. 1962.

[16]   H. Kressel and J. Butler, *Semiconductor lasers and heterojunction LEDs*. London: Academic Press, 1977.

[17] I. Vurgaftman and J. R. Meyer, "Band parameters for III − V compound semiconductors and their alloys," *J. Appl. Phys.*, vol. 5815, no. 2001, 2011.

[18] M. P. C. M. Krijn, "Heterojunction band offsets and effective masses in Ill-V quaternary alloys," *Semicond. Sci. Technol.*, vol. 6, pp. 27–31, 1991.

[19] M. Guden and J. Piprek, "wavelength Material parameters of quaternary III − V semiconductors for multilayer mirrors at 1 . 55 μm wavelength," *Model. Simul. Mater. Sci. Eng.*, vol. 4, pp. 349–357, 1996.

[20] S. Adachi, "Band gaps and refractive indices of AlGaAsSb, GaInAsSb and InPAsSb: key properties for a variety of 2-4 um optoelectronic device applications," *J. Appl. Phys.*, vol. 61, no. 10, pp. 4869–4878, 1987.

[21] E. Williams and H. Hall, *Luminescence and the light emitting diodes: the basics and technology of LEDS and the luminescence properties of the materials*. Oxford : Pergamon, 1978.

[22] F. Schubert, *Light emitting diodes*. Oxford University Press, 2003.

[23] P. J. Tang, C. C. Phillips, and R. A. Stradling, "Excitonic photoluminescence in high-purity InAs MBE epilayers on GaAs substrates," *Semicond. Sci. Technol.*, vol. 8, pp. 2135–2142, 1993.

[24] A. Rogalski and Z. Orman, "Band-to-band recombination in InAs1−xSbx," *Infrared Phys.*, vol. 25, no. 3, pp. 551–560, May 1985.

[25] P. Zory, *Quantum well lasers*. London: Academic Press, 1993.

[26] R. Hunsperger, *Integrated optics*, 6th ed. New York: Springer, 2009.

[27] C. Van Opdorp, C. Werkhoven, and A. Vink, "A method to determine bulk lifetime and diffusion coefficient of minority carriers; application to n-type LPE GaP," *Appl. Phys. Lett.*, vol. 30, no. 1, pp. 40–42, 1977.

[28] T. Chakraborty, *Quantum dots: a survey of the properties of artificial atoms*. Amsterdam, 1999.

[29] O. Manasreh, *Introduction to nanomaterials and devices*. Hoboken: John Wiley & Sons, 2012.

[30] P. Michler, *Single quantum dots: fundamentals, applications and new concepts*. Berlin: Springer, 2003.

[31] W. Silvfast, *Laser fundamentals*. Cambridge: Cambridge University Press, 2004.

[32] O. Svelto, *Principles of lasers*. New York: Springer, 1998.

[33]   A. Yariv and P. Yeh, *Photonics: optical electronics in morden communications*, 6th ed. Oxford University Press, 2007.

[34]   A. Yariv and P. Yeh, *Photonics: optical electronics in morden communications*, 6th ed. Oxford University Press, 2007.

[35]   O. Svelto, *Principles of lasers*. New York: Springer, 1998.

[36]   O. Svelto, *Principles of lasers*. New York: Springer, 1998.

[37]   N. V Zotova, S. A. Karandashev, B. A. Matveev, M. A. Remenny, and G. N. Talalakin, "Gain and internal losses in InGaAsSb/InAsSbP double-heterostructure lasers," vol. 33, no. 6, pp. 1–4, 1999.

[38]   C. Caneau, A. Srivastava, A. Dentai, J. Zyskind, and M. Pollack, "Room temperature GaInAsSb/AlInAsSb DH injection lasers at 2.2 um," *Electron. Lett.*, vol. 21, no. 18, pp. 815–816, 1985.

[39]   A. N. Baranov, C. Fouillant, P. Grunberg, J. L. Lazzari, and S. Gaillard, "High temperature operation of GalnAsSb/AIGaAsSb lasers emitting near 2.1 pm double-heterostructure," vol. 65, no. 5, pp. 616–617, 1994.

[40]   A. N. Baranov, E. A. Grebenschikova, B. E. Dzurthanov, T. N. Danilova, A. N. Imenkov, and Y. P. Yakovlev, "Long wavelength lasers based on GaInAsSb solid solutions near the immiscibility boundary ($\lambda \approx 2.5\ \mu m$; T= 300 K)," *Sov. Tech. Phys. Lett.*, vol. 14, pp. 798–800, 1988.

[41]   H. K. Choi, S. J. Eglash, and G. W. Turner, "Double-heterostructure diode lasers emitting at 3 um with a metastable GaInAsSb active layer and AlGaAsSb cladding layers," vol. 64, no. May 1994, pp. 2474–2476, 1994.

[42]   H. K. Choi and S. J. Eglash, "Room-temperature cw operation at 2.2 um of GaInAsSb/AlGaAsSb diode lasers grown by molecular beam epitaxy," *Appl. Phys. B*, vol. 59, no. 10, pp. 1165–1166, 1991.

[43]   A. N. Baranov, A. N. Imenkov, V. Sherstnev, and Y. P. Yakovlev, "2.7-3.9 um InAsSb(P)/lnAsSbP low threshold diode lasers," *Appl. Phys. Lett.*, vol. 64, no. 19, pp. 2480–2482, 1994.

[44]   A. Popov, V. Sherstnev, Y. Yakovlev, and R. Mu, "High power InAsSb / InAsSbP double heterostructure laser for continuous wave operation at 3.6 um," *Appl. Phys. Lett.*, vol. 68, no. 20, pp. 2790–2792, 1996.

[45]   D. Wu, E. Kaas, J. Diaz, B. Lane, A. Rybaltowski, H. J. Yi, M. Razeghi, and S. Member, "InAsSbP – InAsSb – InAs Diode Lasers Emitting at 3.2 um Grown by Metal-Organic Chemical Vapor Deposition," *Appl. Phys. Lett.*, vol. 9, no. 2, pp. 173–175, 1997.

[46]   M. Yin, A. Krier, R. Jones, and P. J. Carrington, "Reduced free carrier absorption loss in midinfrared double heterostructure diode lasers grown by liquid phase epitaxy," *Appl. Phys. Lett.*, vol. 91, no. 10, p. 101104, 2007.

[47]   S. J. Eglasha and H. K. Choi, "InAsSb/AIAsSb double-heterostructure diode lasers emitting at 4 um," *Appl. Phys. Lett.*, vol. 64, no. 7, pp. 833–835, 1993.

[48]   T. Ashley, C. T. Elliott, R. Jefferies, A. D. Johnson, G. J. Pryce, A. M. White, and M. Carroll, "Mid-infrared In1-xAlxSb/InSb heterostructure diode lasers," *Appl. Phys. Lett.*, vol. 70, no. February 1997, pp. 931–933, 1996.

[49]   A. Sugimura, "Band-to-Band Auger Effect in Long Wavelength Multinary Ill-V Alloy Semiconductor Lasers," *IEEE J. Quantum Electron.*, vol. 18, no. 3, pp. 352–363, 1982.

[50]   H. Search, C. Journals, A. Contact, M. Iopscience, and I. P. Address, "Low-threshold long-wave lasers (lambda =3.0-3.6 um) based on III-V alloys," *Semicond. Sci. Technol.*, vol. 8, pp. 1575–1580, 1993.

[51]   R. Liang, J. Chen, G. Kipshidze, D. Westerfeld, L. Shterengas, and G. Belenky, "High-Power 2.2 um Diode Lasers With Heavily Strained Active Region," *IEEE Photonics Technol. Lett.*, vol. 23, no. 10, pp. 603–605, 2011.

[52]   D. Donetsky, G. Kipshidze, L. Shterengas, T. Hosoda, and G. Belenky, "2.3 um type-I quantum well GaInAsSb/AlGaAsSb/GaSb laser diodes with quasi-CW output power of 1.44 W," *Electron. Lett.*, vol. 43, no. 15, pp. 4–5, 2007.

[53]   J. G. Kim, L. Shterengas, R. U. Martinelli, G. L. Belenky, D. Z. Garbuzov, and W. K. Chan, "Room-temperature 2.5 μm InGaAsSb/AlGaAsSb diode lasers emitting 1 W continuous waves," *Appl. Phys. Lett.*, vol. 81, no. 17, p. 3146, 2002.

[54]   J. Chen, D. Donetsky, L. Shterengas, M. V. Kisin, G. Kipshidze, and G. Belenky, "Effect of Quantum Well Compressive Strain Above 1% On Differential Gain and Threshold Current Density in Type-I GaSb-Based Diode Lasers," *IEEE J. Quantum Electron.*, vol. 44, no. 12, pp. 1204–1210, Dec. 2008.

[55]   G. Belenky, L. Shterengas, G. Kipshidze, and T. Hosoda, "Type-I Diode Lasers for Spectral Region Above 3 μm," *IEEE J. Sel. Top. Quantum Electron.*, vol. 17, no. 5, pp. 1426–1434, 2011.

[56]   K. Vizbaras, A. Andrejew, A. Vizbaras, C. Grasse, S. Arafin, and M. Amann, "Low-Threshold 3 μm GaInAsSb / AlGaInAsSb Quantum-Well Lasers Operating in Continuous-Wave up to 64 °C," *23rd Int. Conf. indium phosphide Relat. Mater. , Berlin, Ger.*, pp. 9–12, 2011.

[57]   T. Hosoda, G. Kipshidze, L. Shterengas, and G. Belenky, "Diode lasers emitting near 3.44 um in continuous-wave regime at 300K," *Electron. Lett.*, vol. 46, no. 21, p. 1455, 2010.

[58] K. Vizbaras, A. Vizbaras, A. Andrejew, C. Grasse and M. Amann, "Room-temperature type-I GaSb-based lasers in the 3.0 - 3.7 um wavelength range," *SPIE OPTO. Int. Soc. Opt. Photonics*, p. 82771B–82771B, 2012.

[59] K. Vizbaras and M.C. Amann, "Room-temperature 3.73 μm GaSb-based type-I quantum-well lasers with quinternary barriers," *Semicond. Sci. Technol.*, vol. 27, no. 3, p. 032001, Mar. 2012.

[60] R. M. Briggs, C. Frez, M. Bagheri, C. E. Borgentun, J. A. Gupta, M. F. Witinski, J. G. Anderson, S. Forouhar, M. Sciences, and K. I. A. Or, "Single-mode 2.65 μm InGaAsSb/AlInGaAsSb laterally coupled distributed-feedback diode lasers for atmospheric gas detection," *Opt. Express*, vol. 21, no. 1, pp. 1317–1323, 2013.

[61] S. Belahsene, L. Naehle, M. Fischer, J. Koeth, G. Boissier, P. Grech, G. Narcy, A. Vicet, and Y. Rouillard, "Laser Diodes for Gas Sensing Emitting at 3 . 06 um at Room Temperature," *IEEE Photonics Technol. Lett.*, vol. 22, no. 15, pp. 1084–1086, 2010.

[62] L. Naehle, S. Belahsene, M. von. Edlinger, M. Fischer, G. Boissier, P. Grech, G. Narcy, A. Vicet, Y. Rouillard, J. Koeth, and L. Worschech, "Continuous-wave operation of type-I quantum well DFB laser diodes emitting in 3.4 um wavelength range around room temperature," *Electron. Lett.*, vol. 47, no. 1, p. 46, 2011.

[63] H. K. Choi and G. W. Turner, "High CW power (>200mW/facet) at 3.4 um from InAsSb/lnAlAsSb strained quantum well diode lasers," *Electron. Lett.*, vol. 32, no. 14, pp. 1296–1297, 1996.

[64] A. A. Allerman, R. M. Biefeld, and S. R. Kurtz, "nAsSb-based mid-infrared lasers (3.8–3.9 um) and light-emitting diodes with AlAsSb claddings and semimetal electron injection , grown by metalorganic chemical vapor deposition," *Appl. Phys. Lett.*, vol. 69, no. 4, pp. 465–468, 1996.

[65] G. R. Nash, S. J. B. Przeslak, S. J. Smith, G. de Valicourt, A. D. Andreev, P. J. Carrington, M. Yin, A. Krier, S. D. Coomber, L. Buckle, M. T. Emeny, and T. Ashley, "Midinfrared GaInSb/AlGaInSb quantum well laser diodes operating above 200 K," *Appl. Phys. Lett.*, vol. 94, no. 9, p. 091111, 2009.

[66] Y. Gu, X. Y. Chen, Y. G. Zhang, Y. Y. Cao, X. Fang, and H. S. B. Y. Li, "Type-I mid-infrared InAs/InGaAs quantum well lasers on InP-based metamorphic InAlAs buffers," *J. Phys. D. Appl. Phys.*, vol. 46, no. 50, p. 505103, Dec. 2013.

[67] A. Joullié and P. Christol, "GaSb-based mid-infrared 2–5 μm laser diodes," *Comptes Rendus Phys.*, vol. 4, no. 6, pp. 621–637, Jul. 2003.

[68] S. Sprengel, C. Grasse, P. Wiecha, A. Andrejew, T. Gruendl, G. Boehm, R. Meyer, and M. Amann, "InP-Based Type-II Quantum-Well Lasers and LEDs," *IEEE J. Sel. Top. Quantum Electron.*, vol. 19, no. 4, p. 1900909, 2013.

[69]   J. R. Meyer, C. A. Hoffman, and F. J. Bartoli, "Type-II quantum-well lasers for the mid-wavelength infrared," *Appl. Phys. Lett.*, vol. 67, no. 6, pp. 757–759, 1995.

[70]   S. Sprengel, A. Andrejew, K. Vizbaras, T. Gruendl, K. Geiger, G. Boehm, C. Grasse, and M.C. Amann, "Type-II InP-based lasers emitting at 2.55 μm," *Appl. Phys. Lett.*, vol. 100, no. 4, p. 041109, 2012.

[71]   A. Wilk, M. El Gazouli, M. El Skouri, P. Christol, P. Grech, A. N. Baranov, and a. Joullié, "Type-II InAsSb/InAs strained quantum-well laser diodes emitting at 3.5 μm," *Appl. Phys. Lett.*, vol. 77, no. 15, p. 2298, 2000.

[72]   D. H. Chow, R. H. Miles, T. C. Hasenberg, and A. R. Kost, "Mid-wave infrared diode lasers based on GaInSb/InAs and InAs/AlSb superlattices," *Appl. Phys. Lett.*, vol. 67, no. 25, pp. 3700–3702, 2001.

[73]   T. C. Hasenberg, R. H. Miles, A. R. Kost, and L. West, "Recent advances in Sb-based midwave-infrared lasers," *IEEE J. Quantum Electron.*, vol. 33, no. 8, pp. 1403–1406, 1997.

[74]   Y. Zhang, R. H. Miles, and D. H. Chow, "InAs-InAsxSb1-x Type-II Superlattice Midwave Infrared Lasers Grown on InAs Substrates," *IEEE J. Sel. Top. Quantum Electron.*, vol. 1, no. 2, pp. 749–756, 1995.

[75]   S. R. Kurtz, A. A. Allerman, and R. M. Biefeld, "Midinfrared lasers and light-emitting diodes with InAsSb / InAsP strained-layer superlattice active regions," *Appl. Phys. Lett.*, vol. 70, no. 24, pp. 3188–3190, 2001.

[76]   A. Joullié, "New developments in mid-infrared Sb-based lasers," *J. Phys. IV*, vol. 9, no. 2, pp. 2.79–2.96, 1999.

[77]   W. W. Bewley, H. Lee, I. Vurgaftman, R. J. Menna, C. L. Felix, R. U. Martinelli, D. W. Stokes, D. Z. Garbuzov, J. R. Meyer, M. Maiorov, J. C. Connolly, A. R. Sugg, and G. H. Olsen, "Continuous-wave operation of λ=3.25 μm broadened-waveguide W quantum-well diode lasers up to T=195 K," *Appl. Phys. Lett.*, vol. 76, no. 3, p. 256, 2000.

[78]   C. L. Canedy, W. W. Bewley, J. R. Lindle, I. Vurgaftman, C. S. Kim, M. Kim, and J. R. Meyer, "High-power continuous-wave midinfrared type-II 'W' diode lasers," *Appl. Phys. Lett.*, vol. 86, no. 21, p. 211105, 2005.

[79]   M. Debbichi, A. Ben Fredj, Y. Cuminal, J.-L. Lazzari, S. Ridene, H. Bouchriha, M. Saïd, and P. Christol, "InAsN/GaSb/InAsN 'W' quantum well laser for mid-infrared emission: from electronic structure to threshold current density calculations," *J. Phys. D. Appl. Phys.*, vol. 41, no. 21, p. 215106, Nov. 2008.

[80]   I. Vurgaftman, J. R. Meyer, N. Tansu, and L. J. Mawst, "InP-based dilute-nitride mid-infrared type-II 'W' quantum-well lasers," *J. Appl. Phys.*, vol. 96, no. 8, p. 4653, 2004.

[81]   C.H. Chang, Z.L. Li, C.H. Pan, H.T. Lu, C.P. Lee, and S.D. Lin, "Room-temperature mid-infrared 'M'-type GaAsSb/InGaAs quantum well lasers on InP substrate," *J. Appl. Phys.*, vol. 115, no. 6, p. 063104, Feb. 2014.

[82]   P. G. Eliseev, S. Member, H. Li, G. T. Liu, A. Stintz, T. C. Newell, L. F. Lester, and K. J. Malloy, "Ground-State Emission and Gain in Ultralow-Threshold InAs-InGaAs Quantum-Dot Lasers," *IEEE J. Sel. Top. Quantum Electron.*, vol. 7, no. 2, pp. 135–142, 2001.

[83]   Y. Arakawa, "Multidimensional quantum well laser and temperature dependence of its threshold current," *Appl. Phys. Lett.*, vol. 40, no. 11, p. 939, 1982.

[84]   N. F. Massé, I. P. Marko, A. R. Adams, and S. J. Sweeney, "Temperature insensitive quantum dot lasers: are we really there yet?," *J. Mater. Sci. Mater. Electron.*, vol. 20, no. S1, pp. 272–276, Mar. 2008.

[85]   A. D. Andreev, A. R. Adams, R. Krebs, and A. Forchel, "Importance of Auger recombination in lnAs 1.3 um quantum dot lasers," *Electron. Lett.*, vol. 39, no. 1, pp. 58–59, 2003.

[86]   S. Fathpour, Z. Mi, P. Bhattacharya, A. R. Kovsh, S. S. Mikhrin, I. L. Krestnikov, A. V. Kozhukhov, and N. N. Ledentsov, "The role of Auger recombination in the temperature-dependent output characteristics (T0=∞) of p-doped 1.3 μm quantum dot lasers," *Appl. Phys. Lett.*, vol. 85, no. 22, p. 5164, 2004.

[87]   Y. Qiu, D. Uhl, and S. Keo, "Room-temperature continuous-wave operation of InAsSb quantum-dot lasers near 2 μm based on (001) InP substrate," *Appl. Phys. Lett.*, vol. 84, no. 2, p. 263, 2004.

[88]   T. J. Rotter, A. Stintz, and K. J. Malloy, "InP based quantum dash lasers with 2 μm wavelength," *ieee Proc. Optoelectron.*, vol. 150, no. 4, pp. 4–7, 2003.

[89]   V. A. Solov'ev, O. G. Lyublinskaya, A. N. Semenov, B. Y. Meltser, D. D. Solnyshkov, Y. V. Terent'ev, L. A. Prokopova, A. A. Toropov, S. V. Ivanov, and P. S. Kop'ev, "Room-temperature 3.9–4.3 μm photoluminescence from InSb submonolayers grown by molecular beam epitaxy in an InAs matrix," *Appl. Phys. Lett.*, vol. 86, no. 1, p. 011109, 2005.

[90]   P. J. Carrington, V. A. Solov'ev, Q. Zhuang, A. Krier, and S. V. Ivanov, "Room temperature midinfrared electroluminescence from InSb/InAs quantum dot light emitting diodes," *Appl. Phys. Lett.*, vol. 93, no. 9, p. 091101, 2008.

[91]   A. Krier, X. L. Huang, and A. Hammiche, "Liquid phase epitaxial growth and morphology of InSb quantum dots," *J. Phys. D. Appl. Phys.*, vol. 34, pp. 874–878, 2001.

[92]   K. D. Moiseev, Y. A. Parkhomenko, A. V. Ankudinov, E. V. Gushchina, M. P. Mikha, A. N. Titkov, and Y. P. Yakovlev, "InSb / InAs Quantum Dots Grown by Liquid Phase Epitaxy," *Tech. Phys.*, vol. 33, no. 4, pp. 295–298, 2007.

[93]   P. J. Carrington, V. A. Solov'ev, Q. Zhuang, S. V. Ivanov, and A. Krier, "InSb quantum dot LEDs grown by molecular beam epitaxy for mid-infrared applications," *Microelectronics J.*, vol. 40, no. 3, pp. 469–472, Mar. 2009.

[94]   S. V. Ivanov, A. N. Semenov, V. A. Solov'ev, O. G. Lyublinskaya, Y. V. Terent'ev, B. Y. Meltser, L. G. Prokopova, A. A. Sitnikova, A. A. Usikova, A. A. Toropov, and P. S. Kop'ev, "Molecular beam epitaxy of type II InSb/InAs nanostructures with InSb sub-monolayers," *J. Cryst. Growth*, vol. 278, no. 1–4, pp. 72–77, May 2005.

[95]   Q. Zhuang, P. J. Carrington, and A. Krier, "Growth optimization of self-organized InSb/InAs quantum dots," *J. Phys. D. Appl. Phys.*, vol. 41, no. 23, p. 232003, Dec. 2008.

[96]   A. Semenov, O. G. Lyublinskaya, V. A. Solov'ev, B. Y. Meltser, and S. V. Ivanov, "Surface segregation of Sb atoms during molecular-beam epitaxy of InSb quantum dots in an InAs(Sb) matrix," *J. Cryst. Growth*, vol. 301–302, pp. 58–61, Apr. 2007.

[97]   O. G. Lyublinskaya, V. A. Solov'ev, A. N. Semenov, B. Y. Meltser, Y. V. Terent'ev, L. A. Prokopova, A. A. Toropov, A. A. Sitnikova, O. V. Rykhova, S. V. Ivanov, K. Thonke, and R. Sauer, "Temperature-dependent photoluminescence from type-II InSb∕InAs quantum dots," *J. Appl. Phys.*, vol. 99, no. 9, p. 093517, 2006.

[98]   G. Yeap, S. Rybchenko, I. Itskevich, and S. Haywood, "Type-II InAsxSb1−x/InAs quantum dots for midinfrared applications: Effect of morphology and composition on electronic and optical properties," *Phys. Rev. B*, vol. 79, no. 7, p. 075305, Feb. 2009.

[99]   V. A. Solov, I. V Sedova, O. G. Lyublinskaya, A. N. Semenov, B. Y. Mel, S. V. Sorokin, Y. V. Terent, and S. V. Ivanov, "Midinfrared Injection-Pumped Laser Based on a III − V / II − VI Hybrid Heterostructure with Submonolayer InSb Insets," *Tech. Phys. Lett.*, vol. 31, no. 3, pp. 235–237, 2005.

[100]   J. Faist, F. Capasso, D. L. Sivco, C. Sirtori, A. L. Hutchinson, and A. Y. Cho, "Quantum Cascade Laser," *Science (80-.).*, vol. 264, pp. 553–556, 1994.

[101]   C. Gmachl, F. Capasso, D. L. Sivco, A. Y. Cho, B. Laboratories, L. Technologies, M. Avenue, and M. Hill, "Recent progress in quantum cascade lasers and applications," *reports Prog. Phys.*, vol. 64, pp. 1533–1601, 2001.

[102]   C. Gmachl, F. Capasso, A. Tredicucci, D. L. Sivco, A. L. Hutchinson, S. N. G. Chu, and A. Y. Cho, "Noncascaded intersubband injection lasers at 7.7 um," *Appl. Phys. Lett.*, vol. 73, no. 26, pp. 3830–3832, 1998.

[103] Y. Yao, A. J. Hoffman, and C. F. Gmachl, "Mid-infrared quantum cascade lasers," *Nat. Photonics*, vol. 6, pp. 432–439, 2012.

[104] C. Gmachl, F. Capasso, C. Sirtori, D. L. Sivco, J. N. Baillargeon, and A. Y. Cho, "Distributed feedback quantum cascade lasers," *Appl. Phys. Lett.*, vol. 70, no. 20, pp. 2670–2672, 1997.

[105] M. Beck, D. Hofstetter, T. Aellen, J. Faist, U. Oesterle, M. Ilegems, E. Gini, and H. Melchior, "Continuous wave operation of a mid-infrared semiconductor laser at room temperature.," *Science (80-.).*, vol. 295, no. 5553, pp. 301–305, Jan. 2002.

[106] A. Muller and J. Faist, "The quantum cascade laser: ready for take-off," *Nat. Photonics*, vol. 4, p. 291, Jan. 2010.

[107] F. Xie, C. Caneau, H. P. Leblanc, N. J. Visovsky, S. C. Chaparala, O. D. Deichmann, L. C. Hughes, C. Zah, and D. P. Caffey, "Room Temperature CW Operation of Short Wavelength Quantum Cascade Lasers Made Material on InP Substrates," *IEEE J. Sel. Top. Quantum Electron.*, vol. 17, no. 5, pp. 1445–1452, 2011.

[108] A. Bismuto, M. Beck, and J. Faist, "High power Sb-free quantum cascade laser emitting at 3.3 μm above 350 K," *Appl. Phys. Lett.*, vol. 98, no. 19, p. 191104, 2011.

[109] N. Bandyopadhyay, Y. Bai, B. Gokden, A. Myzaferi, S. Tsao, S. Slivken, and M. Razeghi, "Watt level performance of quantum cascade lasers in room temperature continuous wave operation at λ∼3.76 μm," *Appl. Phys. Lett.*, vol. 97, no. 13, p. 131117, 2010.

[110] J. M. Wolf, A. Bismuto, M. Beck, and J. Faist, "Distributed-feedback quantum cascade laser emitting at 3.2 μm," *Opt. Express*, vol. 22, no. 2, pp. 2111–8, Jan. 2014.

[111] N. Bandyopadhyay, Y. Bai, S. Tsao, S. Nida, S. Slivken, and M. Razeghi, "Room temperature continuous wave operation of λ ∼ 3–3.2 μm quantum cascade lasers," *Appl. Phys. Lett.*, vol. 101, no. 24, p. 241110, 2012.

[112] N. Bandyopadhyay, S. Slivken, Y. Bai, and M. Razeghi, "High power, continuous wave, room temperature operation of λ ∼ 3.4 μm and λ ∼ 3.55 μm InP-based quantum cascade lasers," *Appl. Phys. Lett.*, vol. 100, no. 21, p. 212104, 2012.

[113] J. P. Commin, D. G. Revin, S. Y. Zhang, A. B. Krysa, and J. W. Cockburn, "High performance, high temperature λ≈3.7μm InGaAs/AlAs(Sb) quantum cascade lasers," *Appl. Phys. Lett.*, vol. 95, no. 11, p. 111113, 2009.

[114] Q. Yang, C. Manz, W. Bronner, K. Köhler, and J. Wagner, "Room-temperature short-wavelength (λ∼3.7–3.9 μm) GaInAs∕AlAsSb quantum-cascade lasers," *Appl. Phys. Lett.*, vol. 88, no. 12, p. 121127, 2006.

[115] J. P. Commin, D. G. Revin, S. Y. Zhang, A. B. Krysa, K. Kennedy, and J. W. Cockburn, "High peak power λ~3.3 and 3.5 μm InGaAs/AlAs(Sb) quantum cascade lasers operating up to 400 K," *Appl. Phys. Lett.*, vol. 97, no. 3, p. 031108, 2010.

[116] J. Devenson, O. Cathabard, R. Teissier, and A. N. Baranov, "High temperature operation of λ≈3.3 μm quantum cascade lasers," *Appl. Phys. Lett.*, vol. 91, no. 14, p. 141106, 2007.

[117] J. Devenson, R. Teissier, O. Cathabard, and A. N. Baranov, "InAs∕AlSb quantum cascade lasers emitting below 3 μm," *Appl. Phys. Lett.*, vol. 90, no. 11, p. 111118, 2007.

[118] O. Cathabard, R. Teissier, J. Devenson, J. C. Moreno, and A. N. Baranov, "Quantum cascade lasers emitting near 2.6 μm," *Appl. Phys. Lett.*, vol. 96, no. 14, p. 141110, 2010.

[119] I. P. Marko, A. R. Adams, S. J. Sweeney, R. Teissier, A. N. Baranov, and S. Tomić, "Evidence of carrier leakage into the L-valley in InAs-based quantum cascade lasers under high hydrostatic pressure," *Phys. Status Solidi*, vol. 246, no. 3, pp. 512–515, Mar. 2009.

[120] R. Q. Yang, "Infrared laser based on intersubband transitions in quantum wells," *superlattices Microstruct.*, vol. 17, no. 1, pp. 77–80, 1995.

[121] I. Vurgaftman, W. W. Bewley, C. L. Canedy, C. S. Kim, M. Kim, J. Ryan Lindle, C. D. Merritt, J. Abell, and J. R. Meyer, "Mid-IR Type-II Interband Cascade Lasers," *IEEE J. Sel. Top. Quantum Electron.*, vol. 17, no. 5, pp. 1435–1444, Sep. 2011.

[122] C. L. Canedy, J. R. Lindle, W. W. Bewley, C. S. Kim, M. Kim, J. A. Nolde, I. Vurgaftman, and J. R. Meyer, "Interband Cascade Lasers with Wavelengths Spanning 3.2–4.2 μm," *J. Electron. Mater.*, vol. 38, no. 9, pp. 1948–1951, Mar. 2009.

[123] C. L. Canedy, J. Abell, C. D. Merritt, W. W. Bewley, C. S. Kim, M. Kim, I. Vurgaftman, and J. R. Meyer, "Pulsed and CW performance of 7-stage interband cascade lasers.," *Opt. Express*, vol. 22, no. 7, pp. 7702–10, Apr. 2014.

[124] R. Weih, M. Kamp, and S. Höfling, "Interband cascade lasers with room temperature threshold current densities below 100 A/cm^2," *Appl. Phys. Lett.*, vol. 102, no. 23, p. 231123, 2013.

[125] W. W. Bewley, C. L. Canedy, C. S. Kim, M. Kim, C. D. Merritt, J. Abell, I. Vurgaftman, and J. R. Meyer, "Continuous-wave interband cascade lasers operating above room temperature at λ = 4.7-5.6 μm," *Opt. Express*, vol. 20, no. 3, pp. 3235–40, Jan. 2012.

[126] R. Weih, L. Nähle, S. Höfling, J. Koeth, and M. Kamp, "Single mode interband cascade lasers based on lateral metal gratings," *Appl. Phys. Lett.*, vol. 105, no. 7, p. 071111, Aug. 2014.

[127] C. S. Kim, M. Kim, J. Abell, W. W. Bewley, C. D. Merritt, C. L. Canedy, I. Vurgaftman, and J. R. Meyer, "Mid-infrared distributed-feedback interband cascade lasers with continuous-wave single-mode emission to 80 °C," *Appl. Phys. Lett.*, vol. 101, no. 6, p. 061104, 2012.

[128] A. Y. Cho and J. R. Arthur, *Molecular beam epitaxy. Progress in solid state chemistry*, 10th ed. New York: Pergamon, 1975.

[129] M. Henini, *Molecular beam epitaxy: from research to mass production*. Oxford: Elsevier, 2013.

[130] A. Guinier, *X-ray Diffraction in Crystals, Imperfect Crystals, and Amorphous Bodies*. Toronto: General Publish Company, 1994.

[131] A. Marshall, C. H. Tan, J. David, M. Steer, and M. Hopkinson, "Growth and Fabrication of InAs APDs," in *4th EMRS DTC Technical Conference - Edinburgh*, 2007, p. B14.

[132] J. Shamir, *Optical Systems and Processes*. Bellingham: SPIE, 1999.

[133] V. A. Solov'ev, P. Carrington, Q. Zhuang, K. T. Lai, S. Haywood, S. V. Ivanov, and A. Krier, "InSb/InAs Nanostructures Grown by Molecular Beam Epitaxy Using Sb2 and As2 Fluxes," *Springer Proceeding Phys.*, vol. 119, pp. 129–131, 2008.

[134] D. Leonard, K. Pond, and P. M. Petroff, "Critical layer thickness for self-assembled InAs islands on GaAs," *Phys. Rev. B*, vol. 50, no. 16, p. 11687, 1994.

[135] H. Chen, L. C. Cai, C. L. Bao, J. H. Li, Q. Huang, and J. M. Zhou, "Two-step method to grow InAs epilayer on GaAs substrate using a new prelayer," *J. Cryst. Growth*, vol. 208, no. 1–4, pp. 795–798, Jan. 2000.

[136] L. C. Cai, H. Chen, C. L. Bao, Q. Huang, and J. M. Zhou, "Strain relaxation of InAs epilayer on GaAs under In-rich conditions," *J. Mater. Sci. Lett.*, vol. 22, pp. 599–601, 2003.

[137] S. Kalem, J. I. Chyi, H. Morkoç, R. Bean, and K. Zanio, "Growth and transport properties of InAs epilayers on GaAs," *Appl. Phys. Lett.*, vol. 53, pp. 1647–9, 1988.

[138] T. Przeslawski, A. Wolkenberg, K. Reginski, J. Kaniewski, and J. Bak-Misiuk, "Growth and transport properties of relaxed epilayers of InAs on GaAs," *Thin Solid Films*, vol. 367, pp. 232–234, 2000.

[139] Y. Wang, P. Ruterana, L. Desplanque, S. El Kazzi, and X. Wallart, "Strain relief at the GaSb/GaAs interface versus substrate surface treatment and AlSb interlayers thickness," *J. Appl. Phys.*, vol. 109, no. 2, p. 023509, 2011.

[140] H. S. Kim, Y. K. Noh, M. D. Kim, Y. J. Kwon, J. E. Oh, Y. H. Kim, J. Y. Lee, S. G. Kim, and K. S. Chung, "Dependence of the AlSb buffers on GaSb/GaAs(001) heterostructures," *J. Cryst. Growth*, vol. 301–302, pp. 230–234, Apr. 2007.

[141] S. H. Huang, G. Balakrishnan, A. Khoshakhlagh, A. Jallipalli, L. R. Dawson, and D. L. Huffaker, "Molecular beam epitaxy of type II InSb/InAs nanostructures with InSb sub-monolayers," *Appl. Phys. Lett.*, vol. 88, no. 13, p. 131911, 2006.

[142] A. Jallipalli, G. Balakrishnan, S. H. Huang, A. Khoshakhlagh, L. R. Dawson, and D. L. Huffaker, "Atomistic modeling of strain distribution in self-assembled interfacial misfit dislocation (IMF) arrays in highly mismatched III–V semiconductor materials," *J. Cryst. Growth*, vol. 303, no. 2, pp. 449–455, May 2007.

[143] J. Yang, S. Member, P. Bhattacharya, and Z. Mi, "High-performance In0.5Ga0.5As/GaAs quantum-dot lasers on silicon with multiple-layer quantum-dot dislocation filters," *ieee Trans. Electron. devices*, vol. 54, no. 11, pp. 2849–2855, 2007.

[144] S. Huang, G. Balakrishnan, and D. L. Huffaker, "Interfacial misfit array formation for GaSb growth on GaAs," pp. 1–6, 2009.

[145] R. Hao, S. Deng, L. Shen, P. Yang, J. Tu, H. Liao, Y. Xu, and Z. Niu, "Molecular beam epitaxy of GaSb on GaAs substrates with AlSb/GaSb compound buffer layers," *Thin Solid Films*, vol. 519, no. 1, pp. 228–230, Oct. 2010.

[146] S. Yamaguchi, M. Kariya, S. Nitta, T. Takeuchi, C. Wetzel, H. Amano, and I. Akasaki, "Structural properties of InN on GaN grown by metalorganic vapor-phase epitaxy," *J. Appl. Phys.*, vol. 85, no. 11, p. 7682, 1999.

[147] M. de la Mare, P. J. Carrington, R. Wheatley, Q. Zhuang, R. Beanland, A. M. Sanchez, and A. Krier, "Photoluminescence of InAs 0.926Sb0.063N0.011/InAs multi-quantum wells in the mid-infrared spectral range," *J. Phys. D. Appl. Phys.*, vol. 43, no. 34, p. 345103, Sep. 2010.

[148] Q. Zhuang, P. J. Carrington, and A. Krier, "Growth optimization of self-organized InSb/InAs quantum dots," *J. Phys. D. Appl. Phys.*, vol. 41, no. 23, p. 232003, Dec. 2008.

[149] R. D. Grober and H. D. Drew, "Infrared photoluminescence of InAs epilayers grown on GaAs and Si substrates," *J. Appl. Phys.*, vol. 65, no. 10, pp. 4079–81, 1989.

[150] L. Brusaferri, S. Sanguinetti, E. Grilli, M. Guzzi, A. Bignazzi, F. Bogani, L. Carraresi, M. Colocci, A. Bosacchi, P. Frigeri, and S. Franchi, "Thermally activated carrier

transfer and luminescence line shape in self-organized InAs quantum dots," *Appl. Phys. Lett.*, vol. 69, no. 22, p. 3354, 1996.

[151] S. Sanguinetti, M. Henini, M. Grassi Alessi, M. Capizzi, P. Frigeri, and S. Franchi, "Carrier thermal escape and retrapping in self-assembled quantum dots," *Phys. Rev. B*, vol. 60, no. 11, pp. 8276–8283, Sep. 1999.

[152] O. G. Lyublinskaya, V. A. Solov'ev, A. N. Semenov, B. Y. Meltser, Y. V. Terent'ev, L. A. Prokopova, A. A. Toropov, A. A. Sitnikova, O. V. Rykhova, S. V. Ivanov, K. Thonke, and R. Sauer, "Temperature-dependent photoluminescence from type-II InSb⁄InAs quantum dots," *J. Appl. Phys.*, vol. 99, no. 9, p. 093517, 2006.

[153] S. Kim, B. Fisher, H.-J. Eisler, and M. Bawendi, "Type-II quantum dots: CdTe/CdSe(core/shell) and CdSe/ZnTe(core/shell) heterostructures.," *J. Am. Chem. Soc.*, vol. 125, no. 38, pp. 11466–7, Sep. 2003.

[154] P. J. Carrington, "Quantum Nanostructures grown by Molecular Beam Epitaxy for Mid-Infrared Applications," 2009.

[155] K. J. Cheetham, A. Krier, I. P. Marko, A. Aldukhayel, and S. J. Sweeney, "Direct evidence for suppression of Auger recombination in GaInAsSbP/InAs mid-infrared light-emitting diodes," *Appl. Phys. Lett.*, vol. 99, no. 14, p. 141110, 2011.

[156] I. P. Marko, S. J. Sweeney, A. R. Adams, S. R. Jin, B. N. Murdin, R. Schwertberger, A. Somers, J. P. Reithmaier, and A. Forchel, "Recombination mechanisms in InAs/InP quantum dash lasers studied using high hydrostatic pressure," *Phys. Status Solidi*, vol. 241, no. 14, pp. 3427–3431, Nov. 2004.

[157] G. Q. Lasers, A. R. Adams, S. J. Sweeney, R. Fehse, S. Tomic, E. P. O'reilly, A. Andreev, and H. Riechert, "A Quantitative Study of Radiative, Auger, and Defect Related Recombination Processes in 1.3-um GaInNAs-Based Quantum-Well Lasers," *IEEE J. Sel. Top. Quantum Electron.*, vol. 8, no. 4, pp. 801–810, 2002.

[158] C. Sirtori, P. Kruck, S. Barbieri, H. Page, J. Nagle, M. Beck, J. Faist, and U. Oesterle, "Low-loss Al-free waveguides for unipolar semiconductor lasers," *Appl. Phys. Lett.*, vol. 75, no. 25, p. 3911, 1999.

[159] A. Wilk, M. El Gazouli, M. El Skouri, P. Christol, and P. Grech, "Type-II InAsSb / InAs strained quantum-well laser diodes emitting at 3.5 um," *Appl. Phys. Lett.*, vol. 2298, no. 2000, 2011.

[160] S. C. Heck, S. B. Healy, S. Osborne, R. Fehse, E. P. O'reilly, L. Maltings, F. Lelarge, F. Poingt, A. Accard, F. Pommereau, O. Legouezigou, and B. Dagens, "Theoretical and experimental analysis of InAs/InP quantum dash lasers," in *IPRM 20th International Conference on ndium Phosphide and Related Materials*, 2008.

[161] K. Janssens, B. Partoens, and F. Peeters, "Magnetoexcitons in planar type-II quantum dots in a perpendicular magnetic field," *Phys. Rev. B*, vol. 64, no. 15, p. 155324, Sep. 2001.

[162] N. Kirstaedter, O. G. Schmidt, N. N. Ledentsov, D. Bimberg, V. M. Ustinov, A. Y. Egorov, A. E. Zhukov, M. V. Maximov, P. S. Kop'ev, and Z. I. Alferov, "Gain and differential gain of single layer InAs/GaAs quantum dot injection lasers," *Appl. Phys. Lett.*, vol. 69, no. 9, p. 1226, 1996.

[163] B. Hakki and T. Paoli, "Gain spectra in GaAs double−heterostructure injection lasers," *J. Appl. Phys.*, vol. 46, p. 1299, 1975.

[164] P. M. Smowton and P. Blood, "The differential efficiency of quantum-well lasers," *IEEE J. Sel. Top. Quantum Electron.*, vol. 3, no. 2, pp. 491–498, Apr. 1997.

[165] A. R. Adams, I. P. Marko, N. F. Mass, and S. J. Sweeney, "Effect of non-pinned carrier density above threshold in InAs quantum dot and quantum dash lasers," *IET Optoelectron.*, vol. 8, no. 2, pp. 88–93, Apr. 2014.

[166] N. N. Ledentsov, J. Bohrer, M. Beer, F. Heinrichsdorff, M. Grundmann, and D. Bimberg, "Radiative states in type-II GaSb/GaAs quantum wells," *Phys. Rev. B*, vol. 52, no. 19, pp. 58–66, 1995.

[167] C. Sun, G. Wang, J. E. Bowers, B. Brar, and H. Blank, "Optical investigations of the dynamic behavior of GaSb/GaAs quantum dots," *Appl. Phys. Lett.*, vol. 68, no. March, pp. 1543–1545, 1996.

[168] K. Gradkowski, N. Pavarelli, T. J. Ochalski, D. P. Williams, J. Tatebayashi, G. Huyet, E. P. O'Reilly, and D. L. Huffaker, "Complex emission dynamics of type-II GaSb/GaAs quantum dots," *Appl. Phys. Lett.*, vol. 95, no. 6, p. 061102, 2009.

[169] J. Tatebayashi, A. Khoshakhlagh, S. H. Huang, G. Balakrishnan, L. R. Dawson, D. L. Huffaker, D. A. Bussian, H. Htoon, and V. Klimov, "Lasing characteristics of GaSb⁄GaAs self-assembled quantum dots embedded in an InGaAs quantum well," *Appl. Phys. Lett.*, vol. 90, no. 26, p. 261115, 2007.

[170] H. Mani, "Realization et Edude d'une Double Heterostructure Laser InAsSb/InAsSbP Emettant a Plus de 3 Microns," 1989.

[171] S. A. Choulis, A. Andreev, M. Merrick, A. R. Adams, B. N. Murdin, A. Krier, and V. V. Sherstnev, "High-pressure measurements of mid-infrared electroluminescence from InAs light-emitting diodes at 3.3 μm," *Appl. Phys. Lett.*, vol. 82, no. 8, p. 1149, 2003.

[172] J. R. Meyer, C. L. Felix, W. W. Bewley, I. Vurgaftman, E. H. Aifer, L. J. Olafsen, J. R. Lindle, C. A. Hoffman, M. Yang, B. R. Bennett, B. V Shanabrook, H. Lee, C. H. Lin, S. S. Pei, and R. H. Miles, "Auger coefficients in type-II InAs/Ga1-xInxSb quantum wells," *Appl. Phys. Lett.*, vol. 73, no. 20, pp. 2857–2859, 1998.

[173] P. E. O'reilly and M. Silver, "Temperature sensitivity and high temperature operation of long wavelength semiconductor lasers," *Appl. Phys. Lett.*, vol. 63, no. 24, pp. 3318–3320, 1993.

[174] P. W. Epperlein, *Semiconductor Laser Engineering, Reliability and Diagnostics: A Practical Approach to High Power and Single Mode Devices*. Chichester: John Wiley & Sons, 2013.

[175] B. R. Bennett, R. A. Soref, S. Member, and J. A. D. E. L. Alamo, "Carrier-Induced Change in Refractive Index of InP , GaAs , and InGaAsP," *IEEE J. Quantum Electron.*, vol. 26, no. I, pp. 113–22, 1990.

[176] P. P. Paskov, "Refractive indices of InSb, InAs, GaSb, InAsxSb1-x, and In1-xGaxSb: Effects of free carriers," *J. Appl. Phys.*, vol. 81, no. 4, pp. 1890–8, 1996.